# OPTIMIZATION OF SPACE DEBRIS COLLISION AVOIDANCE MANEUVER


**Priyatharsan Epoor Rajasekar**

Master of Engineering

Department of Mechanical Engineering

McGill University

Montreal, Quebec


December 2017

A thesis submitted to McGill University in partial fulfillment of the requirements of the degree of Master of Engineering

# ACKNOWLEDGEMENTS

First and foremost, I would like to express my gratitude to my supervisor, Dr. Arun K Misra for his cordial support, and guidance which helped me in carrying out this research. His extensive knowledge and experience have taught me tremendously over the past two years. I also appreciate the opportunity he gave me to work on the Space Situational Awareness project in collaboration with the industries KinetX Aérospatiale International (KAI), KinetX Aerospace and Visual Analytics Research and Development Consortium of Canada.

I take this opportunity to thank Frederic Pelletier, the President of KAI, and Narendra Gollu, the Senior Engineer of KAI, it was a pleasure to work with them during the collaborative project on Space Situational Awareness.

I wish to thank the team from KinetX Aerospace, for their constant support, especially on the technical issues that I faced during the early stage of my research.

I would thank my colleagues in my lab, Eleonora Botta and Isabelle Jean—for sharing their passion, working in this research field.

Finally, I wish to thank my friends and family, for standing by and providing the moral support during my time at McGill.

# ABSTRACT

The rising population of space debris poses a collision hazard to active satellites functioning in their orbits around the Earth. Often these satellites are required to perform orbital maneuvers to avoid high-energy collision with space debris. In addition to maintaining a safe proximity from the approaching debris during the time of closest approach, it is crucial to ensure that the satellite must then be brought back to its nominal orbit. This requires execution of additional orbital maneuvers and optimizing these maneuvers is important so that the impact on the mission life is minimal. Therefore, a framework of minimum-fuel orbital maneuvers in the context of finding an optimal trajectory considering both collision avoidance and orbit re-entry is desired. Most of the previous research work was focused only on optimization of orbital maneuver for collision avoidance. In this study, trajectory optimization for both maneuver processes is attempted using an evolutionary algorithm for which two methods: three-impulse method and two-impulse method, are developed and investigated.

The three-impulse method is established as a two-stage maneuver process. In the first maneuver stage, a small impulse is applied to alter the course of the satellite in order to avoid the predicted collision. The second stage involves a bi-impulse maneuver that will take the satellite back to its nominal orbit after bypassing the obstacle. This bi-impulsive maneuver is estimated using the solutions of the well-known Lambert's problem. The design of the two-impulse method, on the other hand, is more straightforward which involves determining the optimal transfer orbit by just solving the Lambert's problem while the constraints are satisfied to an acceptable level.

The proposed methods are tested for a high-risk collision predicted in a Low Earth Orbit while the test involves accurate numerical propagation taking into account the Earth zonal harmonics and the attraction from other bodies (Sun and Moon). The numerical simulations demonstrate that the conjunction could be mitigated satisfying the minimum-fuel objective and the satellite-safety constraints.

# ABRÉGÉ

La population croissante de débris spatiaux présente un risque de collision pour les satellites actifs fonctionnant sur leurs orbites autour de la Terre. Souvent, ces satellites doivent effectuer des manœuvres orbitales pour éviter les collisions à haute énergie avec les débris spatiaux. En plus de maintenir une proximité sécuritaire avec les débris au moment où ils sont le plus proches, il est crucial de s'assurer que le satellite doit être ramené à son orbite nominale. Cela nécessite l'exécution de manœuvres orbitales supplémentaires. L'optimisation de ces manœuvres est importante pour que l'impact sur la durée de vie de la mission soit minime. Par conséquent, un cadre de manœuvres orbitales à carburant minimum dans le contexte de la recherche d'une trajectoire optimale tenant compte à la fois de l'évitement des collisions et de la rentrée d'orbite est souhaité. La plupart des travaux de recherche précédents étaient axés uniquement sur l'optimisation de la manœuvre orbitale pour éviter les collisions. Dans cette étude, l'optimisation de trajectoire pour les deux processus de manœuvre est tentée en utilisant un algorithme évolutif pour lequel deux méthodes, la méthode à trois impulsions et la méthode à deux impulsions, sont développées et étudiées.

La méthode à trois impulsions est établie comme un processus de manœuvre en deux étapes. Dans la première phase de la manœuvre, une petite impulsion est appliquée pour modifier la trajectoire du satellite afin d'éviter la collision prévue. La deuxième étape consiste en une manœuvre à deux impulsions qui ramènera le satellite à son orbite nominale après avoir contourné l'obstacle. Cette manœuvre bi-impulsive est estimée à l'aide des solutions du problème bien connu de Lambert. D'un autre côté, la conception de la méthode à deux impulsions est plus directe, ce qui implique de déterminer l'orbite de transfert optimale en résolvant simplement le problème de Lambert alors que les contraintes sont satisfaites à un niveau acceptable.

Les méthodes proposées sont testées pour une collision à haut risque prédite dans une orbite terrestre basse, ce qui demande que le test implique une propagation numérique précise prenant en compte les harmoniques zonales de la Terre et de l'attraction de corps supplémentaires (Soleil et Lune). Les simulations numériques démontrent que la conjonction pourrait être atténuée en satisfaisant l'objectif du minimum de carburant et les contraintes de sécurité du satellite.

# LIST OF SYMBOLS

| | |
|---|---|
| $\Delta\boldsymbol{v}$ | Change in velocities that quantifies fuel consumption |
| $\boldsymbol{P_c}$ | Collision Probability |
| $\boldsymbol{X}$ | Axis directing along vernal equinox in the Earth-Centered Inertial reference frame |
| $\boldsymbol{Y}$ | Axis completing the right-hand rule in the Earth-Centered Inertial reference frame |
| $\boldsymbol{Z}$ | Axis directing along the celestial North pole in the Earth-Centered Inertial reference frame |
| $\boldsymbol{R}$ | Axis directing along radius vector of the satellite from the Earth's center |
| $\boldsymbol{T}$ | Axis pointing in the direction of motion of the satellite in its orbit |
| $\boldsymbol{N}$ | Axis pointing in the direction of the angular momentum of the satellite |
| $\boldsymbol{r_s}$ | Position vector of the satellite in the Earth-Centered Inertial reference frame |
| $\boldsymbol{v_s}$ | Velocity vector of the satellite in the Earth-Centered Inertial reference frame |
| $\boldsymbol{x_s}$ | $\boldsymbol{X}$-axis component of the satellite position vector expressed in the Earth Centered Inertial reference frame |
| $\boldsymbol{y_s}$ | $\boldsymbol{Y}$-axis component of the satellite position vector expressed in the Earth Centered Inertial reference frame |
| $\boldsymbol{z_s}$ | $\boldsymbol{Z}$-axis component of the satellite position vector expressed in the Earth Centered Inertial reference frame |
| $\boldsymbol{\dot{x}_s}$ | $\boldsymbol{X}$-axis component of the satellite velocity vector expressed in the Earth Centered Inertial reference frame |
| $\boldsymbol{\dot{y}_s}$ | $\boldsymbol{Y}$-axis component of the satellite velocity vector expressed in the Earth Centered Inertial reference frame |
| $\boldsymbol{\dot{z}_s}$ | $\boldsymbol{Z}$-axis component of the satellite velocity vector expressed in the Earth Centered Inertial reference frame |

| | |
|---|---|
| $\boldsymbol{M_{ECI \rightarrow RTN}}$ | Transformation matrix or Direction cosine matrix that facilitates conversion of state vector from Earth Centered Inertial reference frame to Radial-Transverse-Normal reference frame of the satellite |
| $\boldsymbol{M_{RTN \rightarrow ECI}}$ | Transformation matrix or Direction cosine matrix that facilitates conversion of state vector from Earth Centered Inertial reference frame to Radial-Transverse-Normal reference frame of the satellite |
| $\boldsymbol{\xi}$ | Axis orthogonal to two other axes of Encounter coordinate system |
| $\boldsymbol{\eta}$ | Axis directing along relative velocity vector of the debris with respect to the satellite |
| $\boldsymbol{\zeta}$ | Axis pointing in the direction parallel to the common perpendicular to the two velocity vectors: satellite velocity vector and debris velocity vector |
| $\boldsymbol{r_d}$ | Position vector of the debris in the Earth-Centered Inertial reference frame |
| $\boldsymbol{v_d}$ | Velocity vector of the debris in the Earth-Centered Inertial reference frame |
| $\boldsymbol{v_r}$ | Relative velocity vector of the debris with respect to satellite in the Earth-Centered Inertial reference frame |
| $\boldsymbol{a}$ | Semi-major axis of the reference orbit |
| $\boldsymbol{e}$ | Eccentricity of the reference orbit |
| $\boldsymbol{i}$ | Inclination of the reference orbit |
| $\boldsymbol{\theta}$ | True anomaly of the reference orbit |
| $\boldsymbol{E}$ | Eccentric anomaly of the reference orbit |
| $\boldsymbol{\Omega}$ | Right ascension of the ascending node of the reference orbit |
| $\boldsymbol{\omega}$ | Perigee argument of the reference orbit |
| $\boldsymbol{C}$ | Covariance matrix, defined in chapter 2 section 2.4.1 |
| $\boldsymbol{\sigma}$ | Standard deviation in the reference axis, defined in chapter 2 section 2.4.1 |
| $\boldsymbol{\rho}$ | Correlation between the standard deviation, defined in chapter 2 section 2.4.1 |

| | |
|---|---|
| $\boldsymbol{J}$ | Objective function corresponding to the optimization problem |
| $\boldsymbol{t_0}$ | Epoch at which initial avoidance maneuver is applied (Three-impulse method) |
| $\boldsymbol{t_1}$ | - Epoch at which the second maneuver is applied (Three-impulse method)<br>- Epoch at which avoidance maneuver is applied (Two-impulse method) |
| $\boldsymbol{t_2}$ | - Epoch at which re-entry (third) maneuver is applied (Three-impulse method)<br>- Epoch at which re-entry maneuver is applied (Two-impulse method) |
| $\boldsymbol{t_c}$ | Time of predicted collision |
| $\boldsymbol{t_{ca}}$ | Time of closest approach |
| $\boldsymbol{r_{rel}}$ | Relative distance between the satellite and the debris |
| $\boldsymbol{\rho_c}$ | Combined object radius of the satellite and the debris |
| $\boldsymbol{\rho_s}$ | Object radius of the satellite |
| $\boldsymbol{\rho_d}$ | Object radius of the debris |
| $\boldsymbol{V}$ | Volume swept by the sphere of radius $\boldsymbol{\rho_c}$ |
| $\boldsymbol{u}$ | Parameter corresponding to collision probability by Chan's method, defined in Chapter 2 section 2.6.2 |
| $\boldsymbol{v}$ | Parameter corresponding to collision probability by Chan's method, defined in Chapter 2 section 2.6.2 |
| $\boldsymbol{T}$ | Orbital period of the reference object |
| $\boldsymbol{\tau}$ | Dimensionless time referred as in orbits |
| $\boldsymbol{F}$ | Mutation factor corresponding to Self Adaptive Differential Evolution |
| $\boldsymbol{C_r}$ | Crossover ratio corresponding to Self Adaptive Differential Evolution |
| $\boldsymbol{N}$ | Size of randomly generated population |
| $\boldsymbol{g}$ | Generation number |
| $\boldsymbol{n_i}$ | Size of the sub-population |

| | |
|---|---|
| $\Delta \boldsymbol{v_{tot}}$ | Total change in velocities involved in the optimization problem |
| $\Delta \boldsymbol{v_0}$ | Initial avoidance maneuver vector |
| $\Delta \boldsymbol{v_1}$ | - Vector representing the second maneuver in Three-impulse method<br>- Avoidance maneuver vector in Two-impulse method |
| $\Delta \boldsymbol{v_2}$ | - Vector representing third (re-entry) maneuver in Three-impulse method<br>- Re-entry maneuver vector in Two-impulse method |
| $\Delta \boldsymbol{\tau_{am}}$ | Orbital location at which initial avoidance maneuver is applied |
| $\Delta \boldsymbol{t_f}$ | Time of flight between two points |
| $\Delta \boldsymbol{\tau_f}$ | Non-dimensionless parameter for time of flight |
| $\boldsymbol{c}$ | Chord joining two points in a reference orbit |
| $\Delta \boldsymbol{\theta}$ | Change in true anomaly |
| $\Delta \boldsymbol{\tau_\theta}$ | Non-dimensionaless parameter for change in true anomaly |
| $\boldsymbol{f}$ | Parameter used in Lambert's problem, refer Chapter 3 section 3.3.1 |
| $\boldsymbol{g}$ | Parameter used in Lambert's problem, refer Chapter 3 section 3.3.1 |
| $\dot{\boldsymbol{f}}$ | Parameter used in Lambert's problem, refer Chapter 3 section 3.3.1 |
| $\dot{\boldsymbol{g}}$ | Parameter used in Lambert's problem, refer Chapter 3 section 3.3.1 |
| $\boldsymbol{p}$ | Parameter used in Lambert's problem, refer Chapter 3 section 3.3.1 |
| $\boldsymbol{r_r}$ | Position vector of the satellite in the nominal orbit at the point of re-entry |
| $\boldsymbol{v_r}$ | Velocity vector of the satellite in the nominal orbit at the point of re-entry |
| $\boldsymbol{\theta_c}$ | True anomaly corresponding to the position of the satellite in the nominal orbit at the time of predicted collision |
| $\boldsymbol{U}$ | Earth's gravitational potential |
| $\boldsymbol{r_t}$ | Position vector of the satellite in the reference orbit at any instant $t$ |
| $\boldsymbol{v_t}$ | Velocity vector of the satellite in the reference orbit at any instant $t$ |

| | |
|---|---|
| $\boldsymbol{\varphi}$ | In-plane rotation angle |
| $\psi$ | Out-of-plane rotation angle |
| $\Delta \boldsymbol{r}_{ca}$ | Miss distance between the satellite and the debris at the time of closest approach |
| $\boldsymbol{D}_{m}$ | Minimum desired miss distance |
| $\boldsymbol{P}_{max}$ | Maximum allowable collision probability |
| $\boldsymbol{TF}_{1}$ | First transfer orbit |
| $\boldsymbol{TF}_{2}$ | Second transfer orbit |
| $\Delta \boldsymbol{v}_{R}$ | Change in velocity in the radial direction of the satellite |
| $\Delta \boldsymbol{v}_{T}$ | Change in velocity in the transverse direction of the satellite |
| $\Delta \boldsymbol{v}_{N}$ | Change in velocity in the direction normal to the satellite's orbit |

# LIST OF ABBREVIATIONS

| | |
|---|---|
| CAM | Collision Avoidance Maneuver |
| SADE | Self Adaptive Differential Evolution |
| TCA | Time of closest approach |
| LEO | Low Earth Orbit |
| MEO | Medium Earth Orbit |
| GEO | Geostationary Orbit |
| HEO | High Eccentric Orbit |
| ISS | International Space Station |
| US-SSN | United States Space Surveillance Network |
| RSO | Residual Space Object |
| ADR | Active Debris Removal |
| PMD | Post-Mission Disposal |
| PDF | Probability density function |
| GSOC | German Space Operations Center |
| JSpOC | Joint Space Operations Center |
| TPBVP | Two Point Boundary Value Problem |
| GA | Genetic Algorithm |
| MOPSO | Multi-Objective Partial Swarm Optimizer |
| ECI | Earth Centered Inertial (reference frame) |
| RTN | Radial-Transverse-Normal (reference frame) |
| RAAN | Right Ascension of the Ascending Node |
| TLE | Two Line Elements |
| CCSDS | Consultative Committee for Space Data Systems |
| CA | Conjunction Analysis |
| CSSI | Center of Space Standards and Innovation |
| CARA | Conjunction Assessment Risk Analysis |
| ODE | Ordinary Differential Equation |
| OREKIT | Orbit Exploration tool KIT |

| | |
|---|---|
| SGP4 | Simplified General Perturbations propagator |
| NORAD | North American Aerospace Defence Command |
| DE | Differential Evolution |
| CDM | Conjunction Data message |
| UTC | Universal Time Constant |

# LIST OF FIGURES

# LIST OF TABLES

# TABLE OF CONTENTS

## 3. THREE-IMPULSE MANEUVER OPTIMIZATION



## 4. TWO-IMPULSE MANEUVER OPTIMIZATION

## 5. CONCLUSION

# INTRODUCTION

## 1.1 OVERVIEW

Since the beginning of spaceflight with the launch of the first man-made satellite, Sputnik 1, the era of space exploration has continued to grow and the number of launches per year has significantly increased. Today, more than 1400 operational satellites are orbiting around the Earth [1], majority of them are in Low-Earth Orbits (LEO), at an altitude of between 160 to 2,000 km. Some of the most prominent of these include the International Space Station (ISS), the Hubble Space Telescope and many Earth observation satellites. About a one-third of them are in geostationary orbits (GEO), at an altitude of 35,800 km, the rest are in Medium Earth Orbits (MEO) and high-eccentric elliptical orbits (HEO). Satellites are used in various disciplines and activities including Space exploration, Earth observation, navigation, telecommunication and even in agriculture and meteorology.

The increase in interest for space activities and possible space-based commercial exploitation has given rise to a new threat: space debris. Almost all space missions generate space debris. This led to the establishment of surveillance systems that monitor, track and maintain a catalog of all detectable earth orbiting objects. According to the United States Space Surveillance Network, there are over 18,640 objects larger than 10 cm are orbiting the Earth. Figure 1.1 shows the evolution of number of objects orbiting the Earth that are cataloged by US-SSN [2] in which a very small fraction of the total objects corresponds to the operational satellites, while the rest are rocket bodies, discarded payloads, and satellites that are dormant.

Apart from launch and mission-related objects, the secondary sources for the increase in space debris population are: in-orbit fragmentation, explosions of satellites and rocket bodies, and accidental collisions [3]. These events are highly catastrophic, even a tiny bit of the order of object size <1mm (e.g., a paint flake) can cause severe damage to active satellites and induce further fragmentation. The consequence of such events leads to a cascading effect of debris fragments that would cause formation of debris belts around the Earth. This phenomenon is known as *Kessler Syndrome*. Among the orbital regimes LEO, MEO, and GEO, LEO has the most space debris. This is because the majority of the satellites are launched into LEO [4] in order to save fuel cost.

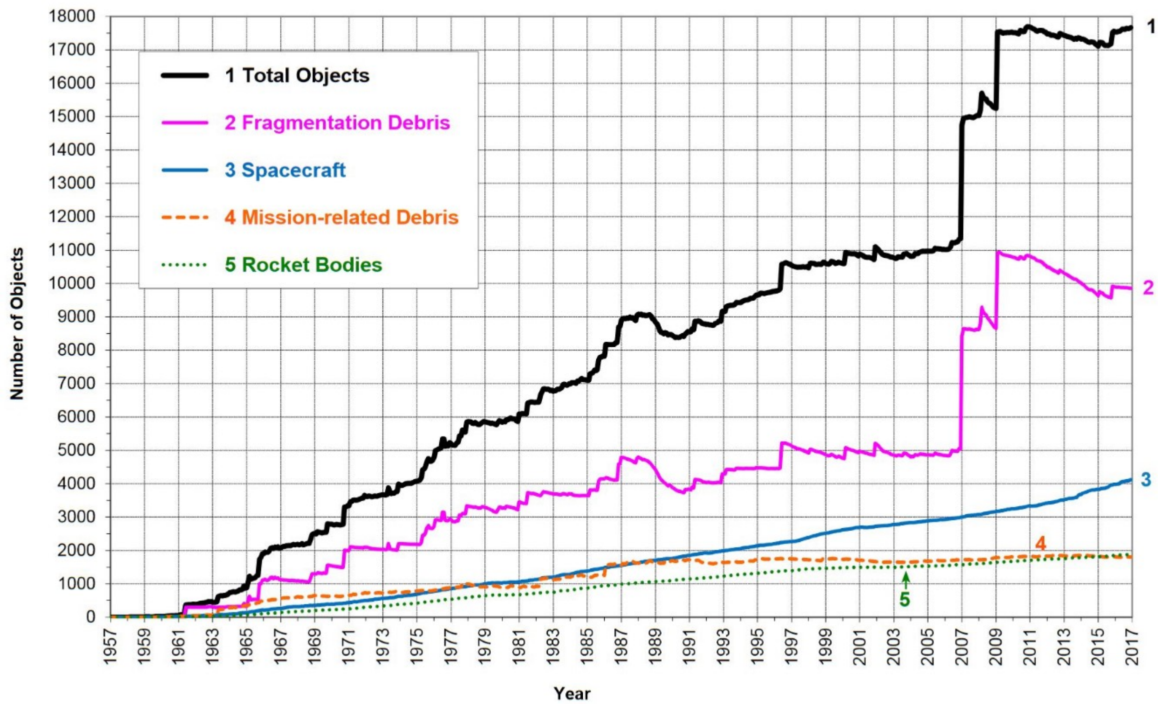


**Fig. 1. 1 Number of Objects in Earth Orbit by Object Type cataloged by the U.S. Space Surveillance Network.**

Two events that occurred in the recent past largely contributed to the rise in population of Residual Space Objects (RSO) in the LEO region. In 2007, China intentionally destroyed its retired weather satellite, Fengyun-1C, at an altitude of 865 km, to test an anti-satellite missile. In 2009, the first accidental collision took place between an operational US satellite - Iridium 33 and a defunct Russian satellite - Cosmos 2251, at an altitude of 789 Km. The US-SSN has cataloged over 3,400 pieces of debris associated with Fengyun-1C, over 600 debris associated with Iridium-33 and over 1,600 debris associated with Cosmos 2251, as of January 2016 [5] The majority of the conjunctions with International Space Station's threat volume was found to involve debris resulting directly from these two disastrous events. Consequently, the ISS was moved often to avoid impact with such debris in its orbit. Figure 1.2 depicts the number of debris avoidance maneuvers performed since the launch of ISS in 1998 [6].

These incidents clearly indicate that it is important to curb the debilitating growth in the debris population by preventing collisions involving the residual space objects. This can be achieved by implementing various mitigation strategies that are being studied such as Active Debris Removal (ADR), Post-Mission Disposal (PMD), Collision Avoidance Maneuver (CAM). From an industrial perspective, the cost-to-benefit trade-off for ADR makes them unlikely to be utilized while PMD and CAM have become more common [7]. This study, however, is related to preventing collision by performing collision avoidance maneuvers (CAM).

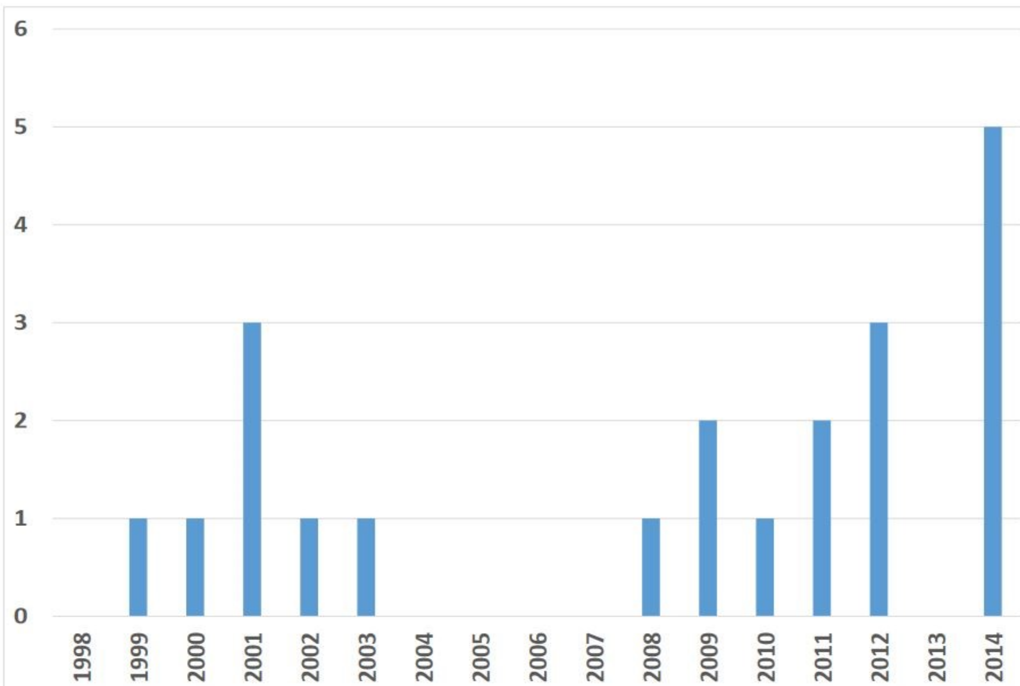


**Fig. 1. 2 Occurrences of Debris Avoidance Maneuvers since the launch of first ISS module, Zarya, in 1998**

The principle of collision avoidance maneuver is to reduce the risk of a predicted collision by increasing the separation distance between the operational satellite and the approaching debris and decreasing the probability that they collide during closest approach. Thus, a typical collision avoidance problem entails, maximizing the separation distance and minimizing the collision probability within the encounter geometry. In addition, it is important to keep the amount of fuel required for the maneuver as low as possible while steadily deviating from the anticipated conjunction, thereby not affecting the satellite's operational life. The fuel requirement absolutely tends to increase when more separation is desired; therefore, a balance between the total fuel cost and the amount of deviation desired during the closest approach must be established. This is possible by optimizing the total-$\Delta v$ budget required for collision avoidance, thereby, treating it as a constrained optimization problem.

Another factor to be considered when planning for an avoidance maneuver is to recover the maneuverable satellite back to its original orbit; i.e., orbital re-entry. Although several studies have been conducted on planning collision avoidance maneuvers [8] and determining fuel-optimal solutions for such planned maneuvers [9-12], none has yet considered finding optimal solutions for combined collision avoidance and orbital re-entry. Thus, this work is aims at determining a single-best solution for an optimal collision avoidance maneuver that includes orbit re-insertion.

## 1.2 LITERATURE REVIEW

In this section, a brief review of the literature relevant to this thesis is presented. The following subsections will discuss some of the work done in the field of a) collision-risk assessment that involves estimation of collision probability, b) trajectory design using Lambert's problem, and c) computation of avoidance maneuver for mitigating the risk of collision.

### 1.2.1 COLLISION PROBABILITY

Collision probability determines the level of risk of collision between any two objects in space. Calculation of the collision probability, $P_c$, plays a critical part in the conjunction risk assessment and planning of collision avoidance maneuvers, as it acts as the primary decision maker whether to perform an avoidance maneuver or not. If the probability is higher than a desired threshold then it is an indication that the two objects will collide. Ultimately, this allows the space agencies and satellite operators to affirm on performing collision avoidance maneuvers so that they could prevent the collision of their asset against the approaching object. However, it matters how accurate the probability prediction is in view of the influencing factors such as position and velocity uncertainty and the conjunction geometry.

In general, the equation for collision probability comprises of information about relative dynamics (position and velocity vectors of the two objects) and the associated error covariance while the probability density function (pdf) is considered to follow Gaussian distribution [13]. The collision probability is then computed by integrating this density function over the volume swept by the combined object radius of the satellite and the approaching object. Previous studies have shown that the collision probability can be determined distinctively such that they differ by two major factors; accuracy and computation speed [14]. This subsection addresses some of the dominant methods that have successfully been used by various space industries.

The three-dimensional integral appearing in the collision probability calculations can be reduced to two dimensions by eliminating the dimension parallel to the relative velocity vector. Foster [15] modified the resulting two-dimensional density function by changing the coordinate system to polar coordinates in the conjunction plane. This model is then numerically evaluated by dividing the combined object's circular cross-section into concentric circle and radial straight lines.

Patera [16] developed a one-dimensional line integral, mathematically equivalent to the two-dimensional probability equation. Instead of integrating over the area of the combined object, Patera's formulation involved integrating around the perimeter of that area (hard-body circle). This is achieved by performing a coordinate rotation and a subsequent scale change to make the density distribution symmetric. This symmetric form of the probability density enabled the two-dimensional integral to be reduced to a one-dimensional integral which was further converted into a path/line integral.

The method developed by Alfano [17] evaluates the collision probability numerically by using error function (erf) and exponential terms, thereby formulating a series expression. Alfano [18] later introduced a strategy to determine maximum collision probability by assessing the possible variables such as the orientation of the position vector with respect to the covariance axes in the encounter ellipse, minor axis standard deviation and the aspect ratio. Although not required, it is desired to have covariance data in order to obtain better results to determine the maximum value for the collision probability by considering the worst-case scenario. Hence, the user has an upper bound to make a decision for risk assessment. Jackson [19] enhanced this approach by imparting an iterative process thereby improving the accuracy of the original method.

Unlike other methods in which collision probability was evaluated numerically, Chan's [20] formulations converted the two-dimensional Gaussian integral to one-dimensional Rician integral and introduced the concept of equivalent areas. As a result, Chan developed analytical series expressions containing two exponential terms.

Alfano [14] compared both numerical (Foster, Patera, and Alfano) and analytical (Chan) models over a wide range of collision parameters (miss distance, standard deviations and collision cross-section radius). The results revealed that all the four models were in good agreement. On the other hand, in terms of computational efficiency, Chan's method was found to be the fastest and Foster's being the slowest. Alfano and Patera models are almost equivalent.

### 1.2.2 LAMBERT'S PROBLEM

Lambert's problem is the most well-known boundary value problem in the field of astrodynamics that involves the determination of a Keplerian orbit connecting two position vectors within the specified time interval [21]. Lambert's problem plays a key role in this research work for determining optimal trajectory that allows safe-return of the satellite to its original orbit after circumventing the predicted collision. This orbital boundary value problem is a problem of determining an orbit connecting two points constrained within a specified time of flight. Several formulations have been developed for solving Lambert's problem [22] and there exist numerous applications where the solutions of Lambert's problem are used. Some of the applications are concerned with orbit design for mission planning, space rendezvous and interception, and ballistic missile targeting.

The initial solutions of Lambert's problem were geometrically formulated by Lagrange [23]. Lagrange's approach expressed transfer time between the two position vectors as a function of semi-major axis and derived an elegant equation. Gauss, on the other hand, in his *Theoria*

*Motus* [24], developed a method to solve this problem using sector-to-triangle area ratio for both elliptic and hyperbolic orbits.

Subsequent to the fundamental solution given by Lagrange and Gauss, several authors have discussed alternative formulations to the problem by adopting various approaches [25]. They all differ in the details of at least one of the following fundamental factors: a) the geometric transfer parameter, b) the initial guess for the free parameter, c) the iteration method, and d) the computation of terminal velocity vectors. The performance of these algorithms has been extensively tested and compared quantitatively based on the above factors by Sangrà and Fantino [25]. The study affirmed that the two solvers, developed by Bate et al. [26] and Izzo [27], incorporated the best qualities, Bate's algorithm being the fastest while Izzo's *Householder* algorithm showed best performance results.

### 1.2.3 COLLISION AVOIDANCE MANEUVER

Previous studies have made important contributions to the development of an optimal collision avoidance maneuver planning that will be presented in this thesis. The main idea of collision avoidance maneuver is to reduce the risk of a predicted collision by increasing the miss distance (i.e., distance of separation) between the primary and the secondary object within the encounter geometry. To perform this maneuver as efficiently as possible, the following three parameters are to be examined:

i. time at which the maneuver is applied,
ii. magnitude of the delta-v, and
iii. direction (in-plane and out-of-plane components) of the applied delta-v.

Any orbital maneuver requires a certain amount of expensive onboard fuel; therefore, it is highly desirable to find out an optimal strategy for collision avoidance maneuver. There have been several studies on this topic of collision avoidance maneuver; however, only the most relevant ones are discussed here.

A gradient technique was developed by Patera [8] to find the maneuver direction for a set of possible maneuver times before the predicted conjunction. For this approach, the collision probability was considered to weigh against the maneuver direction. The displacement of the maneuvering vehicle was conjectured to be linearly proportional to the maneuver velocity magnitude. By taking advantage of this assumption, this method implemented a one-dimensional root finding schemes such as the secant method or Newton-Raphson method to determine the maneuver magnitude. This maneuver design was then applied to an actual high collision risk case involving two geostationary satellites. The post--maneuver state vectors determined from this study indicated that the maneuver worked as planned at reducing the collision probability to an acceptable level.

To guarantee the satellite's operational life, the amount of fuel required for the maneuver must be kept as low as possible while steadily deviating from the anticipated conjunction. A considerable amount of research was conducted by Bombardelli [7] in finding an optimal solution for the collision avoidance maneuver, aimed at reducing the maneuver cost while maximizing the separation distance and minimizing the collision probability. In his work, the formulation of collision avoidance maneuver was deemed as an eigenvalue problem under the assumption that the applied burn is impulsive. Closed-form analytical expressions for the relative dynamics between two approaching objects on a B-plane frame were introduced. This resulted in deriving an optimum maneuver direction as a function of arc length separation between the maneuver point and the predicted collision point [7]. Though this approach may have provided highly accurate analytical solutions, unfortunately, it may not be applicable in practice as the algorithm considers only the Keplerian dynamics.

Aida et al. [11] developed an avoidance maneuver strategy that involved increasing the radial separation by applying an in-track thrust half a period prior to the closest approach. It was found that this approach has already been applied to the operational-Low Earth Orbit satellites monitored by the German Space Operations Center (GSOC). Since only a tangential shift was taken into consideration, this approach was considered to be effective in the long run as the satellite can easily be brought back to its nominal orbit shortly after the closest approach. However, the fuel expenditure could possibly be higher compared to a more general approach of collision avoidance maneuver when taking into account both in-plane (radial and transverse) and out-of-plane (normal) thrusting.

Lee et al. [28] proposed a suboptimal continuous control algorithm that incorporated a penalty term into the performance index and designed such that the penalty rises sharply as two objects approaches. Then the generating functions are introduced as the main tool for solving a Two-Point Boundary Value Problem (TPBVP) for a Hamiltonian system. Though this algorithm was able to generate optimal collision-free trajectories without any initial guess or iterative process, it requires additional efforts to develop higher-order generating functions and to empirically update the penalty function parameters.

In recent studies, it was noted that the design of collision avoidance maneuver can also be tackled as a direct optimization problem using traditional evolutionary algorithms. Lee and Kim [12] proposed a method for collision avoidance maneuver design for both LEO and GEO objects using Genetic Algorithm (GA). The optimization problem was aimed at minimizing a single scalar objective function by taking into account several mission constraints and combining them using weighting factors. It is evident that an optimal solution cannot be obtained in a single run as this technique requires an accurate selection of weights.

On the other hand, Morselli et al. [10] addressed the problem using a Multi-Objective-Particle-Swarm-Optimizer (MOPSO) to obtain a set of optimal solutions. The authors defined four objective functions that simultaneously minimize the *fuel consumption* and increase the *separation distance* while reducing the *collision risk* and handling the *mission constraints*. These two studies are related to the research presented herein which the optimization problem is still treated as a single-objective in minimizing the fuel consumption whereas the miss distance and collision probability are treated as inequality constraints. This eliminates the complexity of the optimization problem and provides a single best solution.

Some studies have also focused on developing an effective mitigation strategy for multiple threatening objects within a brief period of time using evolutionary algorithms. Kim et al. [29] presented an approach by using Genetic Algorithm (GA) to obtain a solution for such complex conjunction situations. Though outside the scope of this research, this application may be examined in the future works.

## 1.3 OBJECTIVES

The objective of this thesis is to determine a single-best minimal-fuel solution by planning a collision avoidance maneuver that considers both collision avoidance as well as orbital re-entry. Two approaches are proposed in this thesis, three-impulse method and two-impulse method, both satisfying three goals: keep the asset (satellite) at a safe distance away from the approaching object (debris) during the time of the closest approach, bring the asset back to its nominal orbit to continue its operation and minimize the total $\Delta v$ consumption for the orbital maneuvers involved. The $\Delta v$s involved are considered to be impulsive.

The design of the three-impulse CAM approach consists of two-stages. The first stage is concerned with avoiding the predicted collision by applying an optimal avoidance maneuver. This initial avoidance maneuver is optimized based on the time of application of the maneuver its direction, and magnitude. This allows the satellite to deviate from its original orbit and consequently, it increases the separation distance with respect to the approaching debris thereby reducing the probability of collision at the predicted time of closest approach. The second stage is attributed to the orbital re-entry of the satellite, wherein a bi-impulse maneuver leading to the re-entry of the satellite to its nominal orbit is determined. The optimization of this bi-impulsive maneuver is based on solving for a minimum-$\Delta v$ solution for the so-called Lambert's problem. And the corresponding optimal trajectory path is characterized by two parameters: a) the time interval between the two impulses (time of flight) and b) the orbital location at which the satellite must re-enter.

In the second approach, only two impulses are considered, the first maneuver is to avoid the collision and the second corresponds to the orbital re-entry. The optimization of this method purely relies on solving for an optimal transfer trajectory using the Lambert’s problem. Consequently, the optimization parameters are the maneuver execution time that determines the orbital locations at which the satellite de-orbits (point before predicted collision time) and re-enters (point after predicted collision time) back to its original orbit and the transfer period between the two points.

Ultimately, the cost function for both the methods is nothing but the sum of all the associated $\Delta v$s involved, i.e., the total-$\Delta v$. Thus, after defining the cost function, the optimization parameters for both the avoidance maneuver and orbital re-entry, the constraints are established that monitor the safe bypass of the satellite during the time of closest approach.

In this study, the cost function and the associated optimization parameters are assessed using Self-Adaptive Differential Evolution (SADE). The performance of the two proposed methods is investigated in terms of the total-$\Delta v$ achieved under the principal constraints on the minimum separation distance between the satellite and the debris, the maximum collision probability during closest approach and the boundary conditions for the maneuver execution time. The proposed algorithms are tested for high-risk conjunctions predicted in Low Earth Orbits through numerical simulations while the test involves numerical propagation under the Earth zonal harmonics ($J_2$-perturbation effect) and the third body attraction.

## 1.4 THESIS OUTLINE

The thesis is divided into five chapters. In the first chapter, the current trend with regards to space situational awareness is introduced. Then the motivation behind this research work and the objectives are discussed. It also includes a brief review of the literature surveyed during the study. The second chapter summarizes the conceptual background required for conducting this work. It demonstrates about the various processes and factors to be accounted before planning for collision avoidance maneuver. The third and fourth chapters detail the three-impulse and two-impulse method, respectively, proposed in this work. The numerical simulations for each method are presented in their respective chapter. Finally, the conclusions from the current work and suggestions for future work are presented in the fifth chapter.

# PRELIMINARY INFORMATION

## 2.1 OVERVIEW

This chapter addresses the fundamentals that are required to be understood before planning for collision avoidance maneuver (CAM). The chapter is divided into seven sections that provide essential knowledge for the development of CAM operation. The first section summarizes the content of this chapter. The second section provides the general view of all the coordinate systems and reference frames that are utilized in this work, while the third briefly summarizes the orbital elements that define how an orbiting object's state can be described with respect to the Earth. The fourth section discusses the uncertainties in position and velocity of an object and describes how this uncertainty can be mathematically represented in the forthcoming calculations.

In the fifth and sixth sections, the types of data available and how such data are implemented to perform collision risk analysis are described. Finally, the tools that are implemented in this study in order to successfully develop and simulate the proposed methods are discussed in the seventh and eighth sections.

## 2.2 COORDINATE SYSTEMS

When determining the orbital motion for objects in space it is convenient to work with one of several available reference frames. These reference frames move through the space, centered at the Earth or the object/satellite itself. The geocentric frames are used to completely describe the trajectory of an object in orbit around the Earth. On the other hand, the satellite-centered reference frames apply to studies of relative motion and to analyze velocity changes or drag effects on the objects in orbit [30].

### 2.2.1 EARTH-CENTERED INERTIAL COORDINATE SYSTEM

Earth-Centered Inertial (ECI) reference frame, shown in Figure 2.1, is one of the universally accepted quasi-inertial or Newtonian coordinate systems in the field of astrodynamics. The frame has its origin at the center of mass of the Earth with the **X**-axis aligned with the vernal equinox in the celestial equator, the **Z**-axis along the celestial North Pole also known as Earth's spin axis and the **Y**-axis completing the right-hand rule. The frame J2000 or EME2000 [30], the commonly used quasi-inertial ECI frame, serves as the basis for most of the orbital propagations in this thesis.

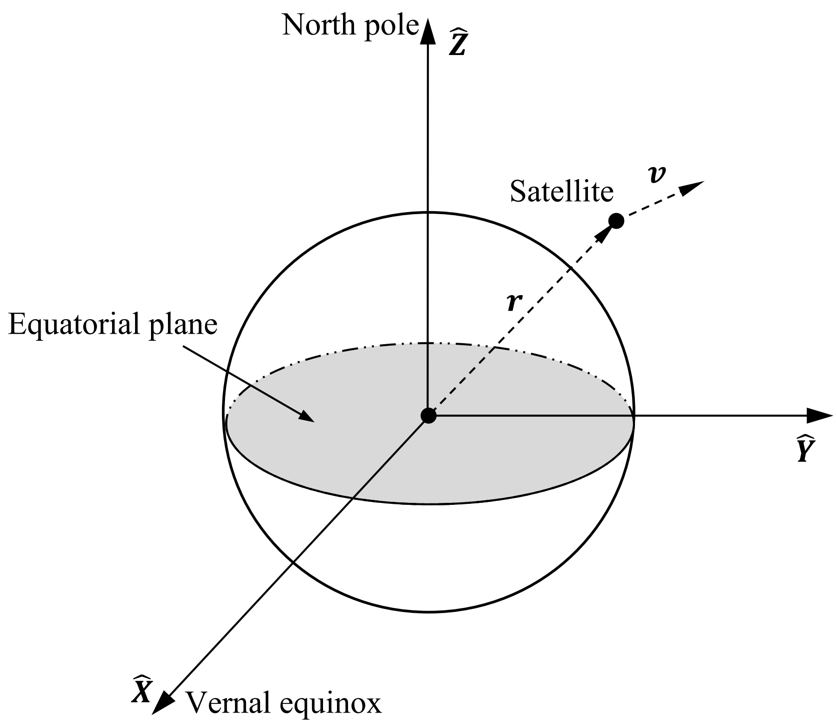


**Fig. 2. 1 Earth Centered Inertial (ECI) coordinate system**

### 2.2.2 RADIAL-TRANSVERSE-NORMAL COORDINATE SYSTEM

The Radial-Transverse-Normal (RTN) reference frame [30], shown in fig 2.2, is a satellite-centered local orbiting frame that moves with the satellite over time. In this coordinate system, the **R**-axis points in the direction along the radius vector from the Earth's center towards the satellite. The **N**-axis points in the direction of the angular momentum, normal to the satellite's orbital plane and the **T**-axis consequently completes the right-hand set of the coordinate axes, perpendicular to the radial direction. It is noteworthy that the **T**-axis is not necessarily parallel to the velocity vector except in the case where the satellite is in a circular orbit. Typically, RTN frame is used to determine the radial, along-track and cross-track separation of the debris with respect to the satellite's origin.

$$\widehat{\boldsymbol{R}} = \frac{\boldsymbol{r_s}}{|\boldsymbol{r_s}|} \tag{2.1}$$

$$\widehat{\boldsymbol{T}} = \widehat{\boldsymbol{N}} \times \widehat{\boldsymbol{R}} \tag{2.2}$$

$$\widehat{\boldsymbol{N}} = \frac{\boldsymbol{r_s} \times \boldsymbol{v_s}}{|\boldsymbol{r_s} \times \boldsymbol{v_s}|} \tag{2.3}$$

where, $\boldsymbol{r_s} = x_s\widehat{\boldsymbol{X}} + y_s\widehat{\boldsymbol{Y}} + z_s\widehat{\boldsymbol{Z}}$ is the position and $\boldsymbol{v_s} = \dot{x}_s\widehat{\boldsymbol{X}} + \dot{y}_s\widehat{\boldsymbol{Y}} + \dot{z}_s\widehat{\boldsymbol{Z}}$ is the velocity of the satellite in the ECI frame. In matrix notation,

$$\begin{bmatrix} \widehat{\boldsymbol{R}} \\ \widehat{\boldsymbol{T}} \\ \widehat{\boldsymbol{N}} \end{bmatrix} = \begin{bmatrix} R_x & R_y & R_z \\ T_x & T_y & T_z \\ N_x & N_y & N_z \end{bmatrix} \begin{bmatrix} \widehat{\boldsymbol{X}} \\ \widehat{\boldsymbol{Y}} \\ \widehat{\boldsymbol{Z}} \end{bmatrix} \tag{2.4}$$

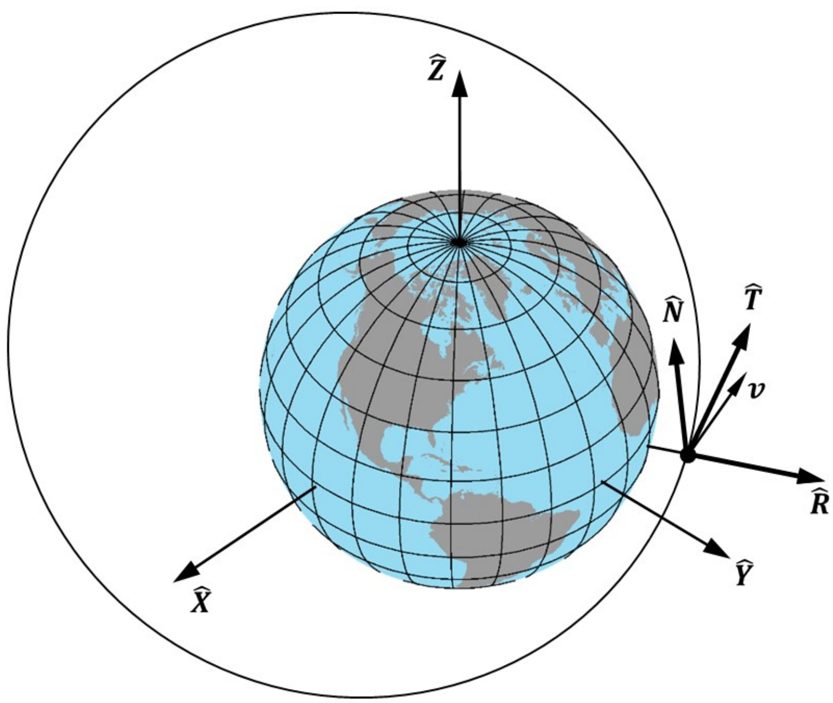


**Fig. 2. 2 Radial Transverse Normal (RTN) coordinate system**

Define

$$M_{ECI\rightarrow RTN} = \begin{bmatrix} R_x & R_y & R_z \\ T_x & T_y & T_z \\ N_x & N_y & N_z \end{bmatrix} \tag{2.5}$$

where, $M_{ECI\rightarrow RTN}$ is the transformation matrix in which its elements are the direction cosines between the ECI and RTN reference frames and are given by the equations (2.1), (2.2), and (2.3). This transformation matrix $M_{ECI\rightarrow RTN}$ is orthogonal such that its inverse is equal to its transpose.

$$[M_{ECI\rightarrow RTN}]^{-1} = [M_{ECI\rightarrow RTN}]^{T} = M_{RTN\rightarrow ECI} \tag{2.6}$$

### 2.2.3 ENCOUNTER COORDINATE SYSTEM

For calculations involving conjunction of two objects, the satellite and the debris, a third reference frame based on the debris relative dynamics with respect to the satellite is used that defines the encounter geometry. The origin of the encounter frame is attached to the center of the satellite and has the $\boldsymbol{\eta}$-axis directed along the debris relative velocity vector. The $\boldsymbol{\zeta}$-axis lies parallel to the common perpendicular line to the two velocities and the $\boldsymbol{\xi}$-axis is orthogonal to the other two axes. The $\xi$- $\zeta$ plane perpendicular to the $\boldsymbol{\eta}$-axis is known as the encounter plane or conjunction plane [18], shown in Figure 2.3. Clearly, the equation for the unit vectors representing the direction of the coordinate axes can be expressed as [13]:

$$\hat{\boldsymbol{\xi}} = \hat{\boldsymbol{\eta}} \times \hat{\boldsymbol{\zeta}} \tag{2.7}$$

$$\hat{\boldsymbol{\eta}} = \frac{\boldsymbol{v}_r}{|\boldsymbol{v}_r|} = \frac{\boldsymbol{v}_d - \boldsymbol{v}_s}{|\boldsymbol{v}_d - \boldsymbol{v}_s|} \tag{2.8}$$

$$\hat{\boldsymbol{\zeta}} = \frac{\boldsymbol{v}_d \times \boldsymbol{v}_s}{|\boldsymbol{v}_d \times \boldsymbol{v}_s|} \tag{2.9}$$

where, $\boldsymbol{v}_s$ and $\boldsymbol{v}_d$ are the velocities of the satellite and debris in the ECI frame, respectively.

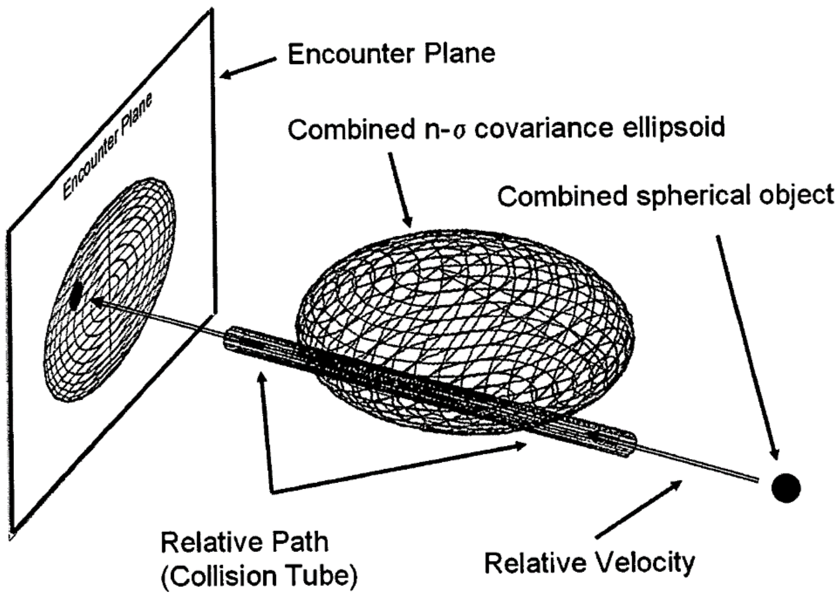


**Fig. 2. 3 Encounter plane [31]**

## 2.3 ORBITAL ELEMENTS

Orbital elements are the parameters that define the state of an object in space for a given time. There are several ways of describing it, the simplest form is the state vector representation associated with the components of the position and velocity vector of the object in an inertial reference frame. The state vector consists of 6 quantities that completely describe the orbit of an object. However, it is hard to visualize them and compare with other object's state in a meaningful way. To overcome this problem, classical or Keplerian orbital elements are introduced. Keplerian orbital elements are the common way of expressing the state of an object in orbit. It consists of six independent quantities that are grouped into two subgroups, dimensional elements and orientation elements [32].

The dimensional elements consist of semimajor axis $a$, eccentricity $e$ and true anomaly $\nu$ that describes the size and shape of the orbit and the location of the object in the orbit with respect to the perigee. If the orbit is circular, then the semimajor axis simply represents the radius of the circular orbit while the eccentricity becomes zero. True anomaly $\theta$ is the angle between the direction of the periapsis and the current position of the object; at times, the true anomaly is replaced with eccentric anomaly $E$. Figure 2.4 [33] illustrates how the position of a satellite in its orbit can be referenced with respect to true anomaly $\nu$ and eccentric anomaly $E$.

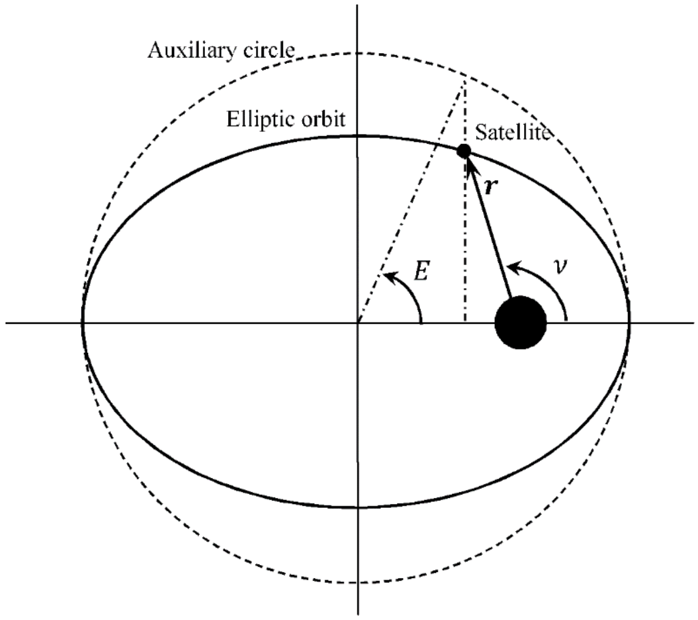


**Fig. 2. 4 Illustration of true and eccentric anomaly**

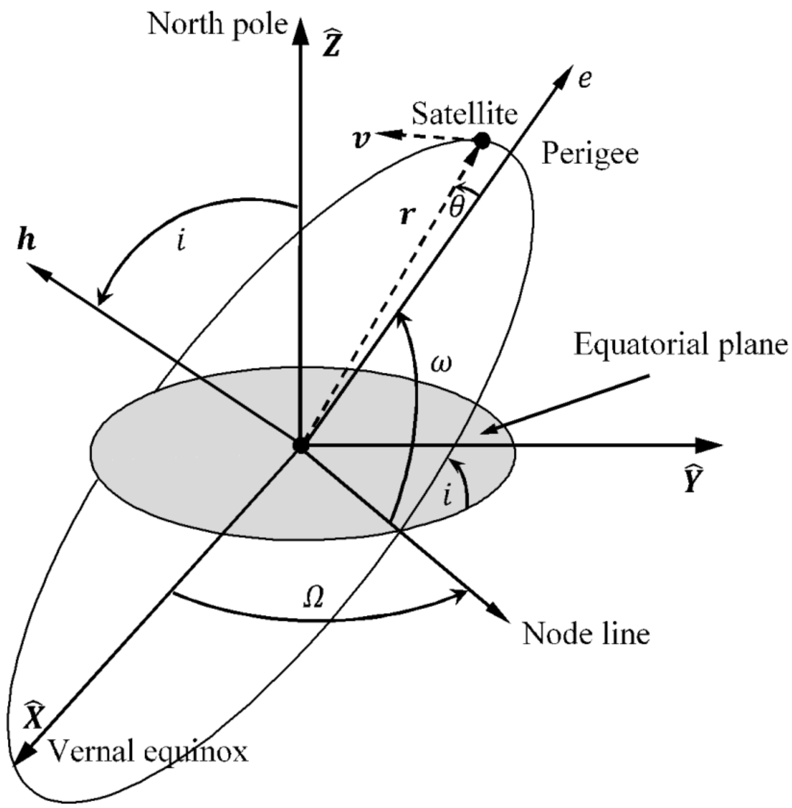


**Fig. 2. 5 Orbital elements in ECI frame**

The orientation elements stand for angular representation of the orbit in space. It consists of inclination $i$, right ascension of the ascending node $\Omega$ and perigee argument $\omega$. The inclination $i$, specifies the angle of tilt of the orbit plane with respect to the Earth's equatorial reference plane. The right ascension of the ascending node $\Omega$ or simply RAAN is the angle in the equatorial plane measured positively from the vernal equinox, **X**-axis of the ECI frame, to the ascending node where the object makes its south-to-north crossing. The perigee argument $\omega$ is the angle measured from the ascending node to the periapsis point on the orbit (perigee). Figure 2.5 [30] shows the 6 orbital elements in an ECI frame.

## 2.4 UNCERTAINTY IN POSITION AND VELOCITY

Due to the difficulty in tracking the objects accurately in space, their position and velocity are inevitably determined with a certain level of uncertainty. Even when the position of an object is precisely known at an arbitrary time [34], the perturbing forces make the uncertainty in position to grow significantly over time upon propagating the orbit, because the perturbations such as the Earth's oblateness and atmospheric drag cause a considerable amount of deviations from the nominal Keplerian orbit. Nevertheless, with the current orbit propagation models, it is impossible to reproduce these perturbation effects acting on an orbiting object.

In addition, while performing collision risk analysis between two objects it is important to know the nominal relative position between them and the error in their trajectories based on which the satellite operator can calculate the risk between them and thus plan for an avoidance maneuver accordingly. This shows the significance of understanding the uncertainties in terms of error.

The uncertainty in velocity, however, can be neglected under the assumption of linear relative motion for conjunctions that occur within a brief period. In addition, the relative velocity is considered sufficiently large during the closest approach [13] since the encounter time is brief and thereby it entails static covariance. Thus, it is adequate to take into account only the positional uncertainty while calculating collision probability for risk assessment.

The error in position is assumed to be normally distributed in all directions such that positional uncertainty can be defined in the form of an error ellipsoid around the space object [34]. If the error ellipsoids of two objects overlap, then we have a probability of collision. Mathematically, these error ellipsoids can be represented as covariance matrices that follow Gaussian distribution.

### 2.4.1 COVARIANCE MATRIX

A covariance matrix provides information about where an object can be positioned, within the error ellipsoid region, in reference to its nominal position [35]. It contains entries of the variance in distance taking into account the correlation between three different principal axes standard deviations; this is why the name covariance. If $\sigma_x$, $\sigma_y$ and $\sigma_z$ are the standard deviations in the principal directions, then the covariance matrix can be written as:

$$C_{3x3} = \begin{bmatrix} {\sigma_x}^2 & \rho_{xy}\sigma_x\sigma_y & \rho_{xz}\sigma_x\sigma_z \\ \rho_{xy}\sigma_x\sigma_y & {\sigma_y}^2 & \rho_{yz}\sigma_y\sigma_z \\ \rho_{xz}\sigma_x\sigma_z & \rho_{yz}\sigma_y\sigma_z & {\sigma_z}^2 \end{bmatrix} \tag{2.10}$$

where $\rho_{xy}$, $\rho_{xz}$ and $\rho_{yz}$ define the correlation between the standard deviations.

For collision risk assessment, a combined covariance matrix is formed by adding the individual covariances of the satellite and debris, and this greatly simplifies the calculation of collision probability during conjunction. The resulting combined covariance matrix results in a new error ellipsoid describing the relative uncertainties between the two in a common reference frame. However, this combining becomes possible only if the individual covariance matrices are uncorrelated and if they are described in the same reference frame [35]. For better results, it is desired to propagate the relative uncertainties up until the time of closest approach [36]. However, propagating the covariances is beyond the scope of this thesis work, instead, the covariance data obtained from the Conjunction Data Message is used explicitly.

## 2.5 DATA SOURCES

Ideally, for any method involved, the accuracy in planning for an optimal collision avoidance maneuver (CAM) requires high-quality data with which the conjunction scenario can be simulated not only to predict the collision but also to certainly decide whether to plan and perform the CAM itself.

### 2.5.1 TWO LINE ELEMENTS

Two Line Element (TLE) dataset is a comprehensive data set that encloses the orbital elements of an object at the epoch time at which it was tracked. TLE for each object is regularly updated by United States Air Force that routinely tracks all objects of size larger than 10cm orbiting around the Earth. The recorded observations are then cataloged into two-line sets. Figure 2.6 shows a typical TLE set containing elementary orbital information with regards to the object [37].

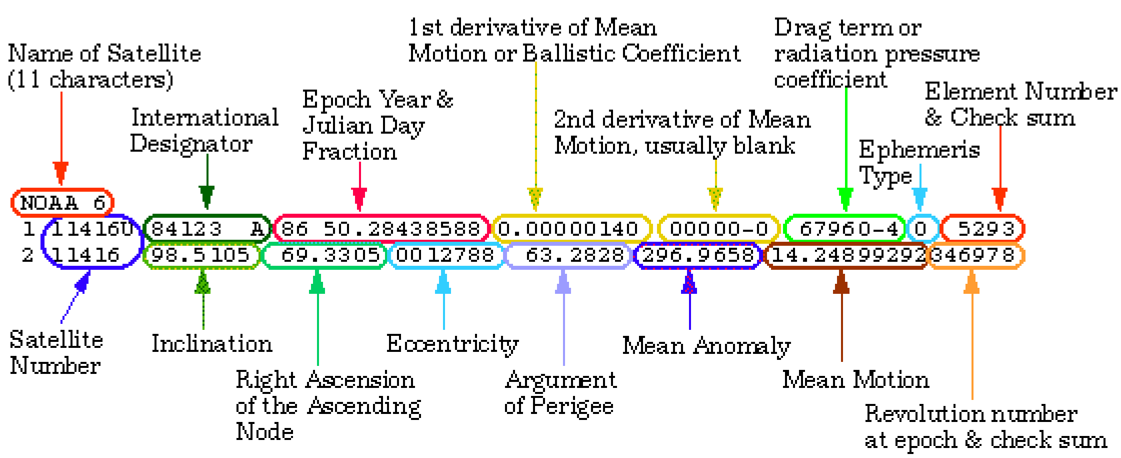


**Fig. 2. 6 Two-Line Element set example [37]**

### 2.5.2 CONJUNCTION DATA MESSAGE

Conjunction Data Message is a standardized message format, maintained by the Consultative Committee for Space Data Systems (CCSDS), that provides information about possible collisions between a satellite and a debris (collectively called as conjunction pair) recorded by JSpOC. It contains data with regards to the predicted collision such as state vectors of both satellite and debris, relative dynamics, covariance matrix, time and distance of closest approach, collision probability value and the type of method, descriptive information such as force models used to propagate both satellite and debris during the creation of CDM.

In this work, for the objects under study, the both TLEs and CDMs are used for testing and analysis of the proposed methods. It is noteworthy, that the TLEs provides only orbital data for a given object at a specific epoch which is then propagated forward, using SGP4 propagation theory, to determine the closest approach with any other object in the catalog. TLEs are ideally used for the pre-screening process during conjunction analysis to filter out the conjunction pairs from the full-catalog. On the other hand, CDMs are specifically designed for conjunction perspective that provides accurate information related to the collision geometry. TLEs are extracted from the publicly available Space-Track [38] website which is the major distributor of TLE for all unclassified objects while CDMs are obtained from the CCSDS website [39].

## 2.6 CONJUNCTION ANALYSIS AND PLANNING OF COLLISION AVOIDANCE MANEUVER

Conjunction Analysis (CA) [40] can be collectively described as the process of predicting upcoming encounters (or close approaches) between any two objects in the catalog and determining the level of risk posed between them (the conjunction pairs). CA is the foremost step, accounted before planning for any collision avoidance maneuver, which helps to determine the likelihood of collision between any two objects obtained from the full-catalog (i.e., by performing all-on-all analysis) [41] and the frequency of the near misses that occur every single day. The full-catalog consists of comprehensive data sets – Two-Line Element sets that provide all necessary information about the objects that are cataloged.

Many space agencies have developed conjunction analysis tools that can routinely perform collision risk assessment, orbit covariance analysis, collision probability calculation and provide collision avoidance maneuver simulations. The Center of Space Standards and Innovation (CSSI) developed an online service that offers Satellite Orbital Conjunction

Reports Assessing Threatening Encounters in Space (SOCRATES) [42], capable of performing conjunction analysis between a list of all orbiting satellite payloads with regards to a list of all orbiting objects, using the catalog containing all unclassified TLE sets, on a weekly basis. Likewise, NASA developed CARA – Conjunction Assessment Risk Analysis tool [43] capable to perform Conjunction Analysis routinely and notifies the satellite owner/operators when conjunctions are found involving their satellites.

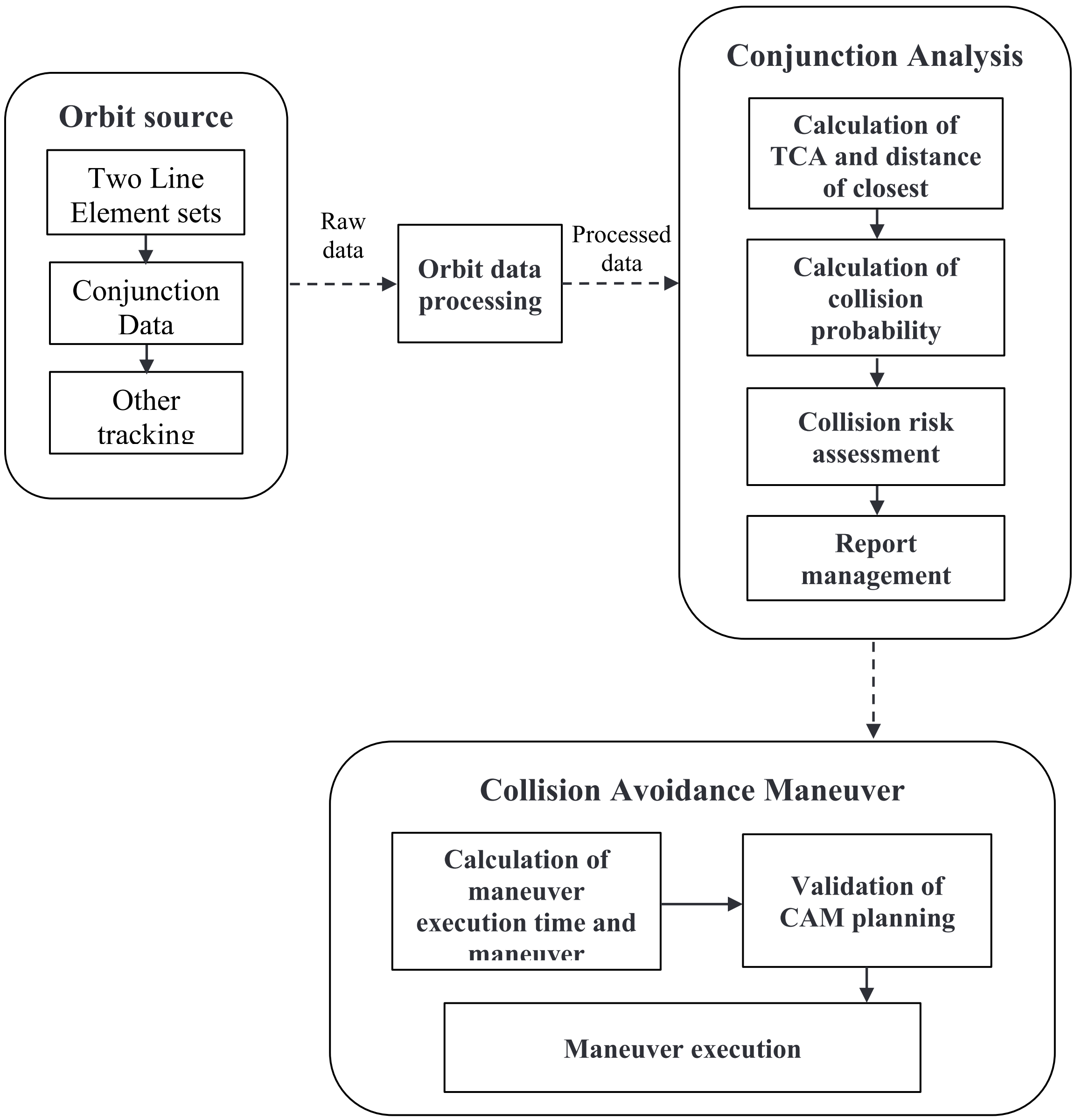


**Fig. 2. 7 Flowchart illustrating the process flow that collectively involves CA and CAM**

Upon getting notified, the satellite operator immediately initiates the standard procedure of a detailed conjunction assessment in order to decide quickly whether to perform avoidance maneuver or not. The following flowchart given in Figure 2.7 illustrates the process flow involved combinedly in conjunction analysis and planning of collision avoidance maneuver.

Due to a large amount of debris in space performing collision risk analysis of all the object along a period on the order of several days is a computationally intensive and is beyond the scope of this work. Hence, for this study, collision risk cases from previous years are arbitrarily chosen.

### 2.6.1 CALCULATION OF TIME OF CLOSEST APPROACH AND MISS DISTANCE

The calculation of closest approach time (TCA) and the miss distance can be formulated as an optimization problem [36] aimed at determining the global minimum of the modulus of the separation distance between the two objects under study. If $\boldsymbol{r_s}(t)$ and $\boldsymbol{r_d}(t)$ defines the position of the satellie and the debris at any time $t$ in the ECI frame, then the minimization function can be written as

$$J = |\boldsymbol{r_d}(t) - \boldsymbol{r_s}(t)| = \left[\left(\boldsymbol{r_d}(t) - \boldsymbol{r_s}(t)\right).\left(\boldsymbol{r_d}(t) - \boldsymbol{r_s}(t)\right)\right]^{1/2} \tag{2.11}$$

For a given conjunction pair, first the initial position vectors of the satellite $\boldsymbol{r_S}(t_0)$ and the debris $\boldsymbol{r_d}(t_0)$ at time $t_0$ are used to determine their orbits, respectively. These orbits are then propagted forward using numerical propagator until the point at which the relative distance becomes closer to zero. The corresponding time is the time of closest approach $t_{ca}$ and the distance is the miss distance $r_{rel}(t_{ca})$. The procedure is repeated inorder to re-calculate the new time of closest approach, after applying $\Delta v$, since the trajectory of the maneuverable object (satellie) will be altered.

### 2.6.2 CALCULATION OF COLLISION PROBABILITY

The collision probability is one of the fundamental criteria to be computed for performing conjunction analysis as well as collision avoidance maneuver planning. Ideally, the collision between a satellite and a debris will take place whenever their relative distance $r_{rel}$ during the time of closest approach $t_{ca}$ is below their combined spherical object radius $\rho_c$ [9]. If $\boldsymbol{r_d}$ and $\boldsymbol{r_s}$ describe the positions of the satellite, then at $t_{ca}$, the collision occurs when:

$$r_{rel}(t_{ca}) = |\boldsymbol{r_d}(t_{ca}) - \boldsymbol{r_s}(t_{ca})| < \rho_c \tag{2.12}$$

The combined object radius is expressed as:

$$\rho_c = \rho_s + \rho_d \tag{2.13}$$

where $\rho_s$ and $\rho_d$ are spherical object radii of the satellite and debris.

As mentioned earlier, the calculation of collision probability between two objects is based on probability density function (PDF) that follows Gaussian distribution [13]. The PDF function is a three-dimensional joint distribution function $f_3(\boldsymbol{r_{rel}})$ that describes the probability of relative position of the debris with respect to the satellite.

$$f_3(\boldsymbol{r_{rel}}) = \frac{1}{\sqrt{(2\pi)^3|C_{3\text{x}3}|}} \exp\left(-\frac{1}{2}\,\boldsymbol{r_{rel}}^{\boldsymbol{T}}\, {C_{3\text{x}3}}^{-1}\, \boldsymbol{r_{rel}}\right) \tag{2.14}$$

$C_{3\text{x}3}$ is the combined covariance matrix, where the uncertainties of the two objects are uncorrelated [35]. The probability of collision is given by the triple integral over the volume $V$ swept by a sphere of radius $\rho_c$.

$$P_c = \iiint_V f_3(\boldsymbol{r_{rel}})\, dV \tag{2.15}$$

Thus, based on the assumption of rectilinear motion, the problem is reduced to a two-dimensional PDF for which the volume swept by the combined radius becomes a circular cylinder extending along the $\eta$-axis perpendicular to the encounter ($\xi$- $\zeta$) plane.

$$f_2 = \frac{1}{2\pi\sigma_\xi\sigma_\zeta\sqrt{1-\rho_{\xi\zeta}{}^2}} \exp\left\{-\frac{1}{2(1-\rho_{\xi\zeta}{}^2)}\left[\left(\frac{\xi-\xi_e}{\sigma_\xi}\right)^2 + \left(\frac{\zeta-\zeta_e}{\sigma_\zeta}\right)^2 - 2\rho_{\xi\zeta}\left(\frac{\xi-\xi_e}{\sigma_\xi}\right)\left(\frac{\zeta-\zeta_e}{\sigma_\zeta}\right)\right]\right\} \quad (2.16)$$

where, $\sigma_\xi$ and $\sigma_\zeta$ denote the standard deviations along $\xi$-axis and $\zeta$-axis, $\rho_{\xi\zeta}$ the non-diagonal component, and $\xi$ and $\zeta$ the distance from the center in the direction of each axis. The combined covariance matrix that contains the positional uncertainties can be written as:

$$C_{2\text{x}2} = C_{\xi\zeta} = \begin{bmatrix} \sigma_\xi{}^2 & \rho_{\xi\zeta}\sigma_\xi\sigma_\zeta \\ \rho_{\xi\zeta}\sigma_\xi\sigma_\zeta & \sigma_\zeta{}^2 \end{bmatrix} \quad (2.17)$$

As mentioned in the literature study, there are several ways to evaluate this two-dimensional integral problem, however, so far no closed-form solution has been developed. One way to solve this problem is to use Rician distribution instead of Gaussian distribution, a method developed by Chan [20]. Rician or Rice distribution is generally used in the applications such as detection of signals in the presence of noise. As a result, Chan developed an analytical expression for the Rician integral that yields an infinite series expression which converges to all sorts of collision parameter values ($1\,m \leq R_c \leq 100\,m,\quad 10\,m \leq D_m \leq 100\,km,\quad 1\,km \leq \sigma \leq 10\,km$).

$$P_c = exp^{\left(-\frac{v}{2}\right)}.\sum_{m=0}^{\infty}\left[\left(\frac{v^m}{2^m.m!}\right).\left(1 - exp^{\left(-\frac{u}{2}\right)}\sum_{k=0}^{\infty}\left(\frac{u^k}{2^k.k!}\right)\right)\right] \quad (2.18)$$

where,

$$u = \frac{\rho_c{}^2}{\sigma_\xi\sigma_\zeta} \quad (2.19)$$

$$v = \left(\frac{\xi-\xi_e}{\sigma_\xi}\right)^2 + \left(\frac{\zeta-\zeta_e}{\sigma_\zeta}\right)^2 \quad (2.20)$$

## 2.7 OREKIT – ORBITS EXPLORATION KIT

The work described in this thesis are implemented in Python programming environment while the astrodynamics is dealt with using OREKIT [44], a high-fidelity simulation toolkit developed by CS-Systems, a French-based company. OREKIT is an open source low-level space dynamics library written in Java that provides various classes for representation of orbits, dates, attitudes, frames, and algorithms to handle conversions, orbit propagations, force models and so on. OREKIT has been successfully used in the European Space Agency (ESA) and the Centre National d'Études Spatiales (CNES, the French Space Agency) for monitoring the real-time simulations for Automated Transfer Vehicle (ATV) and the International Space Station (ISS) missions. OREKIT is utilized in this study to determine realistic state vectors using its propagator and force model modules and to visualize and validate the generated optimal results. The following sub-sections details about the modules and the functionalities that are implemented.

### 2.7.1 ORBIT DETERMINATION AND ORBIT PROPAGATION

Orbit determination is the process of estimating the state (position and velocity) of an orbiting object through observations that include measurements provided by the GPS Navigation sensors [45]. Whereas, orbit propagation is a mathematical process of estimating the future state of an object, whose initial states are obtained from the past observations. It is a technique with which a satellite's state around a celestial body is determined for a specific time. Over the years, the demand for high precision orbit propagation has lead to the development of various computational models which can be broadly classified into three different categories: Numerical, Analytical and Semi-analytical propagation [46]. However, no approach is still capable of determining accurate results that can depict the reality in every detail.

Numerical propagation provides a means of propagating the state by directly integrating the equations of motion. Numerical propagation is the most computationally expensive method, despite, for any computation model, a trade-off must be established between accuracy and it computation cost. While generally, it involves complex computations, numerical propagation is the most accurate propagation technique which can be conveniently used for studies related to space situational awareness [47] (such as collision risk analysis and collision avoidance maneuver planning). By using the fundamental equations of motion, the position and velocity of an object can be determined for a given time using the information based on the previous step. Thus, it requires both the previous output as well as a continuous iterative process in order to obtain consecutive steps and further the accuracy of the solution can be improved by decreasing the step size i.e., the more computational effort is required to achieve the desired accuracy. Numerical propagation techniques [48] rely on ODE integrators (such Dormand-Prince integrator and Runge-Kutta integrator) that helps in adjusting the step size dynamically.

In this study, the DormandPrince853 integrator, delivered by OREKIT, is implemented in which the integrator module requires three parameters to be specified: the minimum and maximum integration step in seconds, and the position tolerance in meters. DormandPrince853 is an embedded Runge-Kutta integrator of the order 8 (5,3) [49]. It uses 12 function evaluations per step for integration and 4 evaluations for interpolation. This method is basically a modified version of 8(6) method where it uses 5$^{th}$ order error estimator with 3$^{rd}$ order correction, as the original method had several flaws in it [50].

Analytical propagation technique uses closed-form time-dependent mathematical equations to determine directly the object's position and velocity at any desired time. Unlike Numerical propagators, analytical propagators are computationally faster that can describe the state of an object at any given time in a much simpler manner. However, the accuracy of the analytical model depends on the underlying equations implemented and often it requires to be revised inorder to achieve the desired accuracy. TLE-propagator, also known as Simplified General Perturbations (SGP4) propagator, an analytical propagation technique commonly used for propagating the objects using two-line element (TLE) sets. TLE-propagator is initially developed by North American Aerospace Defence Command (NORAD) specifically to be used for propagating TLE data. It uses a simple drag model that can describe secular and periodic variations due to the Earth's zonal harmonics $(J_2)$ and the atmospheric drag [51]. OREKIT provides an highly efficient TLE-propagator [52] that can compute the state vectors of the object at any time and guarantees maximum accuracy with its precision not exceeding 2 km. In this work, the TLE-propagator is used to test and compare the efficacy of the methods proposed.

Semi-analytical propagation, a blend of both numerical and analytical methods, widely used for the cases where long-term orbit propagation is required. They consider only long-term perturbation effects that are described analytically and incorporate numerical integration that allows for relatively accurate orbit determination for larger time steps. Semi-analytical propagators are more accurate compared to analytical propagator as well as faster compared to numerical propagator. The use of semi-analytical propagator is beyond the scope of this thesis.

### 2.7.2 PERTURBATION FORCES

Practically, in the real world, several external forces act on a space object that tends to deviate its orbit from its original form. These forces emerge from distinct sources and perturb the object's orbital parameters with different intensities. The main idea of force models is to reproduce these perturbation forces as precise as possible. Several force models exist that can approximate these perturbation forces [30]. Generally, perturbation forces are categorized into two variants: secular and periodic perturbations. Secular perturbations cause a continuous deviation on the orbit such that they induce long-term effects; for instance, the atmospheric drag gradually decreases the semimajor axis of the orbiting object such that its altitude steadily decreases until it reaches the Earth's atmosphere. Periodic perturbations are those that cause the orbital elements to fluctuate around their mean values; for example, the gravitational pull from the Sun and the Moon causes the inclination of the object in GEO to oscillate over a period until it decays. The following subsections discuss some of the most prominent perturbation forces in brief.

**Earth's gravitational potential**

Ideally, it is considered that the Earth is a perfect sphere with a uniformly distributed gravitational potential. However, in reality, the Earth is flattened at its poles such that the equator featuring a slight bulge. In addition, the Earth's mass is not equally distributed such that the orbiting object's orbit experiences perturbations. This irregular distribution of the

Earth's mass affects the orbital elements, particularly the RAAN and perigee argument of the orbit. The perturbing effects due to the non-uniform gravitational potential of the Earth is modeled as Spherical Harmonics [30], which is divided into zonal harmonics, tesseral harmonics, and sectoral harmonics. Figure 2.8 [51] depicts the three different sectional harmonics (left-secular, middle-sectoral and right tesseral). The equation for the gravitational potential [30], helps determine the gravitational attraction on an orbiting object due to the uneven mass distribution of the Earth.

$$U = \frac{\mu}{r}\left\{1 + \sum_{l=2}^{\infty}\sum_{m=0}^{l}\left(\frac{R_E}{r}\right)^l P_{l,m}\sin(\phi)\left(C_{l,m}\cos(m\lambda) + S_{l,m}\sin(m\lambda)\right)\right\} \tag{2.21}$$

where, $P_{l,m}$ represents the Legendre polynomials associated with the object's postion, $C_{l,m}$ and $S_{l,m}$ are the harmonics coefficients that describe the the Earth's deviation from a perfect sphere, $l$ and $m$ are the indices of the summation equation that designate degree and order, respectively and lastly $\lambda$ and $\phi$ represent the longitude and lattitude coordinates, respectively [53]. In this work, only $J_2$ – perturbation effect that accounts for secular variations of Earth's zonal harmonics is considered. The zonal harmonics are described by the zeroth order ($m = 0$) and can be derived from the equation (2.16) [30]:

$$-C_{l,0} = J_l \tag{2.22}$$

After a series of calculations, the value for $J_2$ is $1.0826269$ x $10^{-3}$.

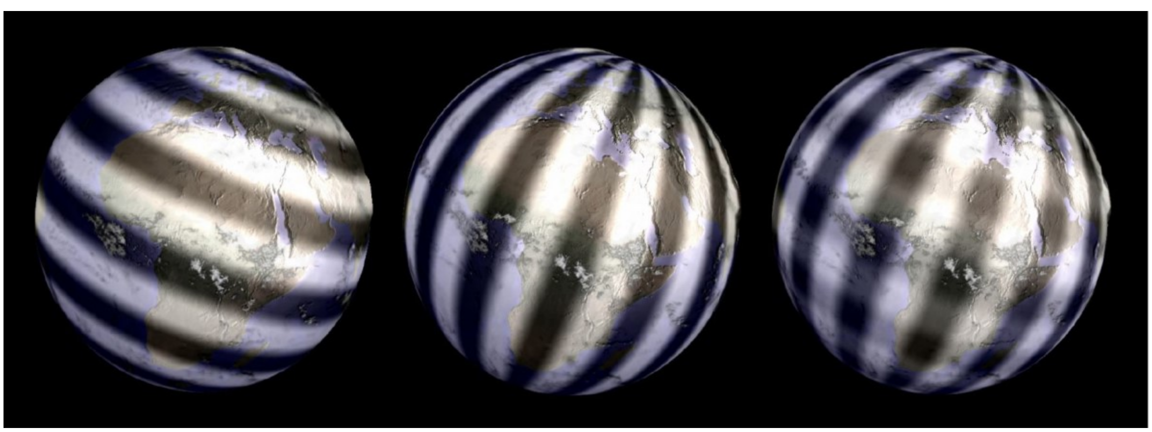

**Fig. 2. 8 Zonal (left), Tesseral (middle) and Sectoral (right) harmonics [51]**

**Atmospheric drag**

The motion of an object orbiting around the Earth can get disrupted by the atmospheric particles thus inducing drag force which retards the object's motion. At low altitude, the effects due to atmospheric drag are more dominant than that of Earth's gravitational harmonics and affect primarily the semimajor axis and the eccentricity of the object's orbit [30]. Atmospheric drag is a nonconservative perturbation because the velocity gets affected thus resulting in loss of energy. The acceleration due to atmospheric drag can be expressed as:

$$\boldsymbol{a} = -\frac{1}{2B}\rho v_{rel}^2 \frac{\boldsymbol{v_{rel}}}{|\boldsymbol{v_{rel}}|} \tag{2.23}$$

where, $\boldsymbol{v_{rel}}$ is the object's velocity vector relative to the atmosphere (Earth's atmosphere), $\rho$ is the atmoshpheric density, and $B$ is the ballistic coefficient (BC) that describes the susceptibility of the satellite to overcome the atmosphere and is a function of mass of the satellite $m$, drag coefficient $C_D$ and the cross-sectional area $A$ normal to the satellite's velocity.

$$B = \frac{m}{C_D A} \tag{2.24}$$

**Third body perturbations**

In addition to the Earth's gravitational attraction, objects orbiting the Earth also exhibits gravitational pull from other massive bodies in its vicinity. The most influential ones are the Sun, because of its enormous mass and the Moon as it is closer to the Earth. Unlike atmospheric drag, third body perturbation is conserved because there is no account of loss of energy. The perturbations from the Sun and the Moon cause long-term effects, both periodic and secular, on all the orbital elements except the semimajor axis. The solar effect tends to precess the object's orbit about the pole of the ecliptic and its amplitude is smaller compared to lunar which regresses the orbit about an axis normal to the orbital plane of the Moon [30].

OREKIT provides built-in force models [54] that allow to configure and simulate the effects of the above perturbation effects for propagating the orbits of objects under study. Using the data available from CDM, the state vectors of the object are defined for both satellite and the debris and are simulated using the numerical propagator; the numerical simulations involve testing of the proposed algorithms under the Earth gravitational zonal harmonics and third body attraction force models provided by OREKIT.

In general, the propagation of the orbit of an object in space is carried out with regards to time, particularly known as epoch time, so as to determine the state vector of the object based on the epoch time and not with respect to the true anomaly. Likewise, OREKIT accepts only the epoch time at which the state of an object can be determined, hence, the state vectors involved in the formulations in this study are referenced with respect to time. However, to simplify the calculations, in this work, the time $t$ is converted into a dimensionless term $\tau$ referred to as *orbits*.

$$\tau = \frac{t}{T} \tag{2.25}$$

where $T$ is the orbital period of the object under study.

## 2.8 SELF-ADAPTIVE DIFFERENTIAL EVOLUTION

Generally, trajectory optimization problems are designed with the aim of minimizing or maximizing some kind of performance measures without violating the constraints. Several distinctive optimization techniques have been successfully applied to solve a wide range of trajectory optimization problems. In recent years, evolutionary algorithms have been considered as powerful and efficient optimization techniques [55] that have been successfully used in various problem domains.

Differential Evolution (DE), a variant of the evolutionary algorithm, is a heuristic direct search method and is well-known for its success in CAM optimization problems [56]. DE updates the parameter vector by adding the weighted difference of two or more randomly generated population vectors. The newly generated member then replaces the old when its objective function has a better value (lower value). However, DE is sensitive to its control parameters: mutation factor $(F)$ and crossover ratio $(C_r)$. The values of these control parameters have to be set up manually which is a time consuming process, instead, if the parameters $C_r$ and $F$ are properly adapted, then the performance of DE can be significantly improved. This type of DE which adopts self-adaptation of its control parameters is known as Self-Adaptive Differenctial Evolution (SADE).

Several authors have contributed in developing an effective strategy to incorporate self-adaptive scheme on DE. In this work, the one proposed by Elsayed et al. [57] is used. The algorithm considers a multiple strategy techniques comprising four different combinations of one mutation strategy and one crossover operator in which each combination has its own set of sub-population that adapts based on the reproductive success of the search operators. The algorithm continues to evolve until the stopping criterion is satisfied. The steps involved in SADE are summarized in Table 2.1.

| | |
|---|---|
| | **Input:** The number of individuals $\boldsymbol{N}$ contained by the population, maximum iteration, constraint tolerances and bounds for optimization parameters |
| | **Output:** Global best solution (minimum) |
| **Step 1:** | **Initialization:** In generation $g = 0$, generate initial random population of size $N$. |
| **Step 2:** | Divide N into 4 sub-populations $p_i$ of size $n_i = N/4, \quad i = 1,2,3,4.$ |
| **Step 3:** | **for i = 1 : 4,** |
| **Step 4:** | Evolve the $n_i$ individuals using the self adaptive parameters $F$ and $C_r$ allocated for $p_i$. |
| **Step 5:** | Generate offsprings and update the fitness evaluations. |
| **Step 6:** | Sort the individuals according to the fitness function values and constraint violations. |
| **Step 7:** | Estimate the improvement index, based on which the size of the subpopulation is either altered or kept unchanged. |
| **Step 7a:** | Replace 3 worst individuals with 3 best solutions (best solution among the subpopulations are exchanged). |

| | |
|---|---|
| **Step 7b:** | **if** there exists any redundant vector, **then** replace it by a generated random vector. |
| **Step 8:** | Store the best individual for each operator. |
| **Step 9:** | **if $g$ > 1, then** |
| **Step 9a:** | Update the subpopulation. |
| **Step 10:** | **if** the termination criterion is satisfied, **then** Stop<br>else, set $g = g + 1,$ and go to **Step 4** |

**Table 2. 1 Self-Adaptive Differential Evolution algorithm [57]**

The algorithm for SADE is readily available in PaGMO [58] library, which refers to Parallel Global Multiobjective Optimizer, a scientific library developed by ESA to handle massively parallel optimization environments. It provides state-of-the-art optimization algorithms that allow being coupled with additional meta-algorithms to build one super-algorithm, thus exploiting the collaboration between algorithms to improve the efficacy of the optimization problem. In simple words, the library offers functionalities that handle asynchronous evolution (or optimization) of the population using meta-algorithms in the background so as to achieve better convergence rate. For more information about PaGMO and the usage of SADE and its functionality, refer the PaGMO website.

# THREE-IMPULSE MANEUVER OPTIMIZATION

## 3.1 OVERVIEW

This chapter provides a detailed explanation pertaining to the three-impulse maneuver optimization method proposed in this thesis. The schema of the three-impulse method is established as a two-stage process in which the first stage involves evasion of predicted collision between the satellite and the debris and the second stage for orbital re-entry by solving the Lambert's problem. The following sections discuss in detail about the formulations involved in the three-impulse method, including the definition of optimization parameters and the constraints. Lastly, the numerical results are presented that validate the adequacy of the method by using Self-Adaptive Differential Evolution (SADE) algorithm.

## 3.2 PROBLEM DEFINITION

The problem consists in determining an optimal trajectory between two points: a) departure point - the orbital location at which the satellite departs from its nominal orbit, and b) the arrival point - the orbital location at which the satellite re-enters back. The problem involves calculating the corresponding $\Delta v$ at the desired maneuver execution times while obeying the mission constraints that monitors the satellite's safety. Evidently, the design of this approach comprises of three impulse maneuvers in total: the first impulse known as initial avoidance maneuver executed within a brief period before the time of predicted collision, the second during the time of the new closest approach and finally, the third during orbital re-insertion. The goal here is to minimize the total-$\Delta v$ by implementing numerical optimization technique. Thus, the objective function for the three-impulse collision avoidance maneuver can be expressed as:

$$J = \Delta v_{tot} = \{|\Delta \boldsymbol{v_0}|\}_{avoid} + \{|\Delta \boldsymbol{v_1}| + |\Delta \boldsymbol{v_2}|\}_{re-entry} \tag{3.1}$$

The optimization problem involves minimizing the objective function given in equation (3.1), by selecting the optimal values of the decision parameters using Self-Adaptive Differential Evolution. The trajectory is optimized by employing the Lambert's problem to determine a fuel economical path. The central idea underlying the optimization problem is contained in the constraint that governs the trajectory optimization aimed at maintaining a safe separation distance between the satellite and debris during the time of closest approach. The following sections detail the calculations involved in the problem structure.

## 3.3 INITIAL AVOIDANCE MANEUVER

The initial avoidance maneuver aims at displacing the maneuverable object (satellite) away from the approaching derelict object (debris) and thus reducing the risk of collision during the time of closest approach. Typically, optimization of collision avoidance maneuver [36] involves finding an optimal location where the maneuver must be applied, the magnitude of the thrust and its direction such that minimal fuel objective must be achieved while maintaining a safe distance of separation between the two approaching objects. Hence, the following three characteristics are to be examined when planning for avoidance maneuver:

i. the maneuver execution time,
ii. the magnitude of the impulse used in the maneuver, and
iii. the direction of application of the impulse.

The orbital location at which the avoidance maneuver must be applied is determined by its execution time, $t_0$. Normally, avoidance maneuvers are performed several hours [59] before the time of predicted collision and it is clear that the satellite becomes inoperative during that time interval. Moreover, if the notification time is less than few orbits before the collision, the time interval within which the maneuver must be applied for collision avoidance will eventually become shorter [60]. With these in mind, the optimal location $\Delta\tau_{am}$ (defined as in orbits) at which the maneuver can be applied is limited up to one orbit i.e., less than 2 hours for Low Earth Orbit satellites, such that the satellite stays in the transfer orbit only for a brief duration.

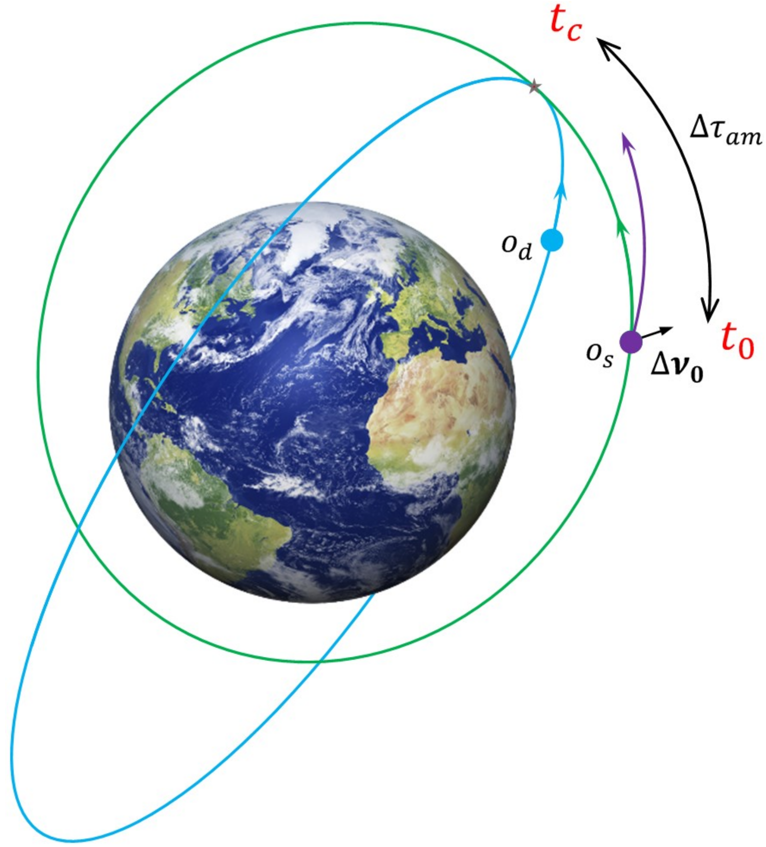


**Fig. 3. 1 Illustration of avoidance maneuver time**

Consider a case where two objects, a satellite $o_s$ and a debris $o_d$ are traveling at velocities $\boldsymbol{v_s}(t)$ and $\boldsymbol{v_d}(t)$, respectively and are predicted to collide at time $t_c$ (Figure 3.1). If $T_s$ is the orbital period of the satellite in its nominal orbit, then the maneuver execution time for the initial avoidance maneuver can be expressed as:

$$t_0 = t_c - (\Delta\tau_{am} \text{ x } T_s) \tag{3.2}$$

where, $\Delta\tau_{am}$ defines the orbital location (in orbits).

$$\Delta\tau_{am} = \frac{\Delta t_{am}}{T_s} \tag{3.3}$$

It is noted that the maneuver execution time for the initial avoidance maneuver is referenced with respect to the time of collision. This is because, in this work, the CDM data is used as a primary source of data that contains only the information that is computed with regards to the time of predicted collision i.e., the state vectors of the satellite and the debris at $t_c$. For this purpose, the formulations involved in this method are referenced with respect to collision time and thereby to determine the state of the satellite during the time of initial avoidance maneuver $t_0$, the state vectors at $t_c$ are propagated backwards up to $t_0$ and then propagated forward with after applying $\Delta v_0$. If $\Delta v$ is the magnitude of the avoidance impulse required to be applied at $t_0$, then the norm of the initial avoidance maneuver $\Delta \boldsymbol{v_0}$ can be expressed as:

$$|\Delta \boldsymbol{v_0}(t_0)| = \Delta v \tag{3.4}$$

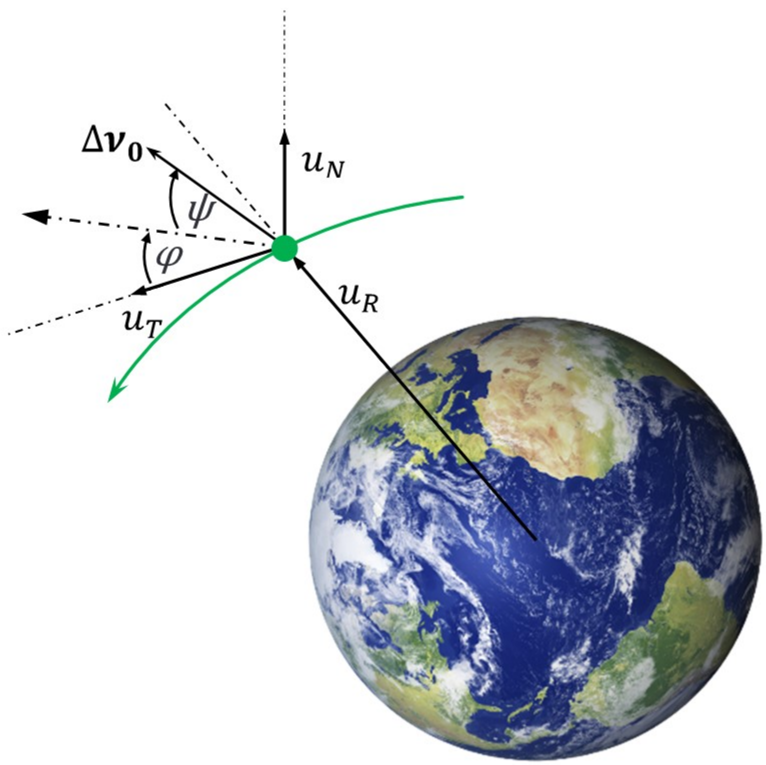


**Fig. 3. 2 Illustration of thrust direction**

Once the maneuver location and the magnitude are established, the third criterion is the direction of the maneuver. To facilitate the intricacy in finding an optimal direction, the components of $\Delta \boldsymbol{v_0}$ are first divided in to in-plane and out-of-plane components. This becomes possible by expressing the direction components in the body-fixed local orbiting frame, Radial-Transverse-Normal reference frame. Here, the components of impulse in the radial and transverse directions contribute to the in-plane change while the normal direction corresponds to the out-of-plane.

$$\Delta \boldsymbol{v_0} = \begin{Bmatrix} \Delta v_R \\ \Delta v_T \\ \Delta v_N \end{Bmatrix} = \begin{Bmatrix} \Delta v \ cos(\psi) \, cos(\varphi) \\ \Delta v \ cos(\psi) \, sin(\varphi) \\ \Delta v \ sin(\psi) \end{Bmatrix} \tag{3.5}$$

where $\varphi$ and $\psi$ are the in-plane and out-of-plane rotation angles in the RTN frame. Figure 3.2 demonstrates the geometry of the avoidance maneuver in the RTN reference frame. Using the direction cosine matrix $M_{RTN \to ECI}$ (section 2.2.2) that establishes the relationship between the Radial-Transverse-Normal reference frame and the Earth Centered Inertial frame (ECI), $\Delta \boldsymbol{v_0}$ can be written as:

$$\Delta \boldsymbol{v_0} = \begin{Bmatrix} \Delta v_X \\ \Delta v_Y \\ \Delta v_Z \end{Bmatrix} = M_{RTN \to ECI} \ \text{x} \ \begin{Bmatrix} \Delta v_R \\ \Delta v_T \\ \Delta v_N \end{Bmatrix} \tag{3.6}$$

# 3.4 BI-IMPULSE MANEUVER FOR ORBITAL RE-ENTRY

After circumventing the approaching obstacle, it is desired to return the satellite back to its nominal orbit. For this purpose, a well-known orbital boundary-value problem in the field of astrodynamics known as the Lambert's problem is employed. The maneuver dynamics involved in the bi-impulsive maneuver is discussed in the following subsections.

## 3.3.1 LAMBERT'S PROBLEM

J. H. Lambert devised a theorem based on conic sections [21]. The theorem states that in a two-body problem, the transfer time required to travel from one point to another depends only on the length of the chord joining the points, the semimajor axis and the sum of the radii from the focus to the initial and final point. Let us consider an orbital transfer problem where the satellite is required to transfer from initial orbit to final orbit. Figure 3.3 shows the geometry of this transfer problem. The problem involves determination of the transfer orbit connecting the two position vectors $\boldsymbol{r_1}$ and $\boldsymbol{r_2}$, given a specified time interval $\Delta t_f$. If $c$ is the chord joining the points $P_1$ and $P_2$, $a$ is the semimajor axis of the transfer orbit then the time of flight between the two points becomes:

$$\Delta t_f = t_2 - t_1 = f(c, a, r_1 + r_2) \tag{3.7}$$

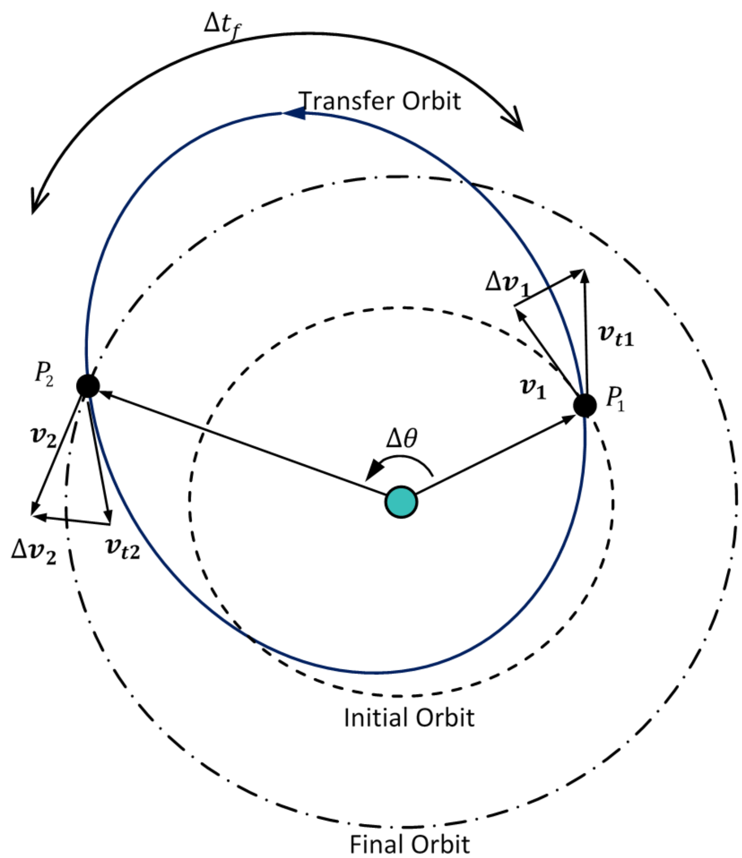


**Fig. 3. 3 Lambert's problem**

Initially, the satellite is in the initial orbit at $P_1$ with position $\boldsymbol{r_1}$ and velocity $\boldsymbol{v_1}$. It enters the transfer orbit with velocity $\boldsymbol{v_{t1}}$, upon applying the impulse $\Delta \boldsymbol{v_1}$ at time $t_1$. The satellite then continues to traverse in the transfer orbit until it reaches the final orbit at $P_2$ with position $\boldsymbol{r_2}$, where the velocity changes from $\boldsymbol{v_{t2}}$ to $\boldsymbol{v_2}$ due to the impulse $\Delta \boldsymbol{v_2}$. The equations for the chord length $c$ connecting two points $P_1$ and $P_2$ and the transfer angle $\Delta\theta$ between the two position vectors $\boldsymbol{r_1}$ and $\boldsymbol{r_2}$ can be expressed as:

$$cos(\Delta\theta) = \frac{\boldsymbol{r_1}.\boldsymbol{r_2}}{r_1 r_2} \tag{3.8}$$

$$c = \sqrt{{r_1}^2 + {r_2}^2 - 2r_1 r_2\, cos(\Delta\theta)} \tag{3.9}$$

Given the time interval $\Delta t_f$ from $P_1$ to $P_2$, the velocities $\boldsymbol{v_{t1}}$ and $\boldsymbol{v_{t2}}$ can be calculated by solving for $f$ and $g$ expressions. For more information related to the derivations involved in Lambert's problem, please refer to [21, 30]:

$$f = 1 - \frac{r_2}{p}(1 - \cos(\Delta\theta)) \tag{3.10}$$

$$\dot{f} = \sqrt{\frac{1}{p}} \tan\left(\frac{\Delta\theta}{2}\right)\left(\frac{1 - \cos(\Delta\theta)}{p} - \frac{1}{r_1} - \frac{1}{r_2}\right) \tag{3.11}$$

$$g = \frac{r_1 r_2 \sin(\Delta\theta)}{\sqrt{\mu p}} \tag{3.12}$$

$$\dot{g} = 1 - \frac{r_1}{p}(1 - \cos(\Delta\theta)) \tag{3.13}$$

where $p$ is the semi-parameter whose equation for an elliptic orbit can be expressed as:

$$p = \frac{r_1 r_2 (1 - \cos(\Delta\theta))}{r_1 + r_2 - 2\sqrt{r_1 r_2}\, cos\left(\frac{\Delta\theta}{2}\right) cos\left(\frac{\Delta E}{2}\right)} \tag{3.14}$$

Then, the equations for the velocities $\boldsymbol{v_{t1}}$ and $\boldsymbol{v_{t2}}$ are:

$$\boldsymbol{v_{t1}} = \frac{\boldsymbol{r_2} - f\boldsymbol{r_1}}{g} \tag{3.15}$$

$$\boldsymbol{v_{t2}} = \frac{\dot{g}\boldsymbol{r_2} - f\boldsymbol{r_1}}{g} \tag{3.16}$$

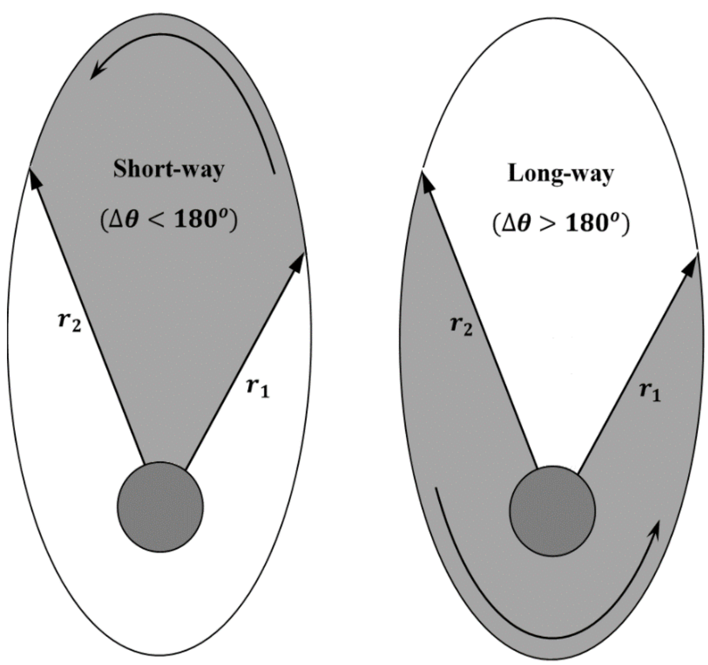


**Fig. 3. 4 Short-way (left) path and long-way (right) path**

Finally, as for the direction of the flight is concerned, there exist two possibilities depending upon the transfer angle. If $\Delta\theta < 180^o$ then the path is known as short-way, whereas, it moves along the long-way path if $\Delta\theta > 180^o$. Figure 3.4 demonstrates the direction of flight in a typical Lambert's problem.

Thus, by varying the transfer period and the transfer angle, a wide range of transfer paths is determined from which the fuel optimal solution can be found. The goal is to determine a trajectory which saves fuel cost by implementing numerical optimization technique.

### 3.3.2 IMPLEMENTATION

After applying the initial avoidance maneuver, the state vectors at $t_0$ become $\boldsymbol{r_0}$ and $\boldsymbol{v_0}'$ (a prime represents state in first transfer orbit, $O_{TF1}$) in the Earth Centered Inertial (ECI) reference frame that define the $O_{TF1}$ orbit. Now, the position and velocity of the satellite at any point in $O_{TF1}$ can be found by propagating forward the initial states and consequently, the new closest approach $t_{ca} = t_1$ can be found. The time of closest approach is not to be confused with that of the time of predicted collision $t_c$. Although this closest approach time lies close to the collision time as it is expected to procure the transfer orbit closer to the nominal orbit. The position and velocity of the satellite in the first transfer orbit during the time of closest approach $t_1$ becomes $\boldsymbol{r_1}'$ and $\boldsymbol{v_1}'$, immediately before initiating the impulse $\Delta\boldsymbol{v_1}$ for orbital re-entry. While in the second stage, immediately after applying the initial impulse $\Delta\boldsymbol{v_1}$ at $t_1$, the new state of the satellite becomes $\boldsymbol{r_1}''$ and $\boldsymbol{v_1}''$ (a double prime represents state in second transfer orbit) which can be written as:

$$\boldsymbol{r_1}'' = \boldsymbol{r_1}' \tag{3.17}$$

$$\boldsymbol{v_1}'' = \boldsymbol{v_1}' + \Delta\boldsymbol{v_1} \tag{3.18}$$

During orbital re-entry, the Lambert's problem is established with the initial and final points and the transfer time. The initial point $\boldsymbol{r_1}''$ is the position of the satellite during the time of closest approach in the first transfer orbit which can be determined by propagating simultaneously both the satellite's first transfer orbit and the object's nominal orbit until the point of closest approach. Thus, the problem gets break down to two unknowns: a) the arrival/re-entry location of the satellite in its nominal orbit, $\boldsymbol{r_2}''$ and b) the time of re-entry.

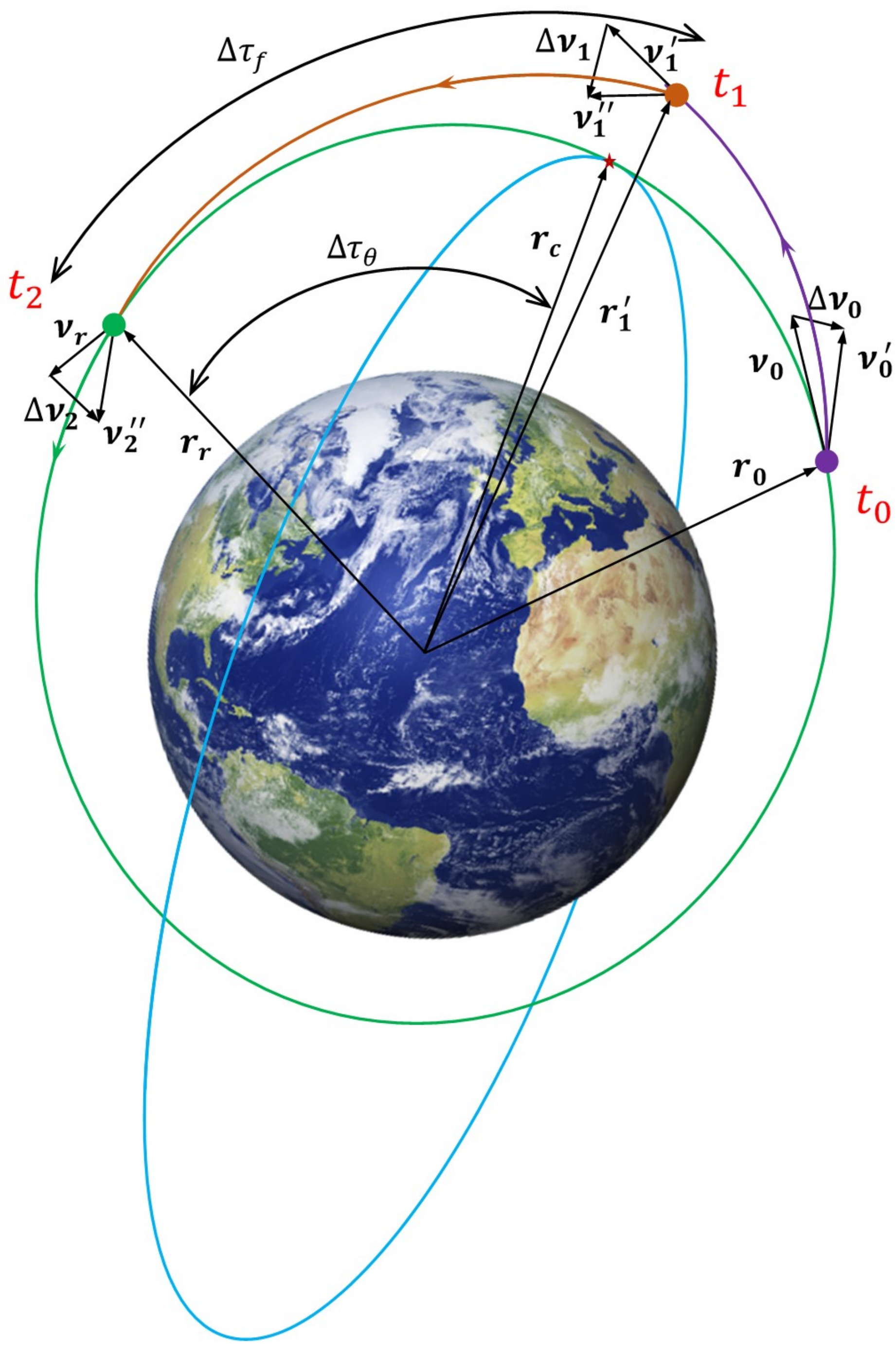


**Fig. 3. 5 Maneuver geometry involved in three-impulse maneuver method**

In order to define the orbital location of the satellite at which it re-enters the nominal orbit, the change in true anomaly $\Delta\theta$ can be used where the point of re-entry must be referenced with respect to the point of predicted collision. If $\theta_c$ represents the true anomaly of the satellite's nominal position during the predicted collision:

$$\boldsymbol{r_c} = \boldsymbol{r}(\theta_c) \tag{3.19}$$

and $\theta_r$ represents the true anomaly at the point of re-entry in the nominal orbit such that

$$\boldsymbol{r_2}'' = \boldsymbol{r}_r = \boldsymbol{r}(\theta_r) \tag{3.20}$$

then the equation for the change in true anomaly can be written as:

$$\Delta\theta = \theta_c - \theta_r = \cos^{-1}\left[\frac{\boldsymbol{r_c}.\boldsymbol{r_r}}{r_c r_r}\right] \tag{3.21}$$

The change in true anomaly can be expressed as a dimensionless angle, $\Delta\tau_\theta$, ranging from 0 to 1 orbits. Thus, equation 3.21 can be re-written as

$$\Delta\tau_\theta = \frac{\Delta\theta}{2\pi} = \frac{1}{2\pi}\cos^{-1}\left[\frac{\boldsymbol{r_c}.\boldsymbol{r_r}}{r_c r_r}\right] \tag{3.22}$$

Now, for the time at which the satellite must re-enter, $t_2$, can be defined by the transfer time, $\Delta t_f$, required to traverse the satellite from $\boldsymbol{r_1}''$ to $\boldsymbol{r_r}$.

$$t_2 = t_1 + \Delta t_f \tag{3.23}$$

For simplicity, the transfer time $\Delta t_f$ is normalized to a dimensionless parameter $\Delta\tau_f$ ranging from 0 to 1 orbits that signifies the angle between the position $\boldsymbol{r_1}'$ of the satellite in the transfer orbit during the time of new closest approach $t_1$ and the re-entry position $\boldsymbol{r_r}$ at $t_2$:

$$\Delta\tau_f = \frac{\Delta t_f}{T_s} = \frac{1}{2\pi}\cos^{-1}\left[\frac{\boldsymbol{r_1}'.\boldsymbol{r_r}}{r_1'\, r_r}\right] \tag{3.24}$$

Figure 3.5 provides a detailed illustration of the maneuver geometry collectively involved in both initial collision avoidance and orbital re-entry. For the reader's convenience, the different orbits involved are distinguished as follows: a) the nominal orbit of the satellite is shown in green, b) the nominal orbit of the debris is in blue, c) the first transfer orbit after initial avoidance maneuver is in purple and d) the second transfer orbit involving Lambert's problem is shown in orange. The flowchart (Figure 3.6) illustrates the basic workflow involved in the three-impulse collision avoidance method. The equations for $\Delta\boldsymbol{v_1}$ and $\Delta\boldsymbol{v_2}$ can be written as:

$$\Delta\boldsymbol{v_1} = \boldsymbol{v_1}'' - \boldsymbol{v_1}' \tag{3.25}$$

$$\Delta\boldsymbol{v_2} = \boldsymbol{v_r} - \boldsymbol{v_2}'' \tag{3.26}$$

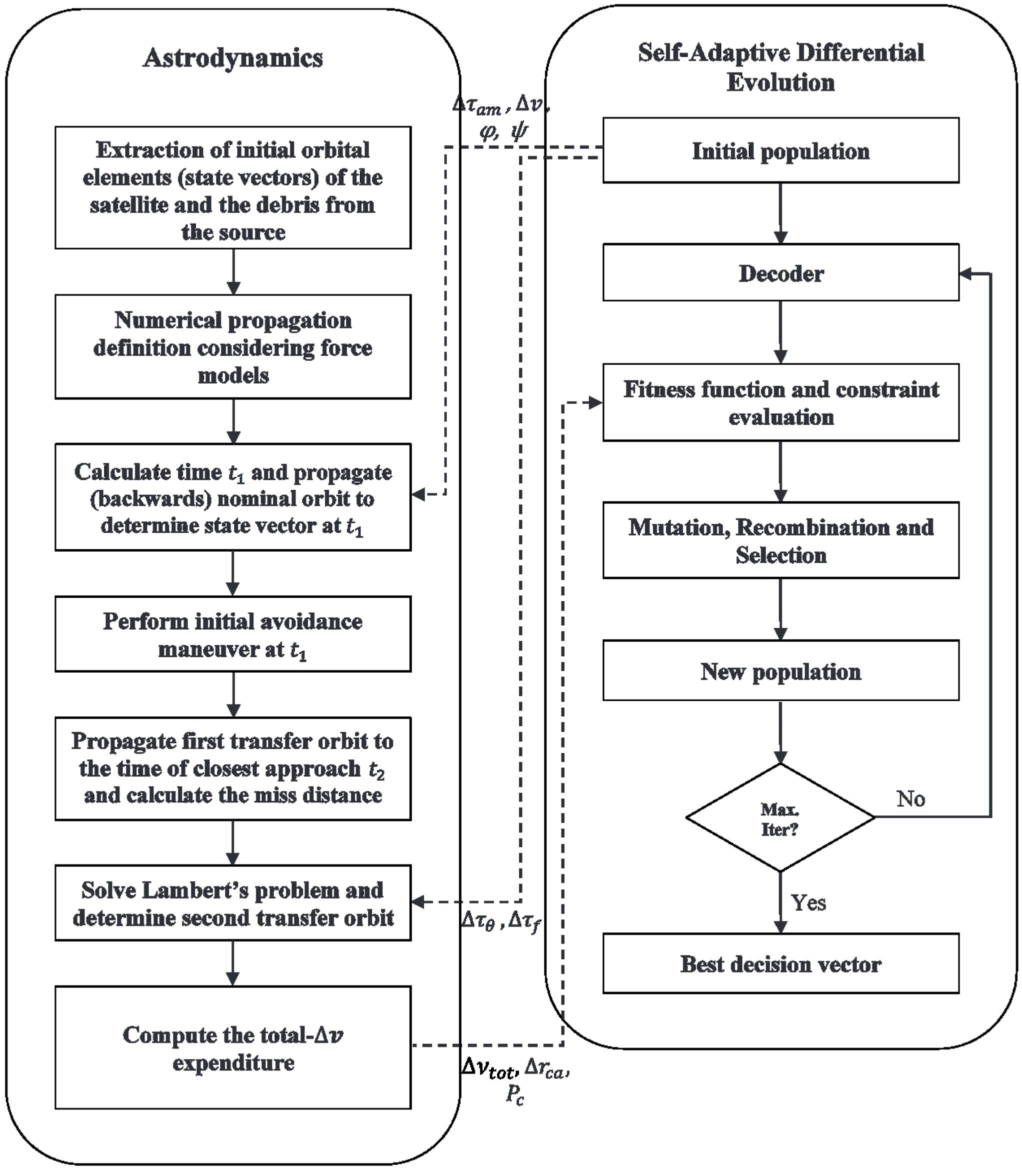


**Fig. 3. 6 Flowchart illustrating the workflow involved in Three-impulse collision avoidance maneuver method**

where $\boldsymbol{v_r}$ is the velocity of the satellite in the nominal orbit at the point of re-entry and can be obtained by propagating the nominal orbit from $t_c$ to $t_c + (\Delta\tau_\theta \,.\, T_s)$. Thus, by varying the following optimization parameters, a wide range of transfer paths can be generated from which the minimum-fuel solution can be determined:

i. Avoidance maneuver time, $\Delta\tau_{am}$ (orbits)
ii. Magnitude of the avoidance maneuver, $\Delta v$ (m/s)
iii. Direction of the initial impulse:

a. In-plane rotation angle, $\varphi$ (radians)

b. Out-of-plane rotation angle, $\psi$ (radians)

iv. Orbital location for re-entry, $\Delta\tau_\theta$ (orbits)

v. Time of re-entry, $\Delta\tau_f$ (orbits)

## 3.5 CONSTRAINTS

The purpose of designating the constraints is to ensure that the satellite is in a safe proximity during the closest approach. Ultimately this becomes possible by maintaining a safe distance of separation between the two approaching objects. In general, this problem is treated as an optimization problem aimed at: maximizing the miss distance and minimizing the collision probability while minimizing the fuel consumption [7, 9, 10, 12]. One crucial drawback in using such strategy is the linear dependence of the miss distance and collision risk with respect to the maneuver applied. Though fuel-optimal solution can be found, but it may not yield the actual fuel economical path, as the $\Delta v_0$ requirement tends to increase with regards to the displacement of the satellite in the encounter plane. In fact, the optimal solutions obtained from such methods may lead to larger deviations in terms of orbital parameters and will generate in larger values for $\Delta v$.

To overcome this drawback, the two influencing factors, miss distance, and collision probability are tackled as constraints in this study. As a result, the optimization problem becomes less complex, also a globally best minimum-fuel solution can be determined with minimal computational effort. The bounds for the constraints are based on the mission requirements and are ideally specified by the satellite operator.

### 3.5.1 MISS DISTANCE AND COLLISION PROBABILITY

With the applied avoidance maneuver, the resulting new time of closest approach, as described in section 2.6.1, can be determined by propagating the satellite's transfer orbit and the debris' nominal orbit simultaneously. As a result, the distance of separation (Figure 3.7) of the satellite and the corresponding collision probability can be determined. Thus, given the nature of the avoidance maneuver, a relationship between the separation distance can be established.

Now, the main idea is to ensure satellite safety at time of closest approach, this is possible by specifying a minimum desired value for the miss distance at $t_{ca}$ to be achieved such that the algorithm, by default, determines an optimal trajectory without violating this constraint. If, $D_m$ is the minimum desired miss distance to be achieved then the miss distance constraint can be expressed as,

$$\Delta r_{ca} \geq D_m \tag{3.27}$$

where,

$$\Delta r_{ca} = |\boldsymbol{r_d}(t_{ca}) - \boldsymbol{r_s}(t_{ca})| \tag{3.28}$$

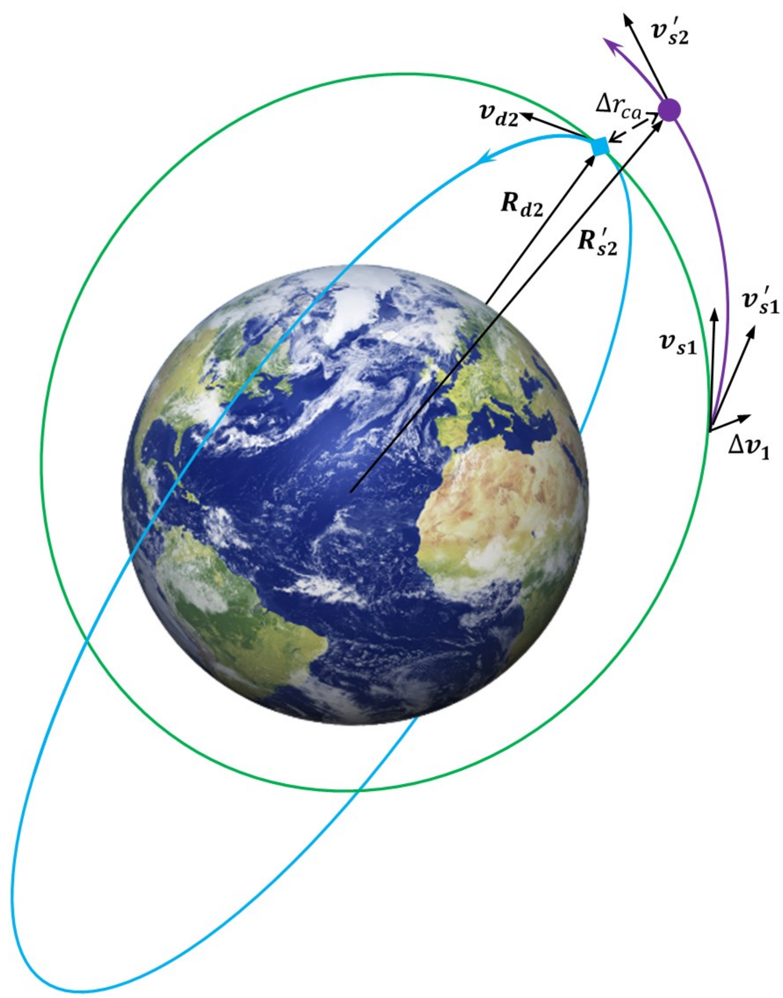


**Fig. 3. 7 Illustration for miss distance**

However, for a more realistic collision avoidance scenario, collision probability [61] is preferred over the miss distance. In addition, the two-dimensional probability density function establishes a correlation with regards to the maneuver direction. So, once the separation distance is determined, the corresponding collision probability is then calculated using the Rician distribution given in the equations (2.16) - (2.18). If, $P_{max}$ is the maximum allowable collision probability then the corresponding collision probability constraint is,

$$P_c < P_{max} \tag{3.29}$$

## 3.6 NUMERICAL SIMULATIONS FOR THREE-IMPULSE APPROACH

The three-impulse collision avoidance maneuver method is tested through various conjunction scenarios using their respective CDM data. In this section, the numerical simulations are presented for one such conjunction pair that was predicted in the past in the LEO regime for which the data was obtained from the reference [62]. Here, the asset object is ESA's meteorological satellite METOP-A and the threatening object is a debris fragment from IRIDIUM 33 collision that occurred in the year of 2009. Table 3.1 provides the orbital information concerning the two objects.

| ***Orbital Elements*** | | ***Satellite*** | ***Debris*** |
|---|---|---|---|
| *Altitude* | *(km)* | 808.531 | 822.869 |
| *Eccentricity* | ~ | $5.016 \times 10^{-4}$ | $8.978 \times 10^{-3}$ |
| *Inclination* | *(degrees)* | 98.778 | 86.315 |
| *RAAN* | *(degrees)* | 123.524 | 16.183 |
| *Perigiee Argument* | *(degrees)* | -86.971 | 162.921 |

**Table 3. 1 Orbital information of the satellite and the debris**

The collision was predicted to occur at 23:58:11.770 UTC on 2 March 2012. The relative miss distance is 207.580 m with a radial, in-track and cross-track separation of 27.12 m, 122.85 m and 165.12 m respectively at TCA, and the relative velocity is found to be 12 km/s.

Figure 3.8 and 3.9 depict the orbital plot and the relative distance plot between the satellite and the debris. It is noteworthy that the simulations are carried out using Numerical propagation under zonal harmonics and third body attraction, yet, accounted only simple cases thus not having any multiple-threatening objects under consideration.

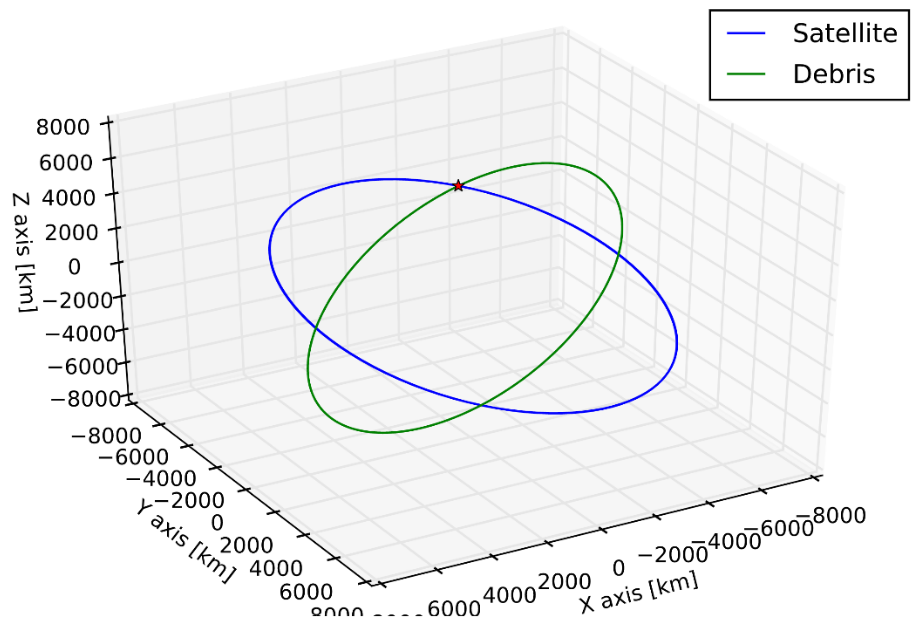


**Fig. 3. 8 3-D orbital plot of the satellite and debris**

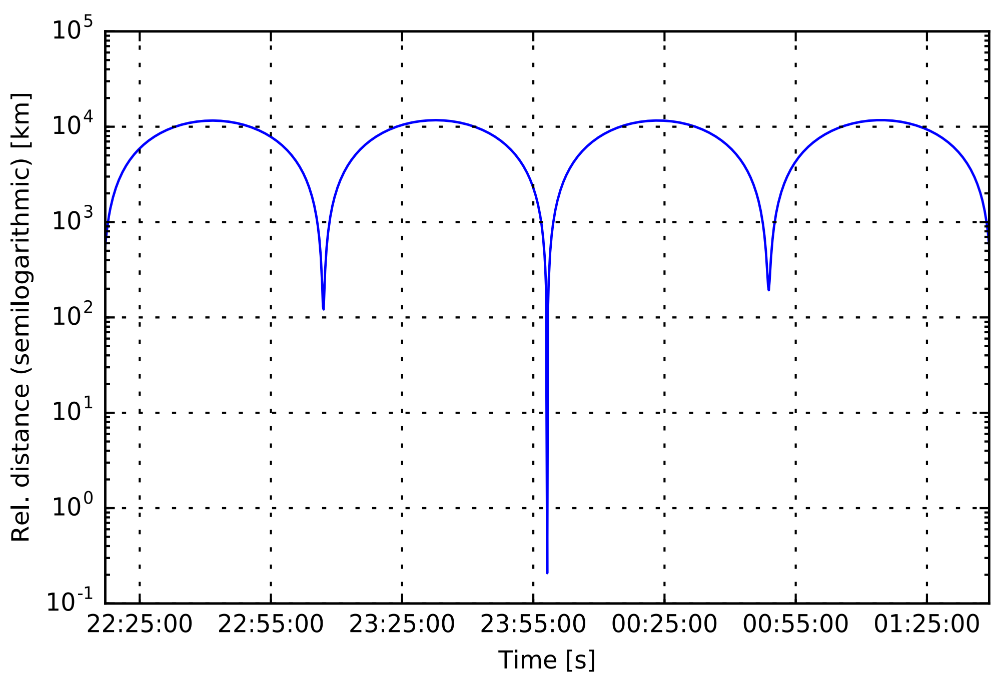


**Fig. 3. 9 Relative distance plot near $t_c$ = 23:58:11.770**

The optimization problem is solved by employing six optimization parameters that enable the satellite operator to consider all possible trajectories that are safe from the approaching debris, within an allowable fuel budget. The optimization parameters are bounded to the ranges specified in table 3.2 that defines the numerical search space. The in-plane and out-of-plane rotation angles for $\Delta \boldsymbol{v_0}$ are specified in radians.

| ***Optimization parameters*** | | $l_b$ | $u_b$ |
|---|---|---|---|
| $\Delta\tau_{am}$ | *(orbits)* | 0 | 1 |
| $\Delta v$ | *(m/s)* | 0 | 1 |
| $\varphi$ | *(radians)* | -π | π |
| $\psi$ | *(radians)* | -π/2 | π/2 |
| $\Delta\tau_{\theta}$ | *(orbits)* | 0 | 1 |
| $\Delta\tau_{f}$ | *(orbits)* | 0 | 1 |

**Table 3. 2 Lower and upper bounds for the optimization parameters**

It is to be noted that the problem is designed with dimensionless (normalized) time units that define the orbital location of the satellite. The orbital location at which the initial avoidance maneuver, $\Delta\tau_{am}$, and the final re-insertion maneuver, $\Delta\tau_{\theta}$, musts be applied is limited to one orbit before and after the time of predicted collision, respectively. The transfer time, $\Delta\tau_{f}$, from the point of new closest approach to the point of re-entry is also confined to one orbit. This is because a short-term transfer is considered during the event of a brief conjunction notification time. The final optimal solutions for $\Delta\tau_{\theta}$ and $\Delta\tau_{f}$ are forecasted to have closer values since the transfer orbits are expected to be adjacent with the satellite's original orbit.

| ***Item*** | ***Value*** |
|---|---|
| *Population size* | 50 |
| *Number of generations* | 600 |
| *Mutation scheme* | best/1/bin |

**Table 3. 3 Properties specific to optimization algorithm**

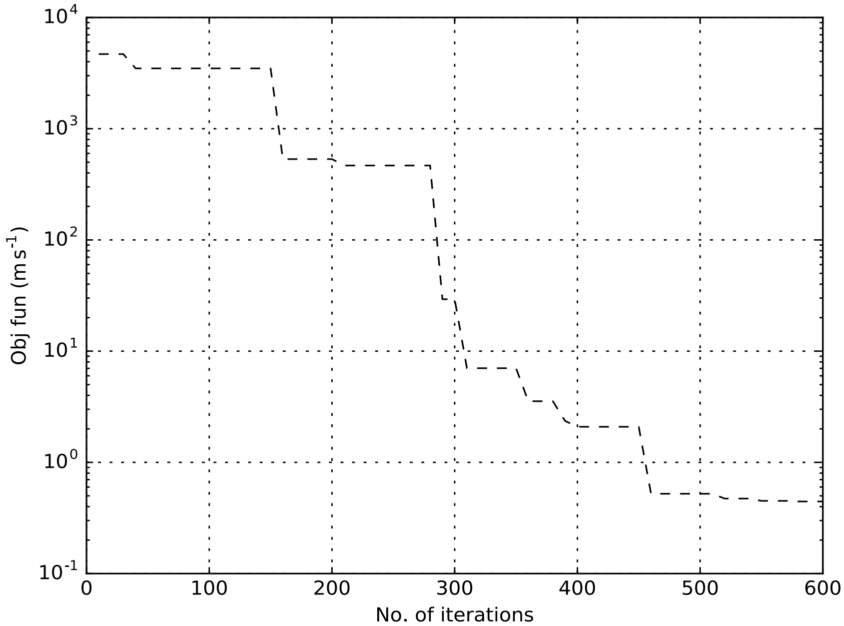


**Fig. 3. 10 Evolution of objective function**

Table 3.3 provides the properties specific to SADE algorithm for the three-impulse method that is enforced so as to determine the globally best solution. The constraint tolerances are specified as $\pm 10^{-3}$ and $\pm 10^{-8}$ for miss distance and collision probability constraint. Among the various mutation schemes available for SADE, the variant best/1/bin is implemented since this particular scheme is found to outperform the other SADE variants as demonstrated in the comparative study performed by Goudos. S.K. et al. [63]. Figure 3.9 illustrates the evolution of the objective function with respect to the number of iterations and points out that the SADE demands only 500 iterations to realize the globally minimum solution while the rest are for refinement.

Two sets of numerical simulations are performed, the first set is for validating the three impulse method by varying the constraints (minimum allowable miss distance and maximum threshold for collision probability) and in the second set of simulations, a comparative study is carried out between distinct initial avoidance maneuver profiles. The characteristics of the different test cases are clearly listed in the table 3.4. The bounds for the constraints are arbitrarily chosen to test the capabilities of the proposed method.

| *Test cases* | *Constraint profiles* | *Initial avoidance maneuver profiles* |
|---|---|---|
| *Case 1a* | $D_m = \mathbf{1.0km}$, $P_{max} = \mathbf{10^{-5}}$ | RTN |
| *Case 1b* | $D_m = \mathbf{1.5km}$, $P_{max} = 10^{-5}$ | RTN |
| *Case 1c* | $D_m = \mathbf{2.0km}$, $P_{max} = 10^{-5}$ | RTN |
| *Case 1a* | $D_m = 1.0km$, $P_{max} = \mathbf{10^{-6}}$ | RTN |
| *Case 1a* | $D_m = 1.0km$, $P_{max} = \mathbf{10^{-7}}$ | RTN |
| *Case 2a* | $D_m = 2.0km$, $P_{max} = 10^{-5}$ | **RT** |
| *Case 2b* | $D_m = 2.0km$, $P_{max} = 10^{-5}$ | **T** |

**Table 3. 4 Characteristics of the test cases**

### 3.6.1 RESULTS FOR DIFFERENT CONSTRAINT PROFILES

In order to assess the effect that the constraints have on the overall fuel consumption, simulations (cases 1a, 1b, 1c, 1d and 1e) are performed for different values of constraints considering the avoidance maneuver is applied on both in-plane (radial and in-track) and out-of-plane (cross-track) directions. Figures 3.10 – 3.14 show the evolution of variation in the X, Y and Z components of the position of the satellite in the ECI system over time after applying the respective initial avoidance maneuver corresponding to each test case. It points out that the change in X, Y and Z are not consistent throughout as it varies after the closet approach $t_{ca}$ since the satellite enters the second transfer orbit during that instant.

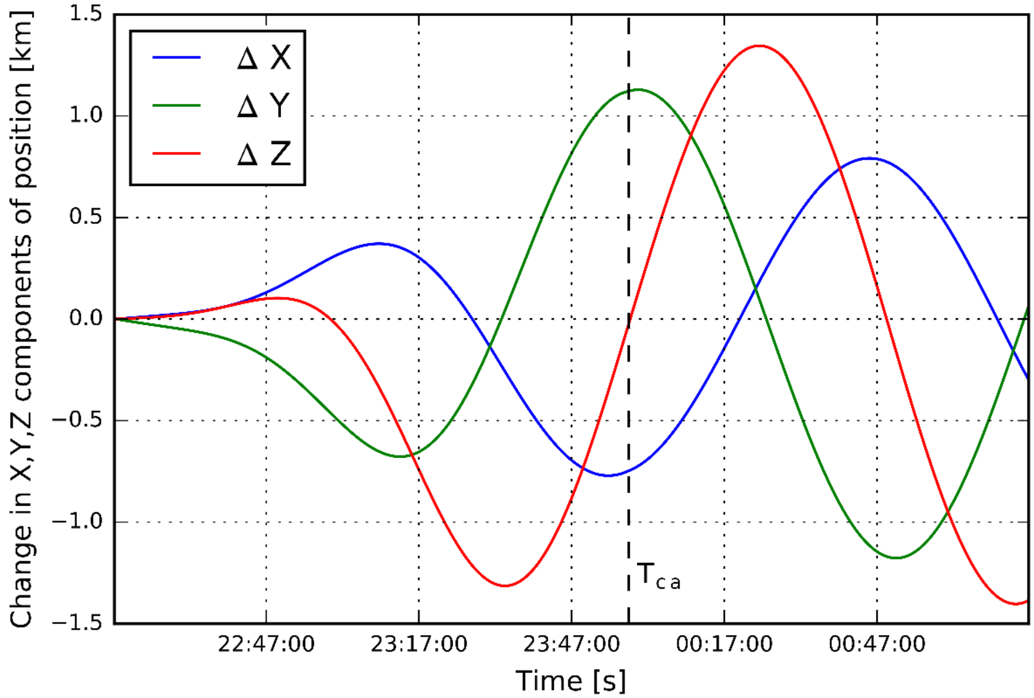


**Fig. 3. 11 Change in X, Y, Z position components of the satellite after applying initial avoidance maneuver for test case 1a: $\Delta v_0$ = 0.0765 *m/s*, new $t_{ca}$ = 23:58:11.861**

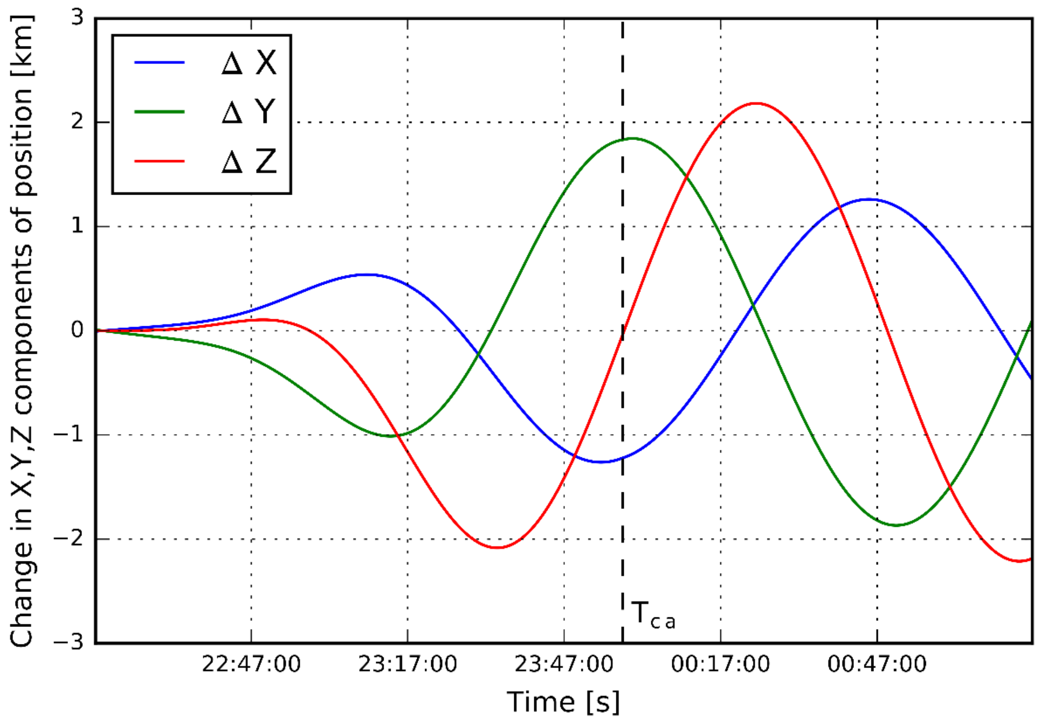


**Fig. 3. 12 Change in X, Y, Z position components of the satellite after applying initial avoidance maneuver for test case 1b: $\Delta v_0$ = 0.1210 m/s, new $t_{ca}$ = 23:58:11.918**

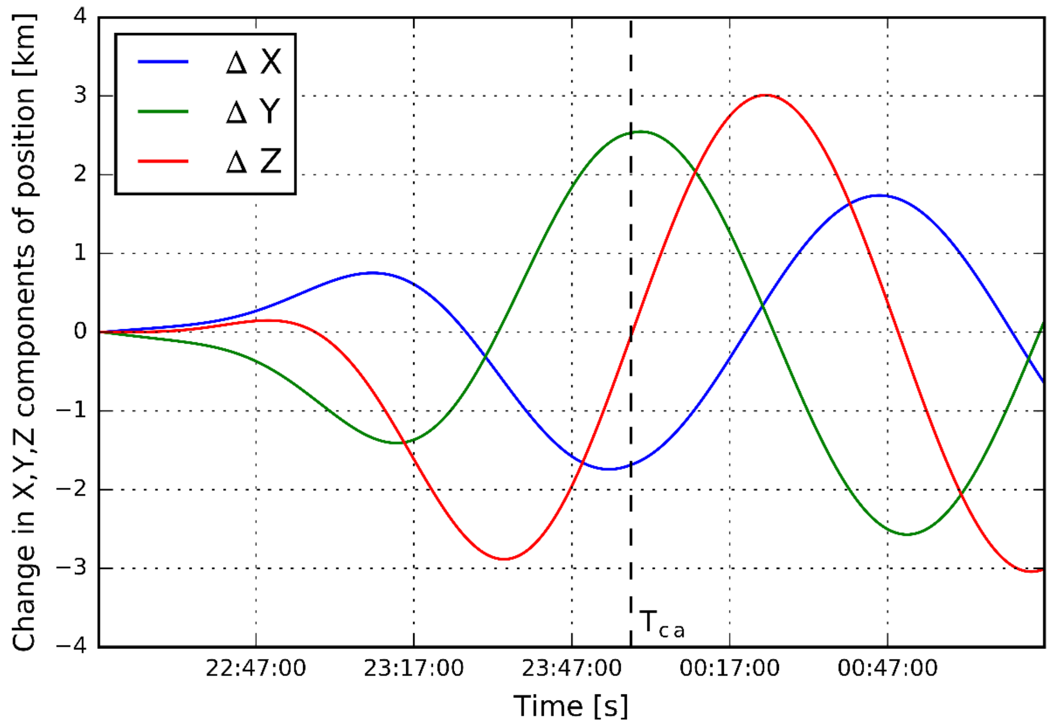


**Fig. 3. 13 Change in X, Y, Z position components of the satellite after applying initial avoidance maneuver for test case 1c: $\Delta v_0$ = 0.1669 m/s, new $t_{ca}$ = 23:58:11.974**

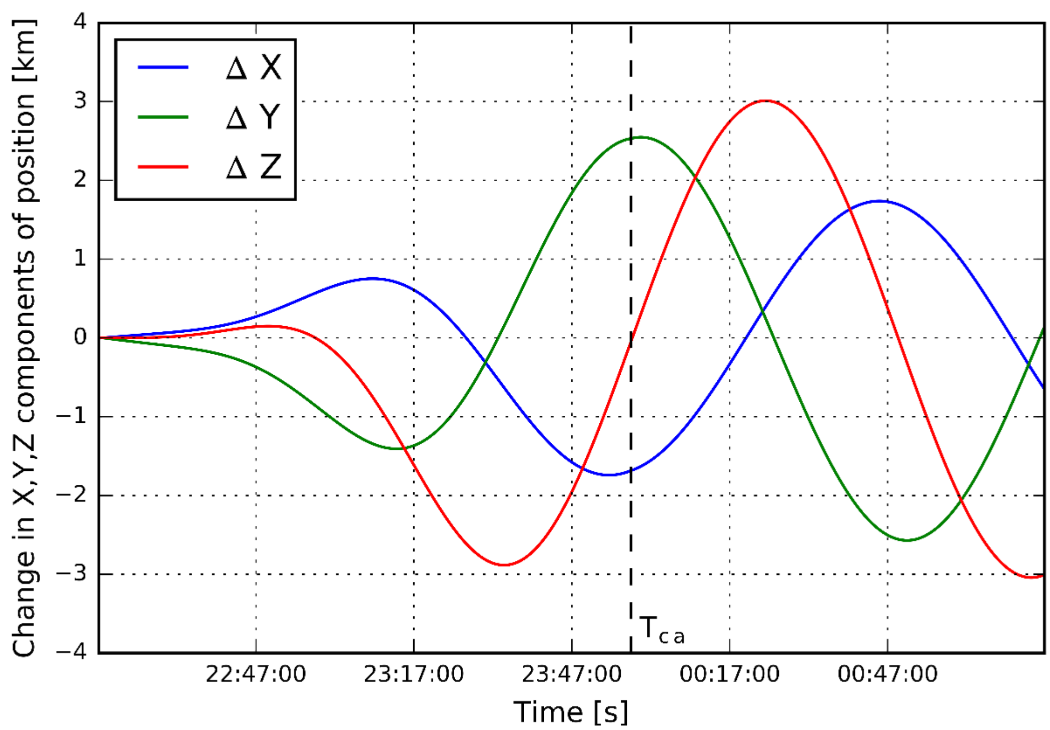


**Fig. 3. 14 Change in X, Y, Z position components of the satellite after applying initial avoidance maneuver for test case 1d: $\Delta v_0$ = 0.1123 m/s, new $t_{ca}$ = 23:58:11.904**

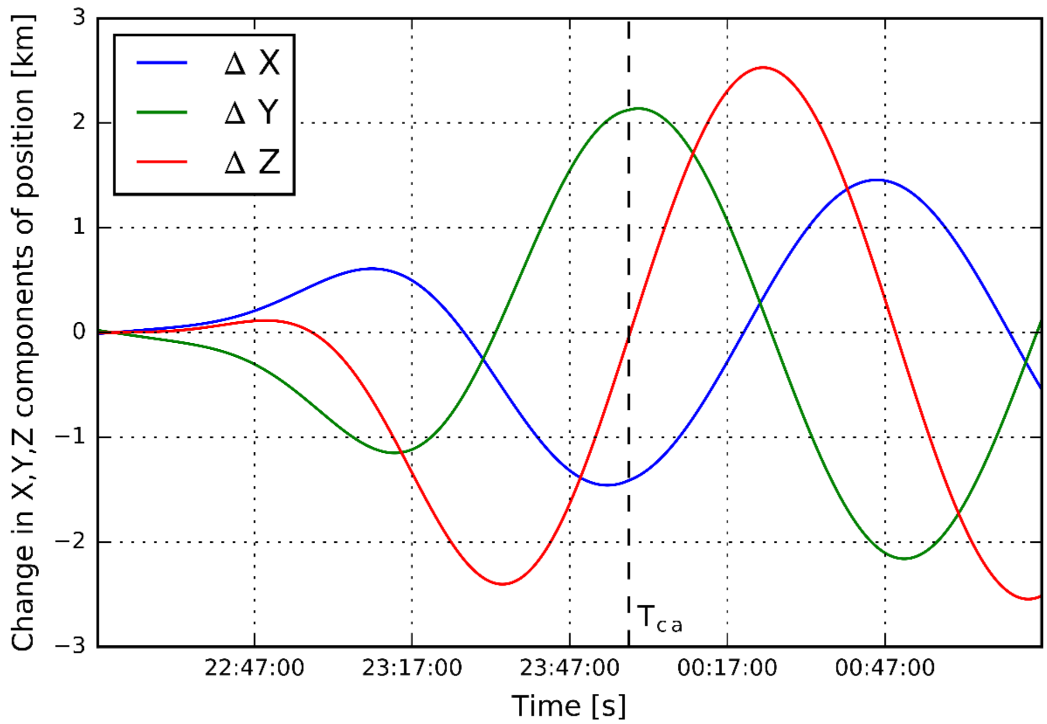


**Fig. 3. 15 Change in X, Y, Z position components of the satellite after applying initial avoidance maneuver for test case 1e: $\Delta v_0$ = 0.1425 m/s, new $t_{ca}$ = 23:58:11.941**

The simulation results are summarized in the Tables 3.5, 3.6 and 3.7. All the solutions secured the desired threshold values specified in the constraints. One distinguishing characteristic found from the results (Table 3.5 and 3.6) is that the algorithm converges to procure most of the separation distance in the in-track direction, by doing so, it greatly lowers the collision probability [10]. Table 3.5 compares the results for varying minimum $D_m$ to be achieved and Table 3.6 compares the results for varying maximum allowable $P_{max}$. It can be observed that when the constraint requirements are increased, the impulse $\Delta v_0$ required to achieve them also increases. To reach a relative distance of 1 $km$ and collision probability of $10^{-5}$ during the closest approach a burn of at least 0.0765 $m/s$ is required which increased nearly to 155% when $D_m$ is increased to 1.5 $km$ (0.1210 $m/s$) or when $P_{max}$ lowered to $10^{-6}$ (0.1123 $m/s$).

| Maneuver characteristics | | Case 1a | Case 1b | Case 1c |
|---|---|---|---|---|
| $\boldsymbol{t_0}$ | *(UTC)* | 2012-03-02 22:17:23.946 | 2012-03-02 22:18:34.149 | 2012-03-02 22:17:51.352 |
| $\Delta \boldsymbol{v_0}$ | *(m/s)* | 0.0765 | 0.1210 | 0.1669 |
| $\boldsymbol{t_1}$ *or* $\boldsymbol{t_{ca}}$ | *(UTC)* | 2012-03-02 23:58:11.861 | 2012-03-02 23:58:11.918 | 2012-03-02 23:58:11.974 |
| $\Delta \boldsymbol{v_1}$ | *(m/s)* | 0.0719 | 0.1196 | 0.1653 |
| $\boldsymbol{t_2}$ | *(UTC)* | 2012-03-03 01:16:47.440 | 2012-03-03 01:22:52.323 | 2012-03-03 01:30:27.516 |
| $\Delta \boldsymbol{v_2}$ | *(m/s)* | 0.0068 | 0.0026 | 0.0022 |
| *Maneuver cycle* | *(mins.)* | 179.391 | 184.302 | 192.602 |
| *Total* $\Delta \boldsymbol{v}$ *consumption* | *(m/s)* | 0.1553 | 0.2433 | 0.3345 |

**Table 3. 5 Simulation results for different miss distance constraint cases**

| Maneuver characteristics | | Case 1a | Case 1d | Case 1e |
|---|---|---|---|---|
| $\boldsymbol{t_0}$ | *(UTC)* | 2012-03-02 22:17:23.946 | 2012-03-02 22:17:43.355 | 2012-03-02 22:20:03.412 |
| $\Delta \boldsymbol{v_0}$ | *(m/s)* | 0.0765 | 0.1123 | 0.1425 |
| $\boldsymbol{t_1}$ *or* $\boldsymbol{t_{ca}}$ | *(UTC)* | 2012-03-02 23:58:11.861 | 2012-03-02 23:58:11.904 | 2012-03-02 23:58:11.941 |
| $\Delta \boldsymbol{v_1}$ | *(m/s)* | 0.0719 | 0.1653 | 0.1408 |
| $\boldsymbol{t_2}$ | *(UTC)* | 2012-03-03 01:16:47.440 | 2012-03-03 01:22:52.323 | 2012-03-03 01:22:51.444 |
| $\Delta \boldsymbol{v_2}$ | *(m/s)* | 0.0068 | 0.0014 | 0.0050 |
| *Maneuver cycle* | *(mins.)* | 179.391 | 178.208 | 163.230 |
| *Total* $\Delta \boldsymbol{v}$ *consumption* | *(m/s)* | 0.1553 | 0.2242 | 0.2884 |

**Table 3. 6 Simulation results for different collision probability constraint cases**

| *Cases* | *Radial Separation (m)* | *In-Track Separation (m)* | *Cross-Track Separation (m)* | *Miss Distance $\Delta r_{ca}$ (m)* | *Collision Probability $P_c$* |
|---|---|---|---|---|---|
| *Case 1a* | -427.171 | 825.576 | -373.073 | 1001.615 | $9.488 \times 10^{-6}$ |
| *Case 1b* | -655.597 | 1234.779 | -560.671 | 1506.267 | $3.754 \times 10^{-7}$ |
| *Case 1c* | -673.924 | -1862.246 | 282.008 | 2000.416 | $4.508 \times 10^{-9}$ |
| *Case 1d* | -600.590 | 1137.641 | -515.984 | 1386.065 | $9.115 \times 10^{-7}$ |
| *Case 1e* | -748.514 | 1402.989 | -637.625 | 1713.248 | $6.853 \times 10^{-8}$ |

**Table 3. 7 Radial, In-track and Cross-track separation distance for distinct constraint cases**

Moreover, when the miss distance is varied as illustrated in Table 3.5, it appears that the resulting collision probabilities thus calculated using equation (2.15) are well below $10^{-5}$ margin. Likewise, from the results of distinct collision probability cases (Table 3.6), the resulting separation distances are certainly higher. This shows that the algorithm is forced to find the optimal solutions primarily based on either of the two factors $\Delta r_{ca}$ or $P_c$ whichever is most significant; as a result, although not violating the constraints, a considerable amount of $\Delta v$ is wasted in securing both constraints. It is evident that the wastage of $\Delta v$ is due to the significant change in orbital parameters, particularly, semi-major axis and eccentricity, between the original, first transfer and second transfer orbit (Figures 3.15 – 3.19). Nevertheless, if the bounds for the constraints are carefully chosen by the operator then this wastage of $\Delta v$ can be avoided.

Now, considering the total-$\Delta v$ accounted to complete the overall rendezvous process, the case 1a involving the least with $\Delta v_{tot} = 0.1553\ m/s$ can be chosen as the best solution for the collision scenario under study. However, the results reveal a longer maneuver cycle period (i.e., the duration the satellite spends away from its original orbit). For instance, in case 1a, the satellite takes $179.4\ mins$ to complete the transfer and this means that the satellite is delayed by that amount from its normal operation time. It is evident that for most satellite missions even a slightest change in the orbit may significantly affect the ability of the satellite to perform its required mission specifications. If there arises a situation with a tighter transfer period, then the case 1e with the maneuver cycle of $163.23\ mins$ can be considered as a satisfactory solution.

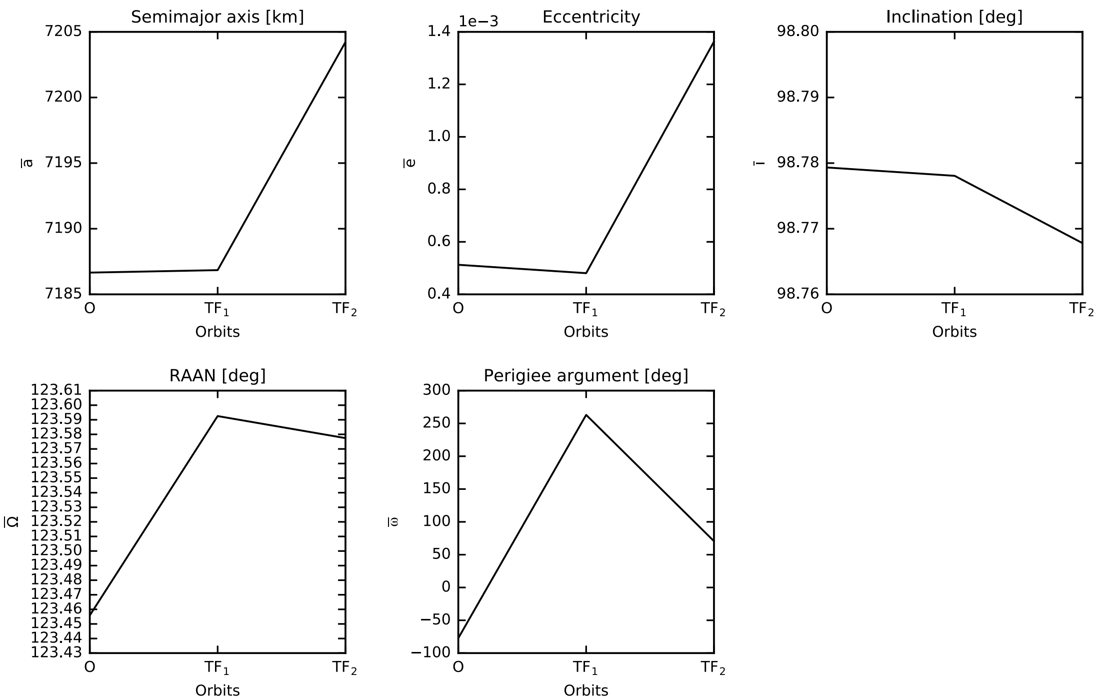


**Fig. 3. 16 Change in mean orbital parameters for test case 1a**

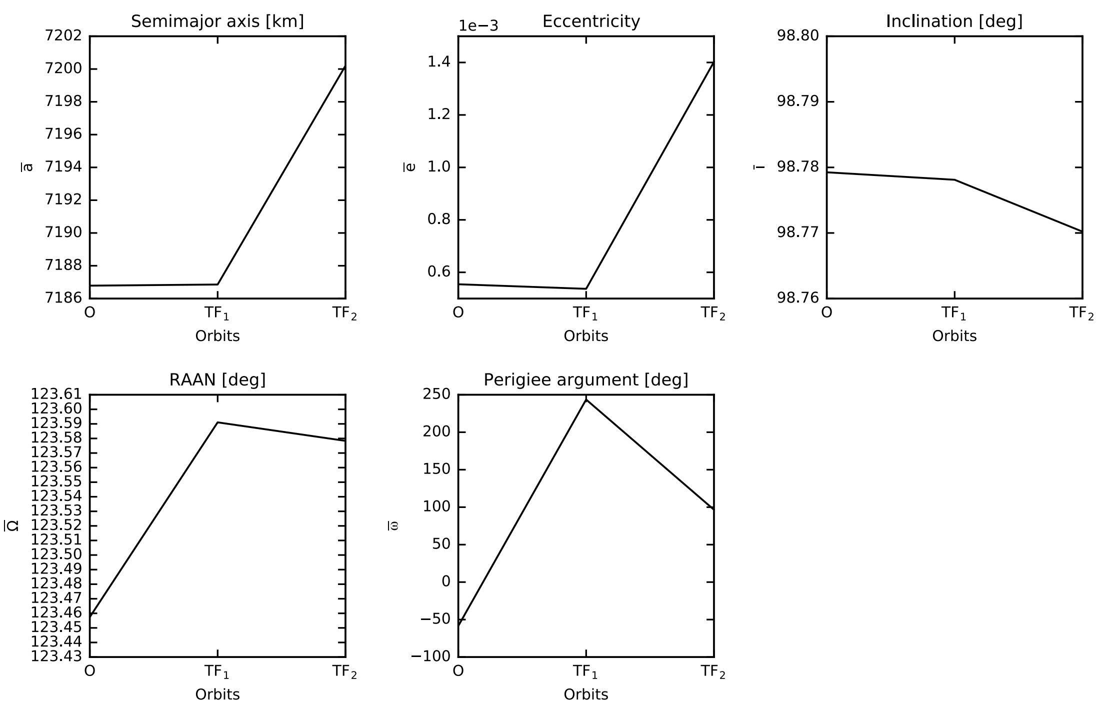


**Fig. 3. 17 Change in mean orbital parameters for test case 1b**

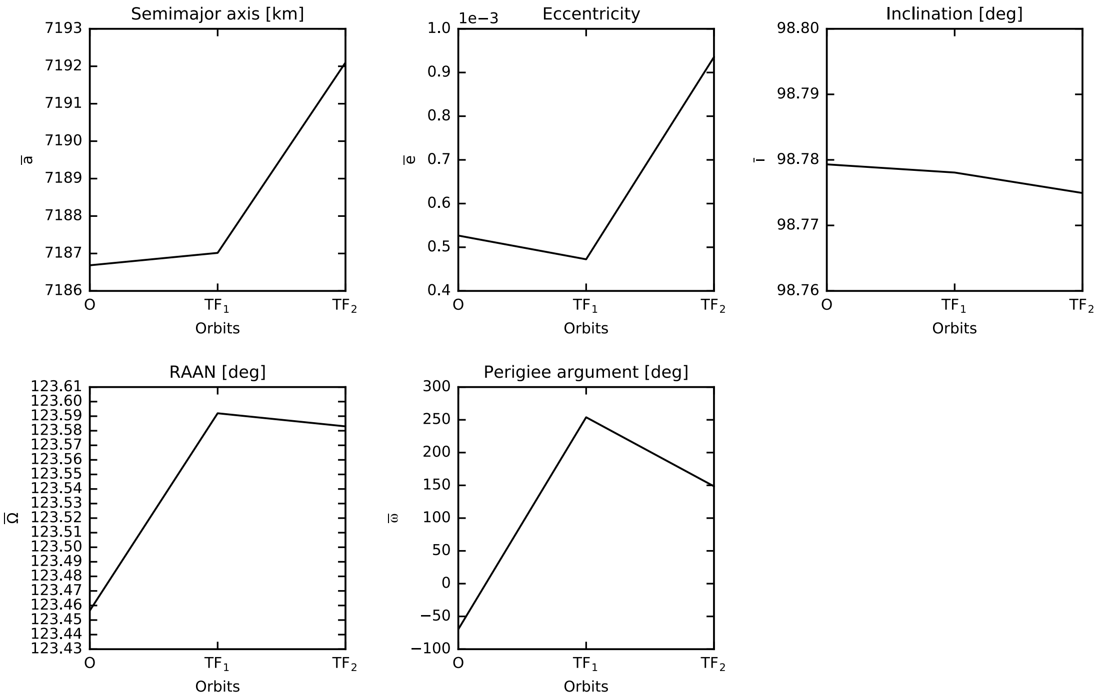


**Fig. 3. 18 Change in mean orbital parameters for test case 1c**

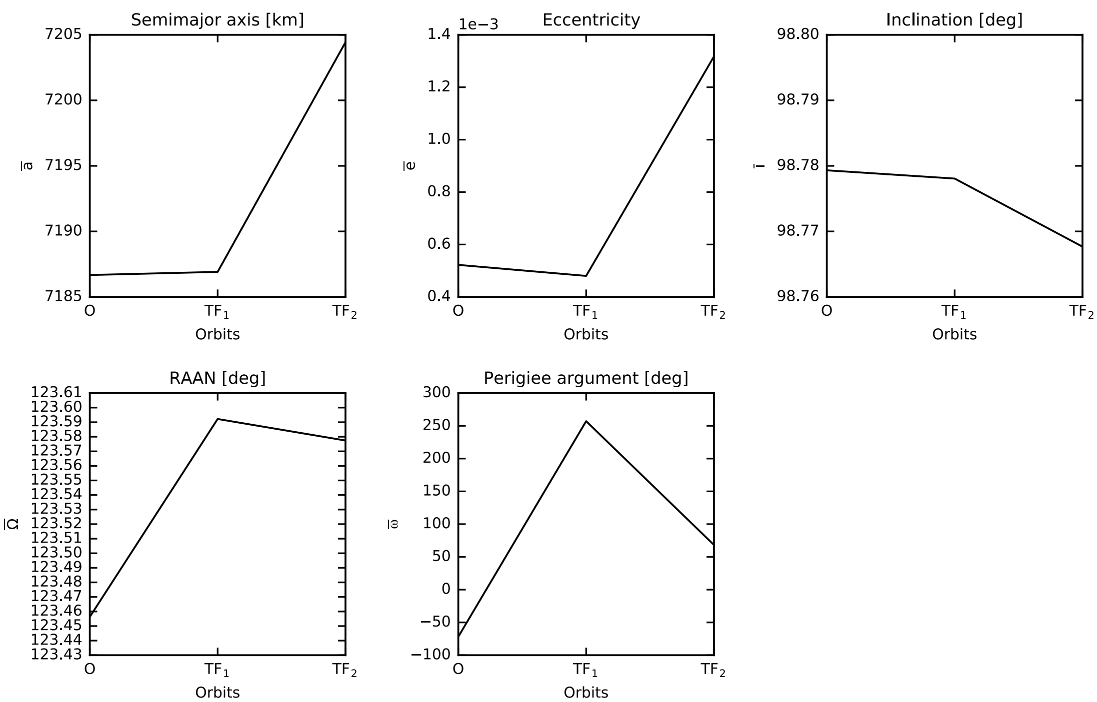


**Fig. 3. 19 Change in mean orbital parameters for test case 1d**

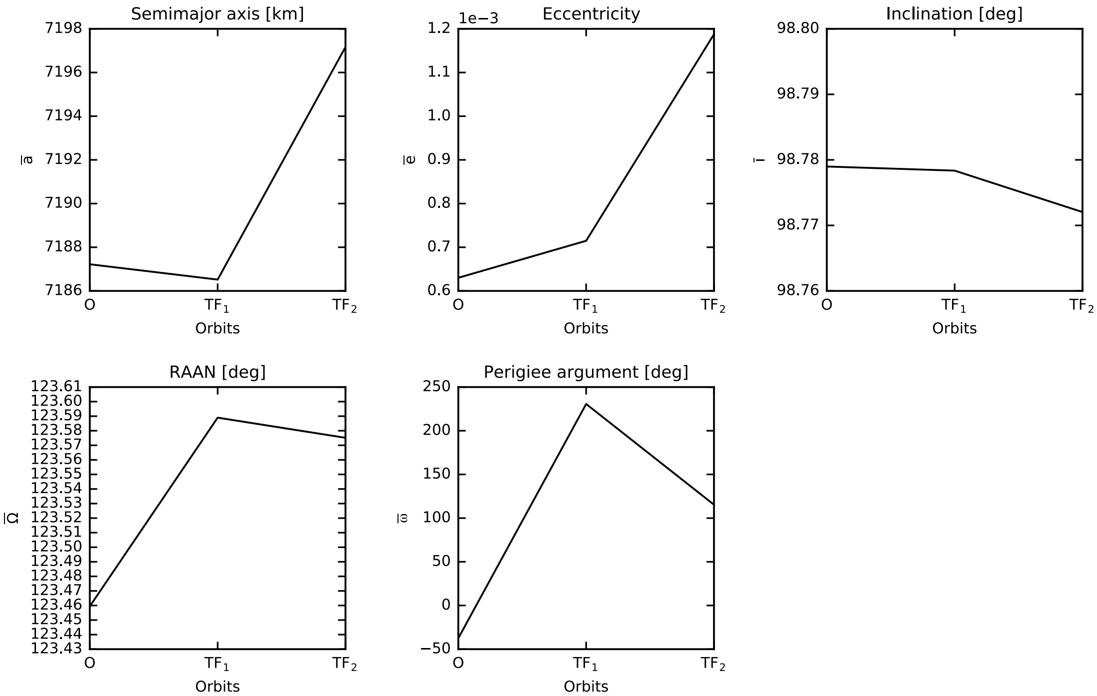


**Fig. 3. 20 Change in mean orbital parameters for test case 1e**

Overall, it is a trade-off between the transfer duration (maneuver cycle) and the total fuel expenditure. Considering these aspects, the solutions can be further improvised by adding more constraints specific to transfer time and mission-related specifications.

### 3.6.2 RESULTS FOR DIFFERENT AVOIDANCE MANEUVER PROFILES

The next set of simulations are performed to analyze how the algorithm behaves when the direction for the initial avoidance maneuver, $\Delta\boldsymbol{v_0}$, is regulated for which an analysis is conducted by considering avoidance maneuver in: all three directions (case 1c), only in-plane direction, i.e., radial and in-track (case 2a), and only in-track direction (case 2b). Table 3.8 reports the results for the distinct maneuver profiles.

The results show that irrespective of the direction of the initial avoidance maneuver, the resulting $\Delta\boldsymbol{v_1}$ and $\Delta\boldsymbol{v_2}$ calculated from equations (3.25) and (3.26) are applied in all three directions. The algorithm, however, obtained the solutions correspondingly without violating the constraints. Moreover, when the direction of the initial avoidance maneuver is considered only in the in-plane (Radial and Transverse) direction $\Delta v_{tot}$ increased by 19%

while when considered only in in-track (Transverse) direction $\Delta v_{tot}$ increased by 33%. This shows that there is no improvement in limiting the direction of the initial avoidance maneuver towards obtaining minimum-fuel solution.

| *Test cases* | | $\Delta v_R$ *(m/s)* | $\Delta v_T$ *(m/s)* | $\Delta v_N$ *(m/s)* | $\Delta v$ *(m/s)* | $\Delta v_{tot}$ *(m/s)* |
|---|---|---|---|---|---|---|
| | $\Delta v_0$ | -0.0644 | 0.1229 | 0.0926 | 0.1669 | |
| *Case 1c* | $\Delta v_1$ | 0.0746 | -0.1202 | -0.0855 | 0.1653 | 0.3345 |
| | $\Delta v_2$ | 0.0008 | -0.0021 | 0.0002 | 0.0022 | |
| | $\Delta v_0$ | -0.0804 | 0.1809 | 0.0 | 0.1982 | |
| *Case 2a* | $\Delta v_1$ | 0.0821 | -0.1782 | -0.0021 | 0.1962 | 0.3972 |
| | $\Delta v_2$ | 0.0014 | -0.0026 | 0.0004 | 0.0029 | |
| | $\Delta v_0$ | 0.0 | 0.2215 | 0.0 | 0.2215 | |
| *Case 2b* | $\Delta v_1$ | 0.0054 | -0.2108 | -0.0046 | 0.2110 | 0.4450 |
| | $\Delta v_2$ | 0.0048 | -0.0101 | 0.0053 | 0.0124 | |

**Table 3. 8 Results for different avoidance maneuver profiles**

Interestingly, it can be observed that the amount of $\Delta v_0$ consumed for collision avoidance is proportional to that consumed for re-insertion ($\Delta v_1$+ $\Delta v_2$) for all cases. This implies that the amount of fuel required for de-orbiting and re-orbiting the satellite are approximately equal ($\Delta v_0 \approx \Delta v_1$+ $\Delta v_2$), yet, with a very small variation accounting to compensate for the drift due to perturbation effects.

Further, the transfer orbits thus obtained are in close proximity with respect to the satellite's original orbit while the satellite is still in the safe vicinity during the time of closest approach $t_{ca}$. These aspects validate that the control scheme used for the three-impulse method is performing well as desired. Figures 3.21 and 3.22 portrays the variation of the mean orbital elements corresponding to case 2a and 2b. Majority of the deviations between the orbits are induced due to the variations in the semimajor axis, eccentricity and the perigee argument, meanwhile there is a significant drift in the right ascension of the ascending node.

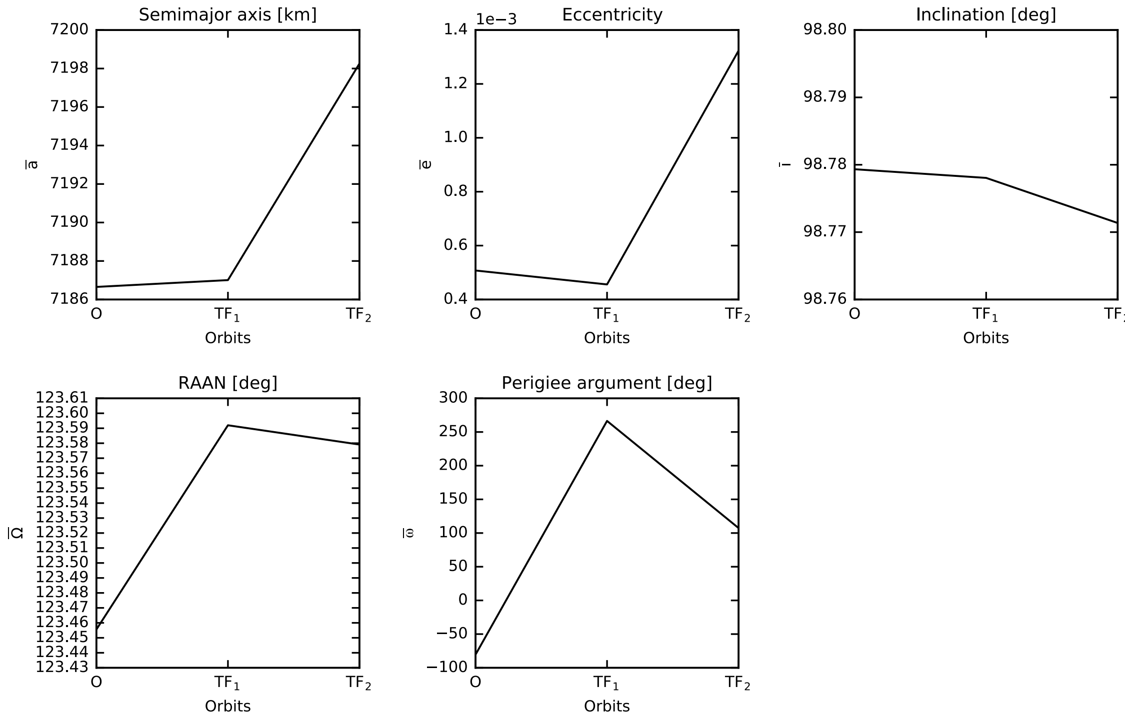


**Fig. 3. 21 Change in mean orbital parameters for test case 2a**

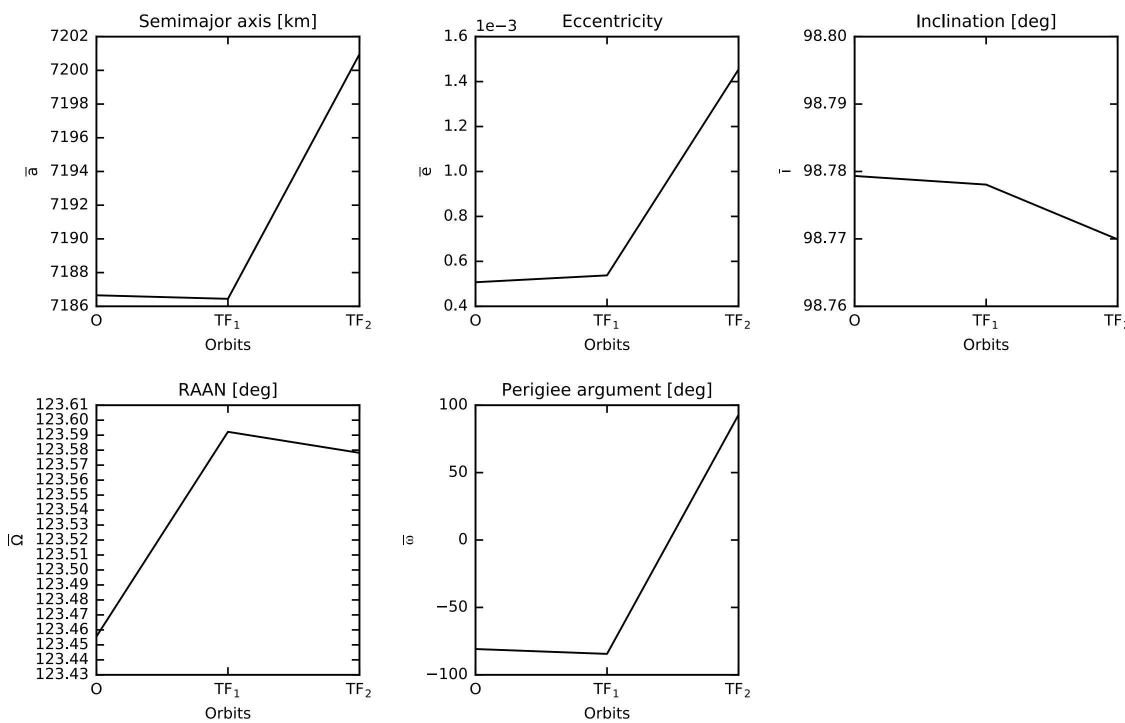


**Fig. 3. 22 Change in mean orbital parameters for test case 2b**

# TWO-IMPULSE MANEUVER OPTIMIZATION

## 4.1 OVERVIEW

The fundamental collision avoidance maneuver problem using a two-impulse maneuver approach can be formulated in a quite simple manner. Here, the first impulse corresponds to collision avoidance while the second represents the orbital re-insertion. The main idea is to determine a transfer trajectory that lies closet to the nominal orbit thereby, ensuring safe pass of the satellite during the time of closest approach. This trajectory optimization problem is modeled as minimization problem aimed at minimizing the $\Delta v$ consumption and is characterized by the presence of constraints required to control the execution time of the orbital maneuvers while satisfying the mission objective.

## 4.2 PROBLEM DEFINITION

Unlike the previous approach, the problem involves calculating the optimal trajectory by using merely two impulse maneuvers: the first is to avoid collision and the second for orbital re-insertion. This allows transferring of the satellite from the departure point to arrival point through a single transfer orbit. In general, the orbital rendezvous operations can involve coplanar orbital transfer between two coaxial elliptical orbits in which the transfer trajectory shares a common apse line [64]. However, this is not susceptible practically since the orbits are not completely planar due to perturbation effects. Therefore, this orbital transfer problem cannot be treated as a coplanar transfer problem rather regarded as non-coplanar transfer between two elliptic orbits. Clearly, the objective function for the two-impulse method is reduced to:

$$J = \Delta v_1 + \Delta v_2 = |\Delta \boldsymbol{v_1}| + |\Delta \boldsymbol{v_2}| \tag{4.1}$$

where, $\Delta v_1$ is the avoidance maneuver and $\Delta v_2$ is the re-entry maneuver, computed by calculating the magnitude of change in velocities at the departure and re-insertion/arrival point. The trajectory optimization involves minimizing the above equation using Self-Adaptive Differential Evolution while conforming with the constraints. The next section provides analytical expressions that approximate the mathematical entities involved in solving this trajectory optimization problem.

## 4.3 ANALYTICAL REPRESENTATION

Let $\theta_1$ and $\theta_2$ be the true anomalies that define the orbital locations at which the avoidance maneuver and re-entry maneuver must be applied. The position and velocity vectors immediately before the first impulse and after the second impulse in the nominal orbital frame can be written as:

$$\boldsymbol{r_1} = \boldsymbol{r}(\theta_1) = \frac{a(1-e^2)}{1+e\,cos(\theta_1)}\left[cos(\theta_1)\,\widehat{\boldsymbol{R}}_{\boldsymbol{1}} + sin(\theta_1)\ \widehat{\boldsymbol{T}}_{\boldsymbol{1}}\right] \tag{4.2}$$

$$\boldsymbol{v_1} = \boldsymbol{v}(\theta_1) = \sqrt{\frac{\mu}{a(1-e^2)}}\left[e\,sin(\theta_1)\,\widehat{\boldsymbol{R}}_{\boldsymbol{1}} + (1+e\,cos(\theta_1))\,\widehat{\boldsymbol{T}}_{\boldsymbol{1}}\right] \tag{4.3}$$

$$\boldsymbol{r_2} = \boldsymbol{r}(\theta_2) = \frac{a(1-e^2)}{1+e\,cos(\theta_2)}\left[cos(\theta_2)\,\widehat{\boldsymbol{R}}_{\boldsymbol{2}} + sin(\theta_1)\ \widehat{\boldsymbol{T}}_{\boldsymbol{2}}\right] \tag{4.4}$$

$$\boldsymbol{v_2} = \boldsymbol{v}(\theta_2) = \sqrt{\frac{\mu}{a(1-e^2)}}\left[e\sin(\theta_2)\,\widehat{\boldsymbol{R}}_{\boldsymbol{2}} + (1+e\cos(\theta_2))\,\widehat{\boldsymbol{T}}_{\boldsymbol{2}}\right] \tag{4.5}$$

However, in this study, the orbital locations are referenced with respect to time, i.e., $t_1$ instead of $\theta_1$ and $t_2$ instead of $\theta_2$. Thus, the equations (4.2 to 4.5) can be rewritten as functions of time:

$$\boldsymbol{r_1} = \boldsymbol{r}(t_1) = r_{1r}(t_1)\widehat{\boldsymbol{R}}_{\boldsymbol{1}} + r_{1t}(t_1)\widehat{\boldsymbol{T}}_{\boldsymbol{1}} \tag{4.6}$$

$$\boldsymbol{v_1} = \boldsymbol{v}(t_1) = v_{1r}(t_1)\widehat{\boldsymbol{R}}_{\boldsymbol{1}} + v_{1t}(t_1)\widehat{\boldsymbol{T}}_{\boldsymbol{1}} \tag{4.7}$$

$$\boldsymbol{r_2} = \boldsymbol{r}(t_2) = r_{2r}(t_2)\widehat{\boldsymbol{R}}_{\boldsymbol{2}} + r_{2t}(t_2)\widehat{\boldsymbol{T}}_{\boldsymbol{2}} \tag{4.8}$$

$$\boldsymbol{v_2} = \boldsymbol{v}(t_2) = v_{2r}(t_2)\widehat{\boldsymbol{R}}_{\boldsymbol{2}} + v_{2t}(t_2)\widehat{\boldsymbol{T}}_{\boldsymbol{2}} \tag{4.9}$$

Now, the change in velocity required to move the satellite from the nominal orbit to the transfer orbit is calculated by:

$$\Delta \boldsymbol{v_1} = \boldsymbol{v_1}' - \boldsymbol{v_1} \tag{4.10}$$

and likewise, the change in velocity required for re-entry is:

$$\Delta \boldsymbol{v_2} = \boldsymbol{v_2} - \boldsymbol{v_2}' \tag{4.11}$$

Here, $\boldsymbol{v_1}'$ and $\boldsymbol{v_2}'$ are the velocities of the satellite calculated in the transfer orbit at time $t_1$ and $t_2$, respectively. As mentioned earlier, the transfer orbit that facilitates the safe travel of the satellite between the departure and arrival point is obtained by solving the Lambert's problem. The equations for these velocities can be obtained as:

$$\boldsymbol{v_1}' = \boldsymbol{v}'(t_1) = v_{1r}'(t_1)\widehat{\boldsymbol{R}}_{\boldsymbol{1}} + v_{1t}'(t_1)\widehat{\boldsymbol{T}}'_{\boldsymbol{1}} \tag{4.12}$$

$$\boldsymbol{v_2}' = \boldsymbol{v}'(t_2) = v_{2r}'(t_2)\widehat{\boldsymbol{R}}_{\boldsymbol{2}} + v_{2t}'(t_2)\widehat{\boldsymbol{T}}'_{\boldsymbol{2}} \tag{4.13}$$

$\widehat{\boldsymbol{T}}'_{\boldsymbol{1}}$ represents transverse direction of $\boldsymbol{r_1}$ and $\widehat{\boldsymbol{T}}'_{\boldsymbol{2}}$ represent transverse direction of $\boldsymbol{r_2}$ in the transfer orbital plane. Substituting the equations (4.7), (4.9), (4.12) and (4.13) into (4.10) and (4.11):

$$\Delta \boldsymbol{v_1} = \left(v_{1r}'(t_1) - v_{1r}(t_1)\right)\widehat{\boldsymbol{R}}_{\boldsymbol{1}} + v_{1t}'(t_1)\widehat{\boldsymbol{T}}'_{\boldsymbol{1}} - v_{1t}(t_1)\widehat{\boldsymbol{T}}_{\boldsymbol{1}} \tag{4.14}$$

$$\Delta \boldsymbol{v_2} = \left(v_{2r}(t_2) - v_{2r}'(t_2)\right)\widehat{\boldsymbol{R}}_{\boldsymbol{2}} + v_{2t}(t_2)\widehat{\boldsymbol{T}}_{\boldsymbol{2}} - v_{2t}'(t_2)\widehat{\boldsymbol{T}}'_{\boldsymbol{2}} \tag{4.15}$$

For uniformity, the components of position and velocity can be expressed in the inertial reference frame $\langle \widehat{\boldsymbol{X}}, \widehat{\boldsymbol{Y}}, \widehat{\boldsymbol{Z}} \rangle$ through the relationship matrix described in section {}. Thus, the equations 4.14 and 4.15 becomes:

$$\Delta \boldsymbol{v_1} = \Delta v_{1x}\widehat{\boldsymbol{X}} + \Delta v_{1y}\widehat{\boldsymbol{Y}} + \Delta v_{1z}\widehat{\boldsymbol{Z}} \tag{4.16}$$

$$\Delta \boldsymbol{v_2} = \Delta v_{2x}\widehat{\boldsymbol{X}} + \Delta v_{2y}\widehat{\boldsymbol{Y}} + \Delta v_{2z}\widehat{\boldsymbol{Z}} \tag{4.17}$$

Evidently, the components of both characteristic change in velocity equations are of functions of three independent variables that can be defined by: a) the initial state of the satellite in the nominal orbit, $t_1$ , b) the final state of the satellite in the nominal orbit, $t_2$ and c) the time of flight of the satellite between the initial and final position (defined by $t_1$ and

$t_2$ in the nominal orbit, respectively) in the transfer orbit, $t_f$. The following equations define the time instants $t_1$, $t_2$, and $t_f$:

$$t_1 = t_c - (\Delta\tau_1 * T_s) \tag{4.18}$$

$$t_2 = t_c + (\Delta\tau_2 * T_s) \tag{4.19}$$

$$t_f = t_1 + (\Delta\tau_f * T_s) \tag{4.20}$$

From the above equations, the independent variables that designate the decision parameters for the two-impulse collision avoidance optimization problem are nothing but the dimensionless times $\Delta\tau_1$, $\Delta\tau_2$ and $\Delta\tau_f$.

## 4.4 ALGORITHM DESCRIPTION

As mentioned earlier, the two-impulse collision avoidance maneuver optimization approach discussed in this chapter is a numerical optimization problem that aims at minimizing the total fuel cost that is accounted in terms of total-$\Delta v$ involved. The objective is to ensure that the satellite maintains a safe separation distance with regards to the approaching object during the time of closest approach. For this purpose, two-impulse approach is modeled such that the satellite operator can plan for a collision avoidance maneuver by specifying just the maneuver execution time desired miss distance and the collision probability threshold which are modelled in as constraints. Additional mission constraints, based on CONOPS (CONcept Of Operations), can be designed if required. The following flowchart illustrates a basic workflow involved in the two-impulse approach.

Firstly, the initial states of the satellite and the debris at the time of predicted collision are extracted from the Conjunction Data Message along with the information about error covariance. The numerical propagator is then set up using the initial states and the force model. Once the propagator is established the algorithm initiates by generating its initial population using which the initial state of the satellite is propagated backward to $t_1$ and forward to $t_2$ in order to determine the orbital locations where the avoidance maneuver and the re-entry maneuver must be applied. The velocities in the transfer orbit at $t_1$ and $t_2$ are then obtained by solving for the transfer orbit using Lambert's problem between the departure and arrival point for the corresponding time of flight $t_f$.

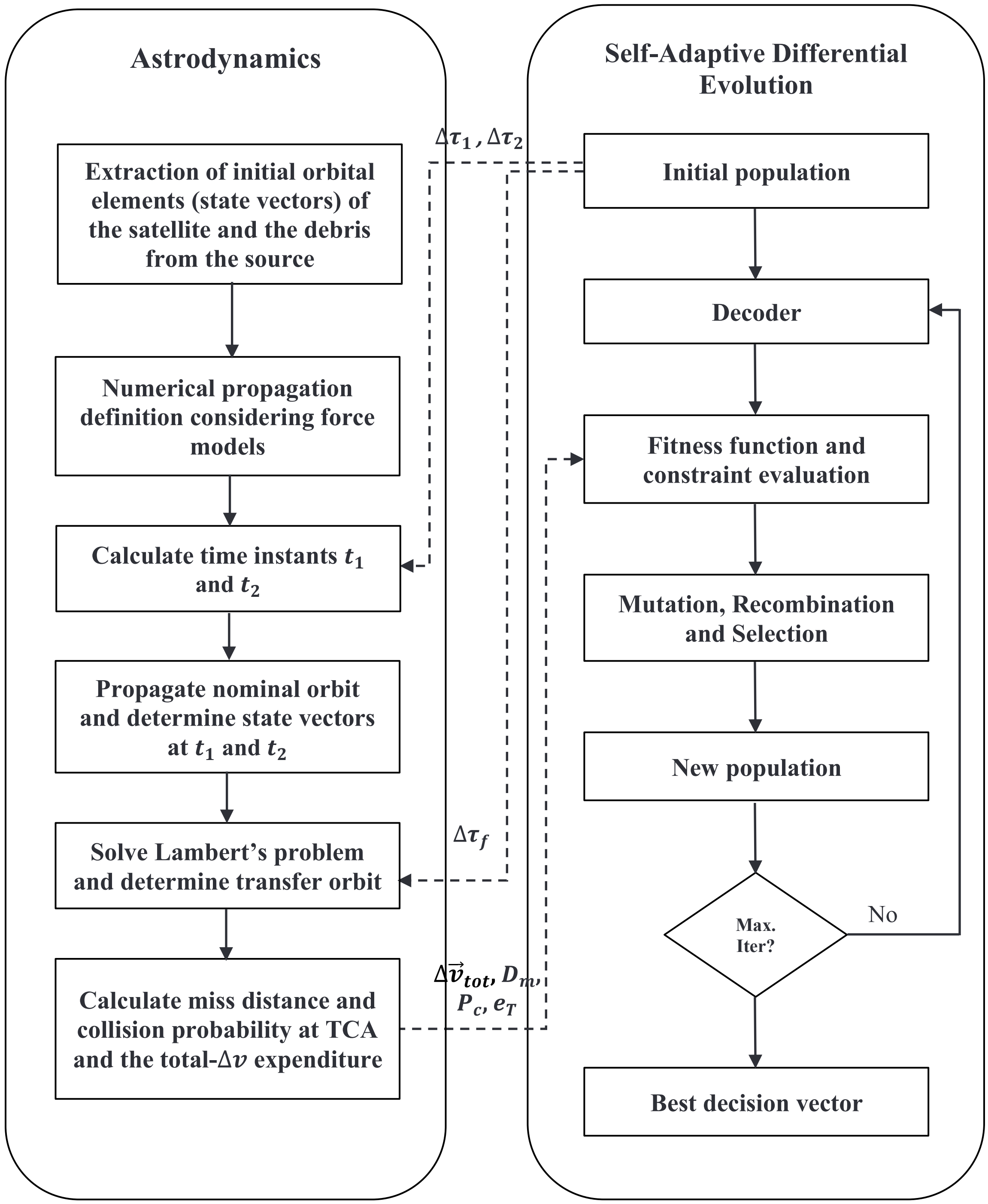


**Fig. 4. 1 Flowchart illustrating the workflow involved in two-impulse collision avoidance maneuver method**

Followed by this, the miss distance and collision probability between the satellite and the debris are computed at the time of new closest approach with regards to the satellite's transfer orbit. Finally, the cost function and the constraints are computed and thus, for every iteration, the algorithm repeats the operation until a globally best solution is determined. The constraints involved in two-impulse collision avoidance maneuver are detailed in the following subsection.

### 4.4.1 CONSTRAINTS

Trajectory optimization problems are normally structured as constrained problems such that optimal solutions can be achieved rigorously with minimal computational effort. The constraints used in this approach are analogous to those used in the three-impulse approach (discussed in section 3.5) that monitor whether if the satellite safely passes through during the time of closest approach.

$$\Delta r_{ca} > D_m \tag{4.21}$$

$$P_c < P_{max} \tag{4.22}$$

However, in addition to these two satellite-safety constraints, two more constraints are implemented: eccentricity constraint and time of flight constraint. The purpose of the eccentricity constraint is to limit the transfer orbit thus obtained to be elliptical. This is because to avoid determining hyperbolic and parabolic orbits that unequivocally result in larger $\Delta v$ values. The equation for eccentricity constraint is given in the eqn. (4.20),

$$e_T < 1 \tag{4.23}$$

where, $\boldsymbol{e_T}$ is the eccentricity of the transfer orbit such that the nature of the transfer orbit must be elliptical. On the other hand, it is assumed that the transfer orbit is adjacent to the nominal orbit such that the semimajor axes and the orbital period of both the orbits are more or less equal. This implies that the orbits are nearly touching each other. For this reason, the time of flight constraint is implemented as an equality constraint such that it ensures that the transfer period between the initial and final position in the transfer orbit is equal to that if travelled in the original orbit. The use of this eccentricity constraint significantly narrow downs the numerical search space where feasible solutions can be located. The time of flight constraint can be written as:

$$\Delta t_f = t_2 - t_1 \tag{4.24}$$

where,

$$\Delta t_f = \Delta\tau_f * T_s \tag{4.25}$$

Substituting equations 4.18, 4.19 and 4.25 into 4.24 then,

$$\Delta\tau_f = \Delta\tau_1 + \Delta\tau_2 \tag{4.26}$$

The above constraints given in equations (4.18), (4.19), (4.26) statistically lead the particles i.e., the optimization parameters, to a feasible region and thereby facilitating the algorithm to determine the transfer trajectory that lies adjacent to the nominal orbit while maintaining a safe separation distance during the time of closest approach.

## 4.5 NUMERICAL SIMULATIONS FOR TWO-IMPULSE APPROACH

This section provides the results of the numerical simulations conducted to test the efficacy of the two-impulse collision avoidance scheme. The collision case used to test this method is same as the one used in section 3.6, however, only one set of simulations conducted that involves varying the constraints (case 1a, 1b and 1c). This is because the avoidance maneuver calculated in the two-impulse method relies on the solutions of Lambert's problem and hence the direction cannot be modified iarbitrarily.

| ***Optimization parameters*** | ***$l_b$*** | ***$u_b$*** |
|---|---|---|
| $\Delta\tau_1$ *(orbits)* | 0 | 1 |
| $\Delta\tau_2$ *(orbits)* | 0 | 1 |
| $\Delta\tau_f$ *(orbits)* | 0 | 1 |

**Table 4. 1 Lower and upper bounds for the optimization parameters**

The two-impulse schema is less complex thus containing 3 optimization parameters that allow determining an optimal trajectory path while evading from the collision to take place. Table 4.1 provides the bounds for the optimization parameters that define the search space and the constraint tolerances used are: $\pm 10^{-3}$ for miss distance, $\pm 10^{-8}$ for collision probability, $\pm 10^{-5}$ for eccentricity and $\pm 10^{-2}$ for the time of flight. The method is devised such that to perform orbital rendezvous within a short time interval after a brief notification time. Thus, the orbital location at which the first impulse for collision avoidance, $\Delta\tau_1$, and the second impulse for orbital re-insertion, $\Delta\tau_2$, must be applied is limited to one orbit before and after the predicted collision time, respectively, while the transfer time, $\Delta\tau_f$, between these two points is restricted to one orbit.

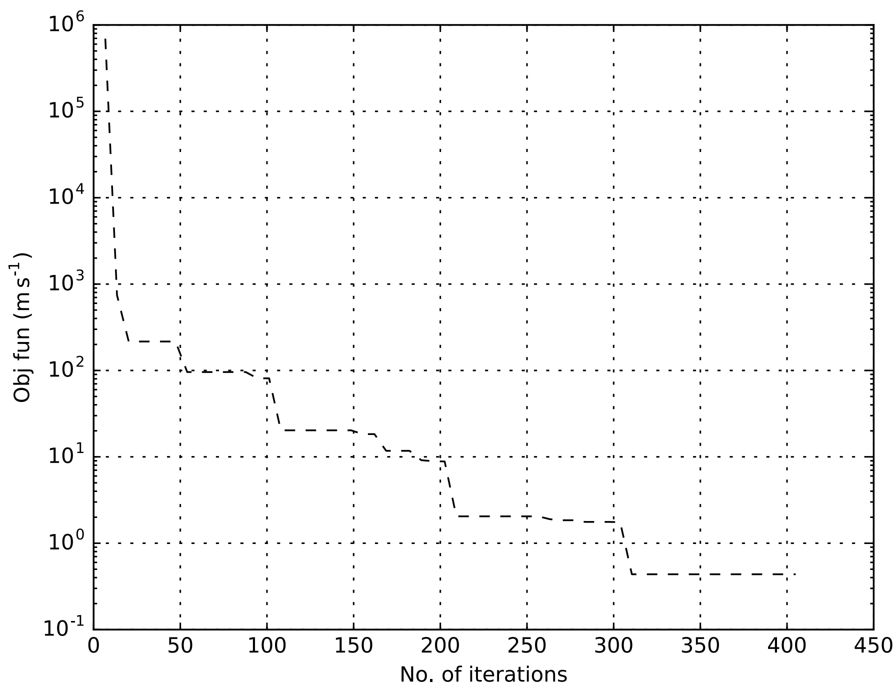


**Fig. 4. 2 Evolution of objective function**

For the two-impulse method, the SADE algorithm showed a faster convergence rate due to its simplicity and points out that the algorithm needs about 400 iterations to attain the global optimal solution. Figure 4.2 illustrates the evolution of the objective function with respect to the number of iterations.

| *Item* | *Value* |
|---|---|
| *Optimization algorithm* | Self Adaptive Differential Evolution |
| *Population size* | 50 |
| *Number of generations* | 400 |
| *Mutation scheme* | best/1/bin |

**Table 4. 2 Lower and upper bounds for the optimization parameters**

### 4.5.1 RESULTS OF NUMERICAL SIMULATIONS

The results of two-impulse method show a similar trend to that of the three-impulse, i.e., when the constraint cost increases, the $\Delta v$ expenditure increases as well. Unfortunately, the second set of simulations corresponding to variation in direction of initial avoidance maneuver is not carried out for this method due to its simplicity in implementing Lambert's problem for determining the transfer orbit.

Tables 4.2, 4.3 and 4.4 report the results for the two-impulse method. It can be noted that the amount of $\Delta v$ required for collision avoidance ($\Delta v_1$) is proportional to that required for orbit re-insertion ($\Delta v_2$). This validates that the control scheme for the two-impulse method is also performing fine, however, the magnitude of the $\Delta v_{tot}$ thus determined using the two-impulse method has larger values compared to that obtained from the three-impulse approach. This shows that decreasing the number of impulses for a typical orbital rendezvous process does not necessarily decrease the overall fuel consumption.

When comparing the results between distinct miss distance constraint (Table 4.2) and distinct collision probability (Tables 4.3) cases, it is found that increasing the minimum achievable $\Delta r_{ca}$ increases the maneuver cycle period while limiting the maximum allowable $P_c$ threshold subsequently reduces the maneuver cycle.

| Maneuver characteristics | | Case 1a | Case 1b | Case 1c |
|---|---|---|---|---|
| $\boldsymbol{t_1}$ | (UTC) | 2012-03-02 23:01:25.211 | 2012-03-02 22:52:22.641 | 2012-03-02 22:57:42.380 |
| $\boldsymbol{\Delta v_1}$ | (m/s) | 0.11025 | 0.14543 | 0.21192 |
| $\boldsymbol{t_2}$ | (UTC) | 2012-03-03 00:33:47.791 | 2012-03-03 00:27:43.641 | 2012-03-03 00:37:51.821 |
| $\boldsymbol{\Delta v_2}$ | (m/s) | 0.11026 | 0.14546 | 0.21194 |
| $\boldsymbol{t_{ca}}$ | (UTC) | 2012-03-03 23:58:11.859 | 2012-03-03 23:58:11.918 | 2012-03-03 23:58:12.013 |
| *Maneuver cycle* | *(mins.)* | 92.376 | 95.347 | 100.157 |
| *Total* $\boldsymbol{\Delta v}$ *consumption* | *(m/s)* | 0.22052 | 0.29091 | 0.42386 |

**Table 4. 3 Simulation results for different miss distance constraint cases**

| Maneuver characteristics | | Case 1a | Case 1d | Case 1e |
|---|---|---|---|---|
| $\boldsymbol{t_1}$ | (UTC) | 2012-03-02 23:01:25.211 | 2012-03-02 22:55:32.363 | 2012-03-02 22:54:16.894 |
| $\boldsymbol{\Delta v_1}$ | (m/s) | 0.11025 | 0.12797 | 0.17838 |
| $\boldsymbol{t_2}$ | (UTC) | 2012-03-03 00:33:47.791 | 2012-03-03 00:33:48.524 | 2012-03-03 00:33:47.791 |
| $\boldsymbol{\Delta v_2}$ | (m/s) | 0.11026 | 0.12798 | 0.17842 |
| $\boldsymbol{t_{ca}}$ | (UTC) | 2012-03-03 23:58:11.859 | 2012-03-03 23:58:11.893 | 2012-03-03 23:58:11.930 |
| *Maneuver cycle* | *(mins.)* | 92.376 | 91.269 | 89.376 |
| *Total* $\boldsymbol{\Delta v}$ *consumption* | *(m/s)* | 0.22052 | 0.25596 | 0.35680 |

**Table 4. 4 Simulation results for different collision probability constraint cases**

| *Cases* | *Radial Separation (m)* | *In-Track Separation (m)* | *Cross-Track Separation (m)* | *Miss Distance* $\Delta r_{ca}$ *(m)* | *Collision Probability* $P_c$ |
|---|---|---|---|---|---|
| *Case 1a* | -369.029 | -952.996 | -181.516 | 1037.9461 | $6.474 \times 10^{-6}$ |
| *Case 1b* | -548.538 | -1439.301 | -155.542 | 1548.119 | $2.116 \times 10^{-7}$ |
| *Case 1c* | -711.599 | -1816.011 | -460.465 | 2004.071 | $1.589 \times 10^{-9}$ |
| *Case 1d* | -477.002 | -1236.713 | -210.310 | 1342.095 | $9.296 \times 10^{-7}$ |
| *Case 1e* | -586.112 | 1542.332 | -144.235 | 1656.237 | $8.711 \times 10^{-8}$ |

**Table 4. 5 Radial, In-track and Cross-track separation distance for distinct constraint cases**

One distinguishing characteristic found from the results of the two-impulse method is that the shorter maneuver cycle period compared to the former approach. Further, the maneuver cycle period is less than the satellite's actual orbital period ($T_s$ = 101.05 mins), which means, although the satellite may become inoperable during that period, yet, it reaches the final re-entry point in the nominal orbit earlier when compared to the actual traverse. This implies early scheduling of the satellite. In addition, the initial impulse is applied nearly half an orbit before the time of predicted collision. These aspects eventually become advantageous when the collision notification time is short so that the orbital rendezvous must be executed swiftly.

On the other hand, the major drawback of the two-impulse method is the high impulse magnitude compared to the three-impulse method, though the former method gave results with longer maneuver cycle; however, the basic goal here is to minimize $\Delta v$. If there arises a situation with a tight maneuver execution time, then the two-impulse maneuver can be considered as a satisfactory solution. Overall, it is a trade-off between the transfer period (maneuver cycle) and the fuel expense. Figures 4.3 – 4.5 show the variation of X, Y and Z components of position in the ECI system after applying the initial avoidance maneuver with regards to the test cases 1a – 1e, respectively. It is noted that the new time of closest approach thus determined is distinctive for each cases, majority of them are occuring after the time of predicted collision, which shows that the satellie is harmless during that period and remains intact throughout the transfer.

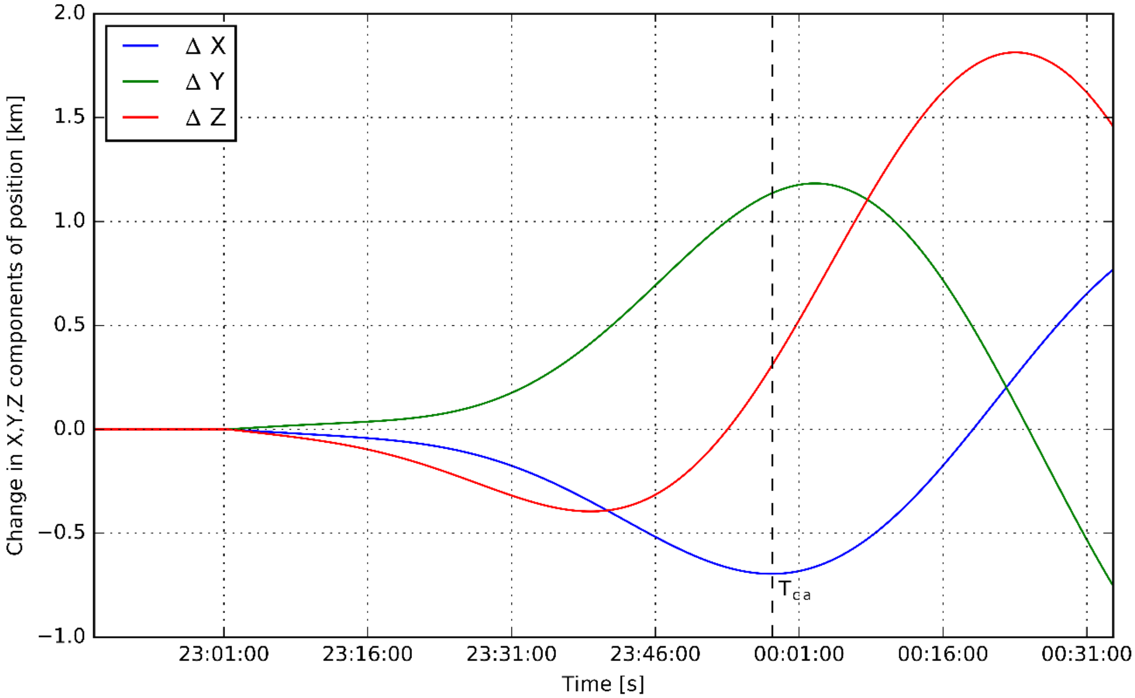


**Fig. 4. 3 Change in X, Y, Z position components of satellite corresponding to test case 1a**

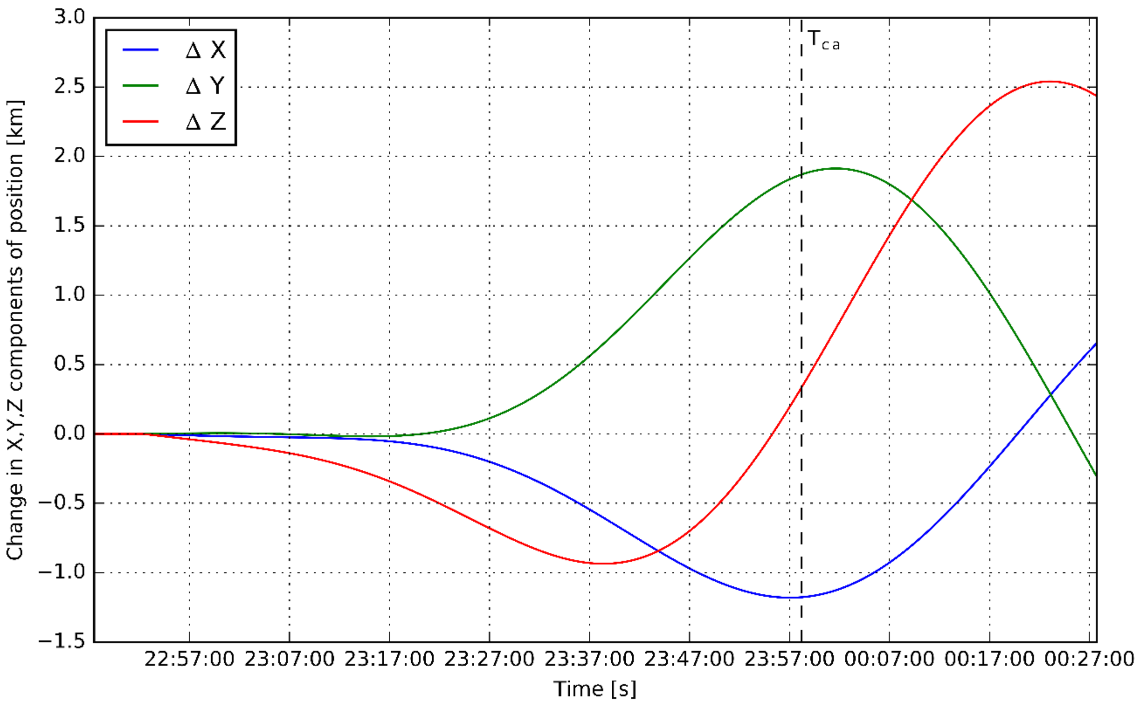


**Fig. 4. 4 Change in X, Y, Z position components of satellite corresponding to test case 1b**

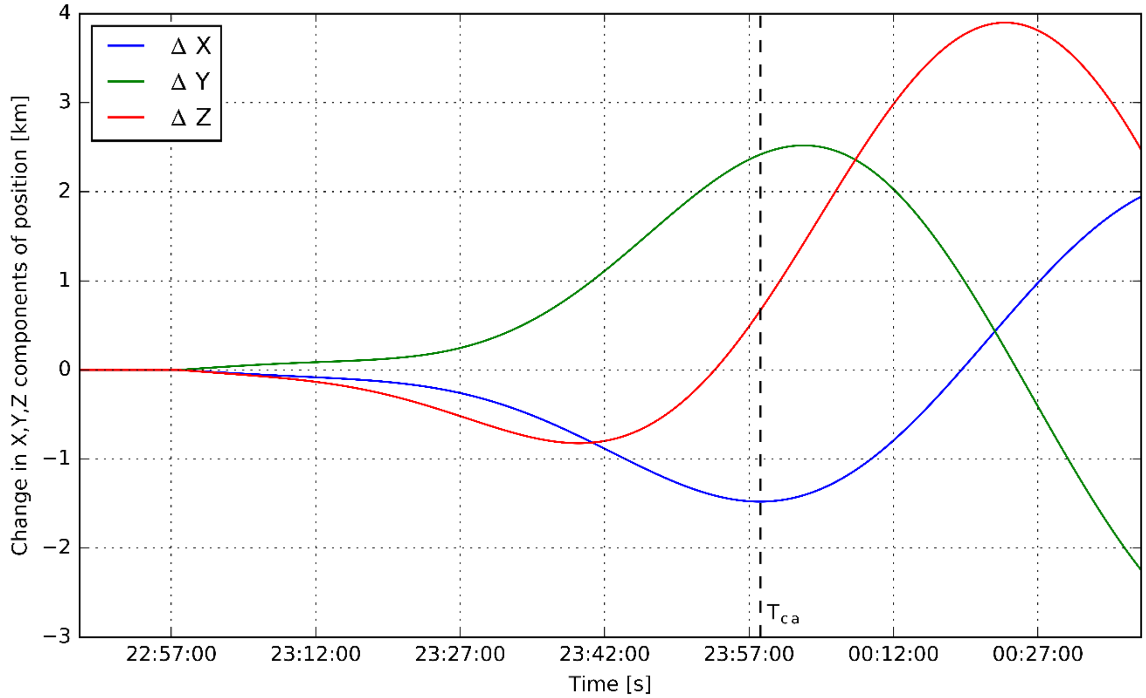


**Fig. 4. 5 Change in X, Y, Z position components of satellite corresponding to test case 1c**

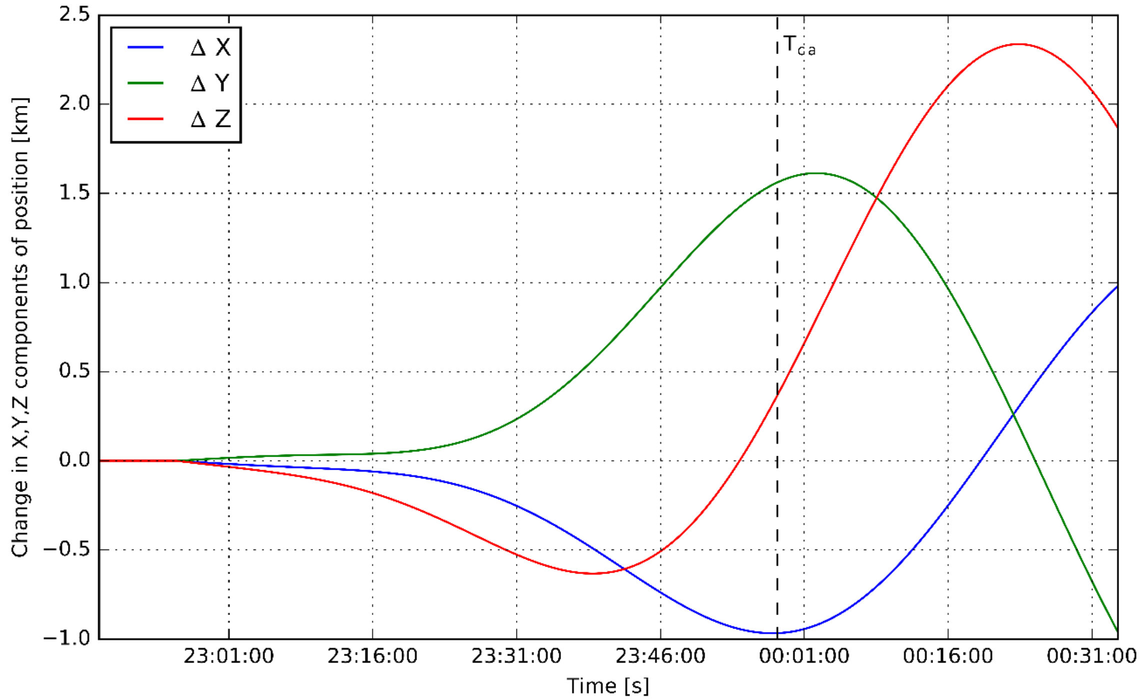


**Fig. 4. 6 Change in X, Y, Z position components of satellite corresponding to test case 1d**

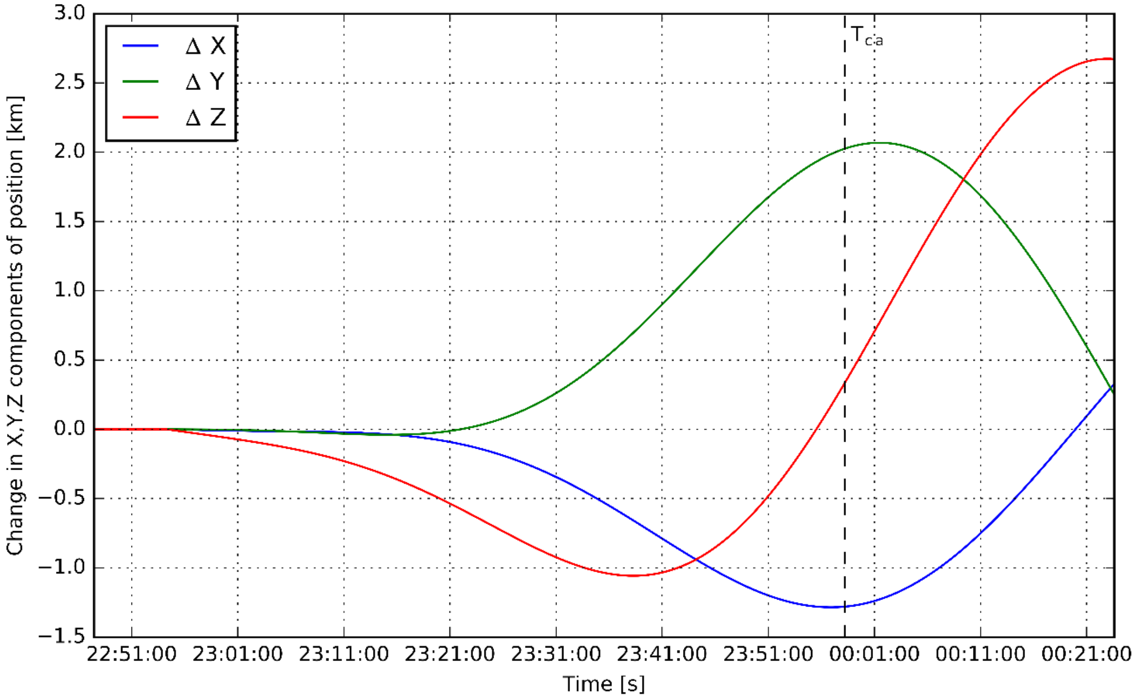


**Fig. 4. 7 Change in X, Y, Z position components of satellite corresponding to test case 1e**

# CONCLUSIONS

## 5.1 SUMMARY OF THE THESIS

In this thesis, the problem of calculating a minimum-fuel trajectory that considers both collision avoidance and orbital re-insertion after successfully avoiding the predicted collision is investigated. For this purpose, two approaches are examined: the three-impulse approach, and the two-impulse approach. Both methods are minimization methods aimed at minimizing the total $\Delta v$ expenditure while satisfying the satellite safety constraints. The former approach was designed with 6 optimization parameters while the latter was designed with 3 optimization parameters. The numerical simulations were performed using the data obtained from CDM and the results thus obtained validated the effectiveness of using Self-Adaptive Differential Evolution for handling trajectory optimization problems.

In the first chapter, a general overview of the current situation in space with respect to space debris population and debris mitigation strategies were presented. This was followed by a literature review that discussed the present methods that are available to compute the collision probability, various approaches for solving the popular Lambert's problem and different methods to determine optimal trajectory while performing collision avoidance maneuver. Lastly, the objectives of this thesis were presented.

In chapter 2, the fundamentals that are to be considered during the planning of a collision avoidance maneuver are described that allows to understand the various stages involved in planning CAM optimization. The chapter first starts by discussing the coordinate systems and orbital elements that define the orbital motion of an object in space. Subsequently, the significance of the covariance matrix that represents the uncertainty in the orbital motion of an object in space and the process flow involved in planning a CAM are explained. Followed by this, the information about the tools and their functionalities that are used towards the development of the proposed methods in this study are presented in this chapter.

Finally, the description of the three-impulse and two-impulse methods, and the results of the numerical simulations are presented in the third and fourth chapters, respectively. The optimization parameters are carefully chosen that determine the optimal solution for the trajectory optimization problem within the numerical search space defined by the control bounds and the constraints. This enables the satellite operator to consider all possible trajectories that are safe from the approaching debris, within an allowable fuel cost.

The numerical simulations are employed using Self-Adaptive Differential Evolution (SADE) for solving the trajectory optimization problem, under numerical propagation that allowed accurate propagation of the orbits through time while taking into account the force models that define the perturbation effects - Earth zonal harmonics, and the third body attraction. Two sets of simulations were run, one by varying the constraints and the other by regulating the direction of the initial avoidance maneuver. The results illustrated that the SADE algorithm indeed represents a reliable optimization technique to determine fuel-optimal solutions. All solutions secured the desired safety thresholds which are the underlying goal of performing collision avoidance maneuver.

The results from the three-impulse CAM had lower total $\Delta v$ values while the two-impulse approach gave out somewhat balanced solutions with shorter transfer period. That means reducing the number of impulses does not necessarily trim the total amount of fuel required. Upon varying the constraints, it was realized that a considerable amount of $\Delta v$ is being wasted as the bounds for the constraints are arbitrarily specified which can be refined by choosing the thresholds based on the actual mission specifications. Furthermore, the three-impulse method provided better results when the direction of the initial avoidance maneuver is not limited to all three directions (Radial-Transverse-Normal).

Although it gave solutions with longer maneuver cycle, the three-impulse method has the upper hand in many aspects as its control scheme can be modified for more advancements, which is demonstrated in the next section and is not applicable to the two-impulse method due to the algorithm's robustness.

## 5.2 RECOMMENDATIONS FOR FUTURE WORK

More work is desired in order to perfect the proposed algorithms. The main problem is with the calculation of collision probability. The covariance matrix has a large impact on the calculation of collision probability during the time of closest approach for which it requires to be propagated using its initial states; yet, right now, it was resorted to just the static covariance matrix (recorded with regards to the time of predicted collision) acquired from the CDM assuming that they differ only to small extent with respect to the actual covariance.

The future work is to design a solution method for the optimization of trajectory considering both collision avoidance and orbital re-entry for the satellites in GEO. Generally, for the case of satellites in geosynchronous orbit, routine station-keeping maneuvers are required to be performed so as to compensate for the drift due to the perturbation effects. For instance, North-South (NS) station-keeping maneuvers are applied orthogonal to the orbital plane in order to negate the effect of lunar/solar gravitation that perturbs the orbital pole by $0.85^{o}$ per year [65], while East-West (EW) station-keeping maneuvers are applied to control the orbital period and the eccentricity vector. Thus, during the planning of collision avoidance maneuver, the calculation of $\Delta v$ should also consider such station keeping maneuvers so that the orbital motion of the satellite can be simultaneously kept in synchronous with the Earth's rotation.

Further, additional constraints satisfying the mission-related objectives such as ground-track cross-over and satellite scheduling needs can be imparted. For instance, in applications requiring high-resolution imaging of a given target area, Earth Observation (EO) satellites have a limited window (time frame) of opportunity for activity scheduling. To handle this mission objective, another constraint related to scheduling can be added to the algorithm. The design of such constraint is intricate and requires input from the satellite operator. However, a global scheduling constraint can be designed which would allow the operator to modify based on the mission CONOPS (Concept of Operations).

Lastly, it would also be more rational to develop an optimization strategy capable of planning for a series of orbital maneuvers (including orbital re-insertion) that will allow the satellite to navigate through multiple threatening objects at the same time. To do this, a single decision-making model comprising of dynamic models and assumptions of future maneuvers for all threatening objects involved can be introduced. However, this is not straightforward as it involves complicated forethought while planning for an effective optimization framework.

# REFERENCES


1. UCS, *Satellite Database*. 2017: http://www.ucsusa.org/nuclear-weapons/space-weapons/satellite-database#.WblhVtiQyUl. Accessed: June 2017.
2. NASA Orbital Debris Program Office. *Orbital Debris Quarterly News, vol.21, issue 1*. February 2017; Available from: https://www.orbitaldebris.jsc.nasa.gov/quarterly-news/pdfs/odqnv21i1.pdf.
3. ESA, *Space Debris*. 2017: http://www.esa.int/Our_Activities/Operations/Space_Debris/About_space_debris. Accessed: June 2017.
4. Mohamad, F.A., Mohamed Ali, N. A., *Space Debris Low Earth Orbit (LEO).* International Journal of Science and Research (IJSR), 2013. ISSN (Online): 2319-7064.
5. NASA Orbital Debris Program Office. *Orbital Debris Quarterly News, vol.20, issue 1-2*. April 2016; Available from: https://www.orbitaldebris.jsc.nasa.gov/quarterly-news/pdfs/odqnv20i1-2.pdf.
6. NASA Orbital Debris Program Office. *Orbital Debris Quarterly News, vol.19, issue 1*. January 2015; Available from: https://www.orbitaldebris.jsc.nasa.gov/quarterly-news/pdfs/odqnv19i1.pdf.
7. Bombardelli, C., *Analytical formulation of impulsive collision avoidance dynamics.* Celestial Mechanics and Dynamical Astronomy, 2014. **118**(2): p. 99-114.
8. Patera, R.P., Peterson, G. E., *Space vehicle maneuver method to lower collision risk to an acceptable level.* Journal of guidance, control, and dynamics, 2003. **26**(2): p. 233-237.
9. Bombardelli, C. and J. Hernando-Ayuso, *Optimal impulsive collision avoidance in low earth orbit.* Journal of Guidance, Control, and Dynamics, 2015. **38**(2): p. 217-225.
10. Morselli, A., Armellin, R., Di Lizia, P., Bernelli-Zazzera, F., *Collision avoidance maneuver design based on multi-objective optimization.* 2014.
11. Aida, S., Kirschner, M., Kiehling, R. *Collision avoidance operations for LEO satellites controlled by GSOC*. in *SpaceOps 2010 Conference Delivering on the Dream Hosted by NASA Marshall Space Flight Center and Organized by AIAA*. 2010.
12. Lee, S.C., Kim, H.D., Suk, J., *Collision Avoidance Maneuver Planning Using GA for LEO and GEO Satellite Maintained in Keeping Area.* International Journal of Aeronautical and Space Sciences, 2012. **13**: p. 474-483.
13. Akella, M.R., Alfriend, K. T., *Probability of collision between space objects.* Journal of Guidance, Control, and Dynamics, 2000. **23**(5): p. 769-772.
14. Alfano, S., *Review of conjunction probability methods for short-term encounters.* AAS paper, 2007(07-148).
15. Foster, J.L., Estes, H. S., *A parametric analysis of orbital debris collision probability and maneuver rate for space vehicles.* NASA JSC, 1992. **25898**.
16. Patera, R.P., *General method for calculating satellite collision probability.* Journal of Guidance, Control, and Dynamics, 2001. **24**(4): p. 716-722.

17. Alfano, S., *A numerical implementation of spherical object collision probability.* Journal of the Astronautical Sciences, 2005. **53**(1): p. 103.
18. Alfano, S., *Relating Position Uncertainty to Maximum Conjunction Probability.*
19. Arrufat Jackson, T., *Study of the risk of impact between a spacecraft and space debris*. 2013.
20. Chan, K., *Collision probability analysis for earth orbiting satellites.* Space cooperation into the 21 st century, 1997: p. 1033-1048.
21. Prussing, J.E., Conway, B. A., *Orbital mechanics*. 1993: Oxford University Press, USA.
22. Battin, R.H., *An introduction to the mathematics and methods of astrodynamics*. 1999: AIAA.
23. Lagrange, J.L., *Mécanique analytique*. Vol. 1. 1853: Mallet-Bachelier.
24. Gauss, C.F., Davis, C. H., *Theory of the motion of the heavenly bodies moving about the sun in conic sections*. 2004: Courier Corporation.
25. Sangrà, T., Fantino, E. *Review of Lambert's problem*. in *ISSFD 2015: 25th International Symposium on Space Flight Dynamics, 19-23 October, Munich, Germany*. 2015.
26. Bate, R.R., D.D. Mueller, and J.E. White, *Fundamentals of astrodynamics*. 1971: Courier Corporation.
27. Izzo, D., *Revisiting Lambert's problem.* Celestial Mechanics and Dynamical Astronomy, 2015. **121**(1): p. 1-15.
28. Lee, K., C. Park, and S.-Y. Park, *Near-optimal continuous control for spacecraft collision avoidance maneuvers via generating functions.* Aerospace Science and Technology, 2017. **62**: p. 65-74.
29. Kim, E.H., Kim, H. D., Kim, H. J., *A study on the collision avoidance maneuver optimization with multiple space debris.* Journal of Astronomy and Space Sciences, 2012. **29**(1): p. 11-21.
30. Vallado, D.A., *Fundamentals of astrodynamics and applications*. Vol. 12. 2001: Springer Science & Business Media.
31. Alfano, S., *Method for determining maximum conjunction probability of rectangular-shaped objects*. 2007, Google Patents.
32. Chobotov, V.A., *Orbital mechanics third edition*. 2002, AIAA.
33. Exoplanet Musings, *RV Fits: The Keplerian Solution*. 2013: https://exoplanetmusings.wordpress.com/2013/05/. Accessed: August 2017.
34. Florijn, D.W., *Collision analysis and mitigation for distributed space systems.* 2015.
35. Chan, F.K., *Spacecraft collision probability*. 2008: Aerospace Press El Segundo, CA.
36. Morselli, A., *High order methods for Space Situational Awareness.* 2014.
37. NASA, *Definition of Two-line Element Set Coordinate System*. 2011: https://spaceflight.nasa.gov/realdata/sightings/SSapplications/Post/JavaSSOP/SSOP_Help/tle_def.html. Accessed: May 2017.
38. Space-track. TLE data: https://www.space-track.org/. Accessed: May 2016.
39. CCSDS, *CDM data*. https://cwe.ccsds.org/moims/docs/Forms/AllItems.aspx?RootFolder=%2Fmoims%2Fdocs%2FMOIMSNAV%2FDraft%20Documents%2FConjunction%20Data%20Message%20(CDM). Accessed: September 2016.
40. Chen, L., et al., *Orbital data applications for space object.* National Defense Industry Press, 2015.

41. Hall, R., S. Alfano, and A. Ocampo. *Advances in satellite conjunction analysis*. in *Proceedings of the Advanced Maui Optical and Space Surveillance Technologies Conference*. 2010.
42. Kelso, T. and S. Alfano, *Satellite Orbital Conjunction Reports Assessing Threatening Encounters in Space(SOCRATES).*
43. NASA, *Conjunction Assessment Risk Analysis*. https://satellitesafety.gsfc.nasa.gov/CARA.html. Accessed: May 2017.
44. OREKIT, *API Overview*. https://www.orekit.org/static/apidocs/overviewsummary.html. Accessed: April 2017.
45. Shou, H.-N., *Orbit propagation and determination of low earth orbit satellites.* International Journal of Antennas and Propagation, 2014. **2014**.
46. Möckel, M., *High performance propagation of large object populations in earth orbits*. 2015: Logos Verlag Berlin GmbH.
47. Aristoff, J.M. and A.B. Poore. *Implicit Runge–Kutta methods for orbit propagation*. in *AIAA/AAS Astrodynamics Specialist Conference, Minneapolis, MN, AIAA*. 2012.
48. OREKIT, *Numerical Propagator*. https://www.orekit.org/static/apidocs/org/orekit/propagation/numerical/NumericalPropagator.html. Accessed: April 2017.
49. OREKIT, *Dormand Prince 8(5,3) Integrator*. https://www.hipparchus.org/apidocs/org/hipparchus/ode/nonstiff/DormandPrince853Integrator.html. Accessed: April 2017.
50. Hairer, E. and G. Wanner, *Solving ordinary differential equations. II, volume 14 of Springer Series in Computational Mathematics*. 1996, Springer-Verlag, Berlin.
51. Azari, P., *An Orbit Control System for UWE-4 Using the High Fidelity Simulation Tool Orekit*. 2017.
52. OREKIT, *TLE Propagator*. https://www.orekit.org/static/apidocs/org/orekit/propagation/analytical/tle/TLEPropagator.html. Accessed: April 2017.
53. Billemont, S., *Numerical Optimization of a Low-Thrust Mission to the Solar Poles*. 2014, Delft University of Technology.
54. OREKIT, *Force models*. https://www.orekit.org/static/apidocs/org/orekit/forces/ForceModel.html. Accessed: April 2017.
55. Deb, K., *Evolutionary algorithms for multi-criterion optimization in engineering design.* Evolutionary algorithms in engineering and computer science, 1999. **2**: p. 135-161.
56. Seong, J.-D. and H.-D. Kim, *Multiobjective optimization for collision avoidance maneuver using a genetic algorithm.* Proceedings of the Institution of Mechanical Engineers, Part G: Journal of Aerospace Engineering, 2016. **230**(8): p. 1438-1447.
57. Elsayed, S.M., R.A. Sarker, and D.L. Essam. *Differential evolution with multiple strategies for solving CEC2011 real-world numerical optimization problems*. in *Evolutionary Computation (CEC), 2011 IEEE Congress on*. 2011. IEEE.
58. PaGMO. 2017: https://esa.github.io/pagmo2/index.html. Accessed: April 2017.
59. Gavigan, P., *Estimation of Minimum Required Thrust for Spacecraft Collision Avoidance*. 2013: Defence Research and Development Canada.
60. Reiter, J.A., *Numerical And Analytical Solutions To Rapid Collision Avoidance Maneuvers Constrained By Mission Performance Requirements.* 2016.
61. Bombardelli, C., J. Hernando-Ayuso, and R. García-Pelayo, *Collision avoidance maneuver optimization.* Advances in the Astronautical Sciences, 2014: p. 2014-335.

62. Lázaro, D. and P.L. Righetti. *Evolution of EUMETSAT LEO conjunctions events handling operations*. in *Proceedings of SpaceOps 2012 Conference*. 2012.
63. Goudos, S.K., et al., *A comparative study of common and self-adaptive differential evolution strategies on numerical benchmark problems.* Procedia Computer Science, 2011. **3**: p. 83-88.
64. Pontani, M. and B.A. Conway, *Particle swarm optimization applied to impulsive orbital transfers.* Acta Astronautica, 2012. **74**: p. 141-155.
65. Anderson, P.V., et al. *Operational considerations of GEO debris synchronization dynamics*. in *66th International Astronautical Congress, IAC-15 A*.